Thin Polymer Films Out of Thermodynamic Equilibrium

Inaugural-Dissertation zur Erlangung des Doktorgrades der

Fakultät für Mathematik und Physik der

Albert-Ludwigs-Universität Freiburg

Vorgelegt von

Mithun CHOWDHURY

2012

Dekan: Prof. Dr. Kay Königsmann
Leiter der Arbeit: Prof. Dr. Günter Reiter
Referent: Prof. Dr. Günter Reiter
Koreferent: Prof. Dr.
Prüfer (Theorie): Prof. Dr. Alexander Blumen
Prüfer (Experiment): Prof. Dr. Elizabeth von Hauff
Datum der mündlichen Prüfung : 30.08.2012

To my family

Abstract

The fabrication process of a thin polymer film, involving the transition from a (dilute) solution to a dry glass, is believed to have an impact on film properties, often related to the poorly entangled out-of-equilibrium chain conformations and corresponding residual stresses. Thus, a central question concerns the possibility of relaxation of such chains even in the glassy state. Physical ageing of polymer films at temperatures below the glass transition ($T_{g,bulk}$) was found to lead to a progressive decrease in dewetting velocity, which is indicative of a decreasing residual stress or an increasing modulus with ageing time. Dewetting velocity showed a close to exponential decay with ageing time, defining a characteristic relaxation time. Variation of relaxation times with temperature seems to follow an Arrhenius temperature dependence [**i**]. This suggests a process of a faster segmental relaxation mechanism, which is sufficient to relax part of the residual stresses. The relaxation dynamics of residual stresses appears to be in close agreement with some earlier reports, concerning relaxation solely at the surface of polymer thin films [**i**]. This intriguingly invokes the possibility to correlate the surface mobility in thin polymer film with non-equilibrium conformation of polymer chains. The relaxation behaviour of such films, both above and below the $T_{g,bulk}$, is notably faster than the α-relaxation time and reptation time of the bulk polymer [**i,ii**]. In addition, films prepared from solutions close to the theta-temperature were aged for varying times at room temperature and characterized by dewetting. The characteristic relaxation time of ageing varied strongly with the quality of the solvent, which is attributed to distorted chain conformations in the as-cast films [**iii**]. This signifies quite clearly the non-equilibrium nature of thin polymer films, possibly causing some of their unexplained properties, such as fast relaxation.

Interestingly, the process of physical ageing of such films at elevated temperatures close but still below the $T_{g,bulk}$ can also lead to crack formation [**iv**]. We observed cracking during cooling these films to room temperature. For long chain polymers,

AFM inspection inside the cracking patterns showed craze nano/microstructures consisting of voids and fibrils. Short chain polymers (of a length comparable to the entanglement length) did not show such crazes, rather formed simple cracks. For higher molecular weight polystyrene, a systematic study showed a progressive increase of craze growth velocity with ageing time whereas for the same films the dewetting velocity decreased with ageing. While the increase in craze growth velocity might indicate an increase in total stress inside the film upon a temperature jump, the decrease of dewetting velocity is the signature of relaxation of residual stresses.
In summary, our study invokes the possibility to correlate several of the long standing puzzling properties of thin polymer films with respect to the non-equilibrium conformations of polymer chains inside the film.

Publication references:
[**i**] Chowdhury, M., Freyberg, P., Ziebert, F., Yang, A. C. -M., Steiner, U. and Reiter, G. "Segmental Relaxations have Macroscopic Consequences in Glassy Polymer Films" accepted in Phys. Rev. Lett. (August 2012).
[**ii**] Chowdhury, M. and Reiter, G. *et al.* "Influence of Temperature on Dewetting and Relaxation of Thin Polymer Films above the Glass Transition Temperature" in preparation.
[**iii**] Raegen, A., Chowdhury, M., Calers, C., Schmatulla, A., Steiner, U., and Reiter, G. "Aging of Thin Polymer Films Cast from a Near-Theta Solvent" Phys. Rev. Lett. 105(22), 227801 (2010).
[**iv**] Chowdhury, M., Yang, A. C. -M., Steiner, U. and Reiter, G. "Cracking and Crazing in Thin Glassy Polymer Films by Physical Ageing" in preparation.

Other related publications (not included in this thesis):

[**a**] Clough, A., Chowdhury, M., Jahanshahi, K., Reiter, G. and Tsui, O.K.C. "Swelling with a Near-Θ Solvent as a Means to Modify the Properties of Polymer Thin Films" published online in Macromolecules. (July 2012).

Contents

Chapter 1

Introduction and Background of Motivation

1.1 Introduction to polymers

1.1.1 Structure of polymers

Polymers are ubiquitous in our daily life. Polymers are met under a large variety of chemical achievements, from biopolymers like DNA, cellulose, proteins, and actin filaments, to synthesized polymers like polyethylene (PE), polybutadiene (PB), polystyrene (PS), polymethylmethacrylate (PMMA), and so on, all of great industrial interest. Details of the molecular structure of polymers remained a mystery until Hermann Staudinger proposed the structural concept of macromolecules while working in Freiburg [1]. His work was acknowledged in 1953 when he was awarded the Nobel Prize for Chemistry. Polymers are formed by repeating a molecular unit for many times within the same molecule (cf. **Figure 1.1)**. Due to the connectivity the units are not independent. However, they have a certain amount of freedom which leads to several complex behaviours. The molar mass distribution (or molecular weight distribution) in a polymer describes the relationship between the number of moles of each polymer species (N_i) of molar mass (M_i). The number of subunits is called degree of polymerization N. Polymer molecules, even ones of the same type, come in different sizes (chain lengths, for linear polymers), so the average molecular weight will depend on the method of averaging. The number average molecular weight (M_n) is the arithmetic mean of the molecular weights of the individual macromolecules. It is determined by measuring the molecular weight of N_i polymer molecules, summing the weights, and dividing by N_i. The weight average molecular weight is

the average of molecular weights in a polymer due to the occurence of different chain lengths (polydispersity) present in it.

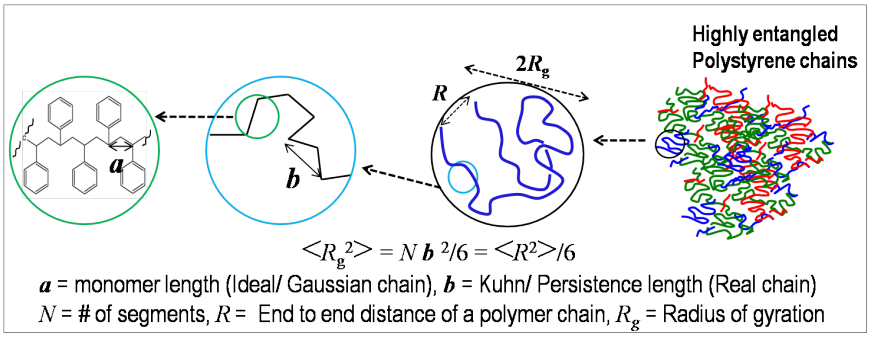

Figure 1.1 – Schematic of a polymer chain at different length scales. Redrawn inspired from ref. [2].

The simplest polymers are linear homopolymers, *i.e.* repeat units follow a single linear backbone and all the units are identical: AAAAAAAAA. Block-copolymer consists of two or more blocks, *e.g.* AAA-BBB-AAA, a tri-block co-polymer. Polymers are the main building block of soft matter physics, a term first coined by Pierre Gilles de Gennes [3]. This means: (i) They are very deformable objects: temperature (the thermal energy k_BT) and entropy are important in determining their shape and behaviour. (ii) Due to the connectivity, large size, and their deformability, polymers and other soft matter systems are very responsive: small external forces can have large effects. (iii) Structures on the scale of nano to micrometer determine their behaviour. In contrast to simple liquids and crystals, which have units of fractions of nanometers and are homogeneous on length scales larger than the nanometer scale, soft matter systems like polymers can be structured and inhomogeneous up to micron scale [4].

The arrangement of the subunits of a polymer in space is called its conformation. The foundation of polymer physics is based on the consequences of connectivity and conformational variability in polymer chains. Statistical description can nicely explain these facts. The simplest molecular architecture corresponds to linear molecules that consist of identical monomer units connected end-to-end. For a linear polymer chain, the maximum end-to-end distance, R. The contour length (L) of a polymer chain is equal to the sum of the lengths (a) of all monomer segments as $L = Na$. Further, the idea of equivalent or Kuhn segments (b) in a chain can be implemented by introducing segments that are statistically independent. In a collection of similar molecules, a linear polymer molecule will adopt the shape of a random coil. The overall coil size can be characterized statistically by the root-mean-square end-to-end distance R_{RMS} which scales as the square root of

the length of the molecule (N) or its molecular weight (M_w) and typically ranges from several nanometers to tens of nanometers, $R_{RMS} \sim \sqrt{\langle R^2 \rangle} \sim aN^{1/2} \sim bN^{1/2}$. The polymer molecule can be described by a variety of different length scales, ranging from the size of the individual monomers to the overall macrscopic entangled molecules (cf. **Figure 1.1**). Obviously entropy plays an important role. Entropy for non-connected molecules without interactions tries to maximize by increasing randomness of the distribution. Similar considerations of maximizing entropy are also applicable for polymers. But due to the connectivity, connected monomers cannot spread over the whole space and the polymer will form a coiled path. Only very stiff polymers (with strong interactions along the backbone) can keep straight against entropy. Large N and the connectivity lead to constraints in the dynamics of chains. If many chains come together closely they can entangle (cf. **Figure 1.1**).

The first quantitative question one may ask when starting to deal with polymer is the characteristic size of a single polymer coil in solution and how does this size depend on the degree of polymerization of the polymer? A simple way to introduce the fundamentals of the behaviour of a polymer in solution or a molten polymer is through the presentation of the scaling properties [5]. In such a case, a number of properties are not dependent on the local segmental scales/monomers, and the chemical features can be ignored. On the other hand, all mesoscopic properties depend on N according to scaling laws, of the type $R_g \sim N^{\nu}$, where, R_g is the so-called radius of gyration, *i.e.*, a characteristic size of the statistical coil representing the polymeric chain. For a random walk of a polymer chain it can be shown that,

$$\left\langle R_g^2 \right\rangle = \frac{1}{6} b^2 N = \frac{1}{6} \left\langle R^2 \right\rangle \tag{1.1}$$

i.e. the mean squared radius of gyration and the mean squared end-to-end distance for a linear polymer differ only by a numerical factor. By statistical random walk counting or by the analogy of Brownian diffusion of particles one can show that the probability $p(N, R)$ for the N-link chain in the volume element $(dR)^3$ around R has the Gaussian distribution:

$$p(N, R) = \left(\frac{3}{2\pi b^2 N} \right)^{\frac{3}{2}} \exp\left(-\frac{3R^2}{2b^2 N} \right) \tag{1.2}$$

So far, we accounted for interactions between neighbouring monomers of

the polymer chain, but we neglected interactions between distant points on the chain *i.e.* interactions between monomers along the backbones. For an isolated chain these interactions are important, and affect the long range structure of the chain. Distinctly two limiting cases can be considered. In a very dilute solution, each chain has an individual behaviour independent of the other chains. If the chain is swollen, one refers to the solvent as a good solvent; the radius of gyration of the chain scales as the Flory radius ($R_g \sim R_F \sim N^{3/5}$). In the absence of solvent, *i.e.* in a melt, each monomer of a "molten" polymer is subjected to attractive van der Waals interactions (due to the monomers of other neighbouring chains) and to repulsive interactions (due to the monomers of the same chain). These interactions compensate exactly at the scale of a few monomers, because the density fluctuations of the melt are so small. Therefore, each chain is expected to behave in a melt as an ideal chain ($R_g \sim N^{1/2}$). Such ideality can be reachable even in solvents, namely theta-solvents, at a particular temperature-solvent condition in which the excluded volume of other monomers become zero and the monomers do not feel the existence of other particles in the solvent [6, 7]. The statistics of a single polymer chain depends on the solvent. For good solvent the chain is more expanded while for bad solvent the chain segments stay close to each other. In the limit of a very bad solvent the polymer chain collapse to form a hard sphere, while in good solvent the chain swells in order to maximize the number of polymer-fluid contacts.

Interactions between monomers of the chain and with the solvent molecules can be described by an effective potential $U(r)$. It describes the energy to bring a monomer in a surrounding containing solvent from infinity to a distance r with respect to a reference monomer. The potential contains a repulsive part for small r, describing the excluded volume (cf. **Figure 1.2**). This is reflected in the idea

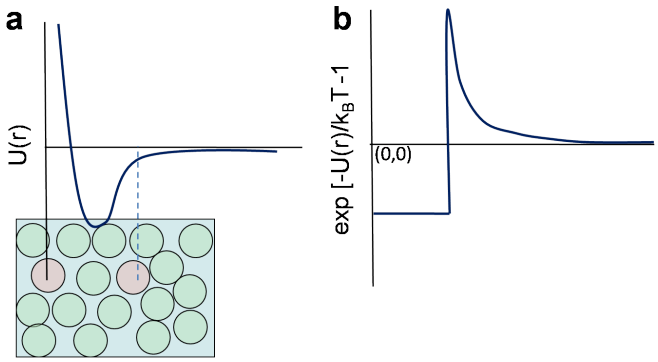

Figure 1.2 – (a) Schematic form of the potential *U(r)* representing interactions between monomers of the chain and with the solvent molecules. (b) The function $[\exp(-U(r)/k_BT) - 1]$. Area under the curve is the integration area indicating the excluded volume. Reproduced from ref. [7].

of a self avoiding random walk of polymers, two monomers cannot be in the same place together or in other words, a chain cannot intersect itself. If the monomers like each other more than the solvent, there will be an additional attractive interaction and vice-versa. The probability to find two monomers a distance r away from each other, in an non-interacting equilibrium situation, is proportional to the $\exp(-U(r)/k_BT)$ and the excluded volume can be defined as,

$$v = -\int f(r)d^3r = \int -4\pi r^2 f(r)dr \tag{1.3}$$

Where $f(r)$ is known as Mayer f-function $f(r) = \exp\left(-\frac{U(r)}{K_BT}\right) - 1$. $v < 0$ implies net attraction and $v > 0$ net repulsion. With b the characteristic size of the molecule, one gets $v = -\int f dv = (4\pi/3)b^3 \sim b^3$. This relation holds strictly for spherical subunits, similar to particles. Kuhn segments are rather cylindrical (rod-like), and their characteristic excluded volume is $v = b^2d$ (with b is the size (length) of the segment and d is the diameter of the segment). Based on the excluded volume different solvent conditions can be defined [7].

Athermal solvent: $v = b^2d$; here v is independent of temperature. Holds if: (i) Monomers are chemically identical with the solvent (ii) For high temperatures. The system only features repulsive interactions. Monomer-monomer interaction is energetically indistinguishable from monomer-solvent contact. Example: Polystyrene (PS) in toluene, ethyl benzene.

Good solvent: $0 < v < b^2d$; here excluded volume is reduced due to monomer-monomer attraction. Hence the solvent particles enter the chain, resulting in a swelling of the chain. The effect of this attraction is greater at lower temperature: for decrease in T, f increases and hence v decreases. Example: PS in benzene.

Theta-solvent: $v = 0$; holds at the special temperature T_Θ. Attractive and repulsive interactions are exactly balanced and cancelled. Chains are nearly ideal at the theta-point. Example: PS in cyclohexane at $T_\Theta = 34.5$ °C, PS in trans-decalin at $T_\Theta = 21$ °C.

Poor solvent: $-b^2d < v < 0$, for $T < T_\Theta$, the attractive interactions between monomers dominate over monomer-solvent and monomers will be closer together than in an ideal situation. Example: PS in ethanol.

Non-solvent: $v = -b^2d$; the solvent will be completely expelled from the chain interior, the chain collapses. Example: PS in water.

The Flory theory estimates the energetic and entropic contributions to the polymer chain due to the presence of a good solvent in the athermal limit, it means it considers the interactions between monomers separated by many bonds along the chain. To understand the importance of such interactions one need to

estimate the number of monomer-monomer contacts within a single coil. This number depends on the probability for a given monomer to encounter any other monomer that is separated from it by many bonds along the polymer. An estimate of this probability can be made for the general case of an ideal chain in D-dimensional space for a polymer chain of N monomers in the pervaded volume of a coil $\sim R^D$. The probability can be expressed in terms of volume fraction of overlap, $\Phi^* \approx Nb^D/R^D$. The probability of a second monomer being within the excluded volume v of a given monomer is $\Phi^* \approx Nb^3/R^3 \approx Nv/R^3$. The energetic cost of being excluded from this volume (the energy of excluded volume interaction) is k_BT per exclusion or k_BTNv/R^3 per monomer. Hence the interaction part of the Free energy (F) can be estimated as:

$$F_{int} \approx Nk_BT\frac{Nv}{R^3} \tag{1.4}$$

Excluded volume interactions have energies of k_BT from entropic origin. The part of the free energy stemming from entropic elasticity (it costs configurational entropy, to stretch the chain) is given by

$$F_{ent} \approx k_BT\frac{R^2}{Nb^2} \tag{1.5}$$

In total,

$$F = F_{int} + F_{ent} \approx k_BT\left(\frac{N^2v}{R^3} + \frac{R^2}{Nb^2}\right) \tag{1.6}$$

At equilibrium (at $R = R_F$) the system will attain the minimum of the free energy, *i.e.* $\partial F/\partial R = 0$. This is finally leads to the scaling relation of Flory radius as $R_F \sim N^{3/5}$. In general, the Flory theory leads to a universal power law dependence of polymer size to the number of monomer units $R \sim N^\nu$. $\nu = 1/2$ for Θ-solvent, $\nu = 3/5$ for athermal/good solvent and $\nu = 1/3$ for poor/non solvent. Radii of gyration have been measured in dilute solutions of polymers (in a good solvent and dilute enough such that individual coils are independent) by light scattering, viscometry, or diffusivity measurement, and simulated numerically. All of these measurements yield a critical exponent ν close to 0.6 for a polymer in a good solvent. Whereas, similar experiements indicated an exponent close to 0.5 for a polymer in a theta-solvent. An actual isolated polymeric chain is more swollen than is an ideal chain, as expected. The simple approach taken by Flory provides surprisingly good results in agreement with experiments and calculations as $R \sim N^{0.588}$ [6]. However, the success of the Flory theory is due to a cancellation of errors. The excluded volume contributions are overestimated as correlations between monomers (which decrease the probability of overlap) are not considered.

At the same time, the entropic restoring force is also overestimated.

In calculating the entropy contribution in the free energy of a coil, one needs to consider the stretched conformation of an ideal chain, a directed random walk of tension blobs. The idea of tension blob (of diameter ξ) can be also implemented in terms of thermal blobs of characteristic size ξ_T (cf. **Figure 1.3**). One

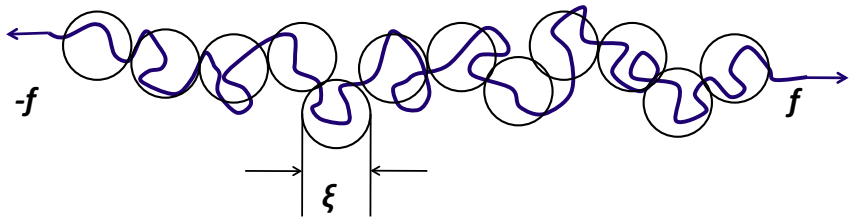

Figure 1.3 – Splitting of a swollen chain into blobs under an applied force. Redrawn after ref. [6].

can consider a blob that is associated with the balance between thermal energy and the energetic contribution due to excluded volume interactions. Below temperature T, the polymer is ideal whereas above T, excluded volume interactions dominate and the system executes a self-avoiding random walk. For scales smaller than ξ_T the chains are ideal, while on scales larger than ξ_T, the excluded volume energy dominates and solvent effects, *i.e.* swelling of the chain occurs. It holds the relation $\xi_T \approx b g_T^{1/2}$ similar to the random walk of ideal chain whereas for real chain $\xi_T \approx b g_T^{3/5}$. Using a mean field number density of monomers inside the blob, the excluded volume interaction energy (cf. **Equation 1.4**) can be written as $k_B T v g_T^2/\xi_T^3$. This energy is balanced by the thermal energy, $k_B T$ so that the thermal blob size is given by $\xi_T \approx b^4/v$ and the number of monomers in a blob as $g_T \approx b^6/v^2$.

If one considers the conformation of the chain above blob length scale, in a good solvent the excluded volume repulsion is larger than thermal energy $k_B T$, and the polymer is a swollen chain of N/g_T thermal blobs which follow a self-avoiding random walk.

$$R \approx \xi_T \left(N/g_T\right)^{\nu} \approx b \left(\frac{v}{b^3}\right)^{2\nu-1} N^{\nu} \tag{1.7}$$

$\nu \approx 3/5$ in this equation leads to Flory argument. The overall behaviour of a single polymer coil size can be expressed as shown in **Figure 1.4** in terms of scaling relations [7].

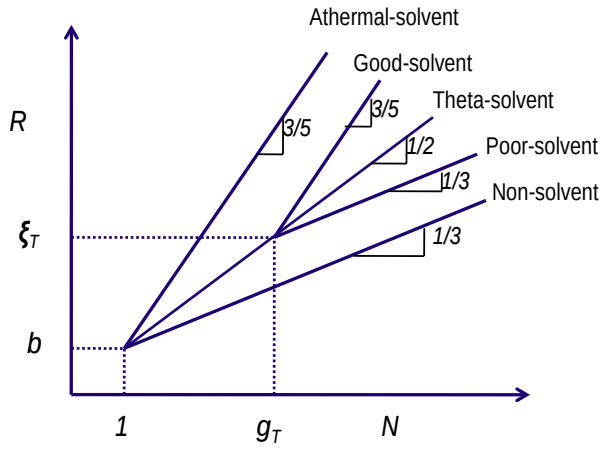

Figure 1.4 – End-to-end distance (R) of dilute polymers in various types of solvents, sketched on logarithmic scales. In a theta-solvent the thermal blob size is infinite. For athermal solvent and non-solvent the thermal blob is the size of a single monomer. Good and poor solvents have intermediate thermal blob size. Reproduced from ref. [7].

1.2 Dynamics of polymers

Whereas standard solids respond elastically obeying Hooke's law (an applied shear stress produces a shear strain in response, the shear strain is proportional to shear stress, $\sigma = E\epsilon$ and the constant of proportionality is the elastic modulus E) and liquids respond in the Newtonian way (an applied shear stress produces a flow with a constant shear strain rate in respond, the strain rate is proportional to the shear stress, $\sigma = \eta d\epsilon/dt$, and the constant of proportionality is the viscosity η), the response of a polymer under applied stress is rather complex. Polymers can behave as a solid (elastic), or a liquid (viscous), or somewhere in between (elastomeric melt) depending on the temperature and on the experimental time scale.

The chain length and its entanglement situation play an important role on the viscoelastic properties of polymers. For the flow of an entangled polymer, polymer chains need to move around other chains (disentangle) to change their positions, *e.g.* when reacting to external shear. Hence, the mechanical behaviour is very different from usual liquids (which are viscous) or solids (which are elastic), leading to the so-called viscoelastic behaviour. Depending on temperature and time scales, the mechanics of behaviour will be either viscous, elastic or a mixture of both. If a stress is applied on a short timescale the material will behave like a solid while for longer times it exhibits viscous flow (*e.g.* "silly putty").

The characteristic time between the solid like and the liquid like behaviour is the relaxation time τ. The approximate relationship between the viscosity η, shear modulus G and the relaxation time is given by $\eta \sim G\tau$. The approximate response of a viscoelastic material is schematically depicted on **Figure 1.5**. Strain rate ($\dot{\epsilon}$) decreases with time in the creep zone, until finally reaching a steady state. In the recovery zone, the viscoelastic fluid recoils, eventually reaching an equilibrium at some small total strain relative to the strain at unloading [8].

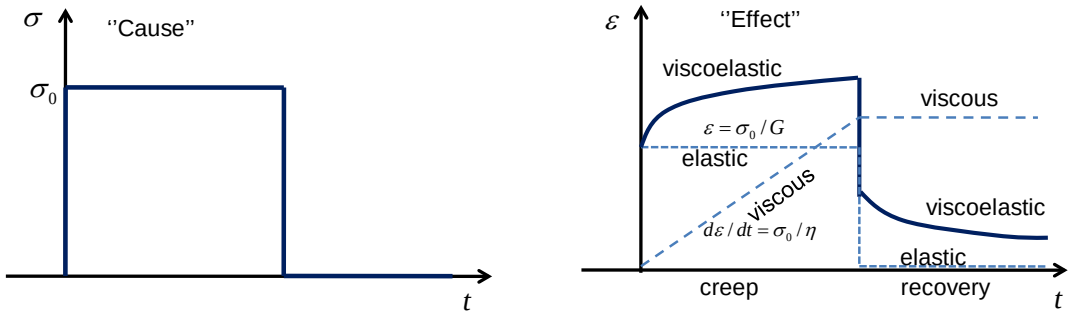

Figure 1.5 – Schematic showing approximate viscoelastic response (indicated by "effect" in right) showing creep and recovery under a constant stress at time zero (indicated by "cause" in left). Reproduced inspired from ref. [8].

So far viscoelastic material properties have been discussed on the macroscopic basis. Further on dynamics of polymer chains will be discussed considering the ideal case of polymer melt. The beauty of polymer physics by considering polymer chains (and statistical scaling relations) irrespective of chemical details of the polymer is also successfully applicable to its dynamical behaviour. For a simple example, Berry and Fox showed that a wide range of chemically and structurally dissimilar polymers display nearly the same molecular weight dependence of viscosity (cf. **Figure 1.6**) [9]. Detailed examination of this plot indicated that for all the polymers up to a certain molecular weight (a critical molecular weight M_c, related with the entanglement molecular weight of the polymer as $M_c \sim (3\pm1)M_e$), the zero shear rate melt viscosity (η_0) varies as $\eta_0 \sim M$. At $M > M_c$ the behaviour changes to $\eta_0 \sim M^{3.4}$. The linear regime of scaling is applicable for low molecular weight unentangled polymer chains described as the Rouse dynamics of polymer melt. The 3.4 power-law regime is applicable for entangled polymers showing reptation dynamics. Any process of non-segmental motion in polymeric melt should be comprised of center of mass motion of the polymer chain, which is important in determining the diffusivity (in terms of viscosity or relaxation time) of a polymer melt.

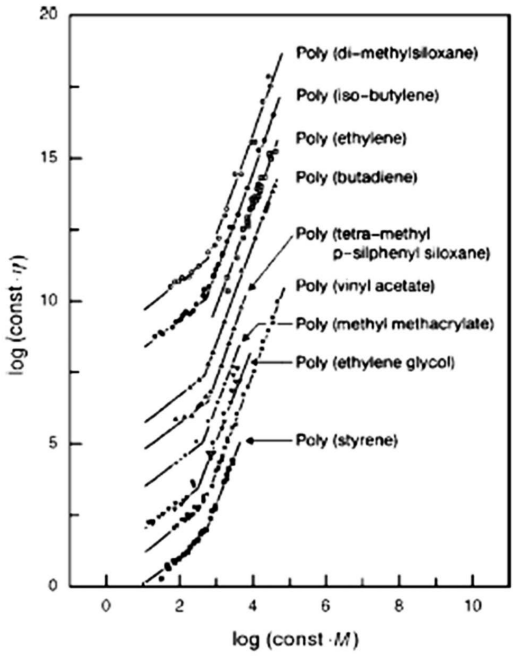

Figure 1.6 – Molecular weight dependence of viscosity as observed for the indicated polymers. For better comparison curves are suitably shifted in horizontal and vertical directions. Data was originally from Berry and Fox [9].

A Rouse chain is comparable to a flexible connected string of Brownian particles that interact with a featureless background viscous medium. In case of polymers, individual particles are comparable with the chain segments following a Gaussian distribution. Further, such repeated segments are connected through imaginary springs; the only interaction is through the spring (cf. **Figure 1.7**). The number of repeat units are less than the entanglement limit, the chain has small N, where $N < N_e$. The principal results are:

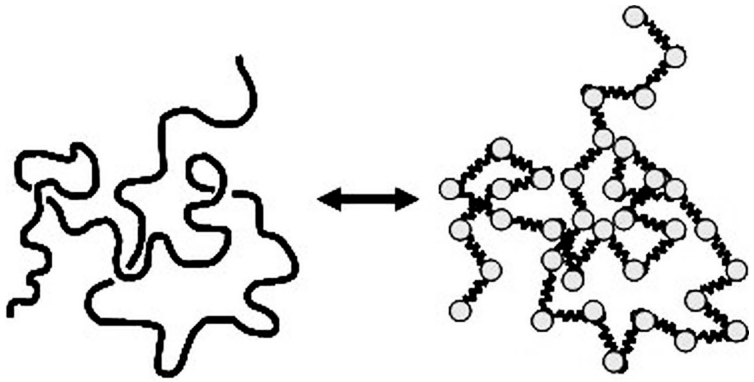

Figure 1.7 – Rouse model, a chain of N monomers is mapped onto a bead-spring chain of N beads connected by springs. Adapted from ref. [7].

(i) Diffusivity of the center of mass depends on the friction factor via Einstein equation: $D_R = k_B T/\varsigma_R = k_B T/\varsigma N$ (here total friction coefficient of chain

$\varsigma_R = N\varsigma$). So, $D_R \sim N^{-1}$. For a particle to move its size R, $\tau_R = R^2/D_R = N^2b^2\varsigma/k_BT$. It means at times $t > \tau_R$, polymer diffuses like a particle of size b, whereas, on shorter times $t < \tau_R$, more complex behaviour of sub-diffusive monomer motion can appear.
(ii) Viscosity (or characteristic relaxation time τ_R, often termed as Rouse time) depends on monomeric friction factor ς and size b as: $\tau_R \sim \eta \sim \varsigma_R b^2 \sim \varsigma N^2 b^2 \sim N^2$.

The idea of reptation dynamics was developed by de Gennes, Doi, and Edwards (1971) [5]. The key idea considers a chain moving inside a tube defined by the surrounding topological constraints. The number of repeat units in the chain is much larger than the entanglement limit, *i.e.* large N, where $N > N_e$. The basic constraint felt by one chain due to all the other chains is that it cannot cross the other chains. This effect can be represented by imagining the considered test chain to be contained inside a tube (cf. **Figure 1.8**). The motion of the

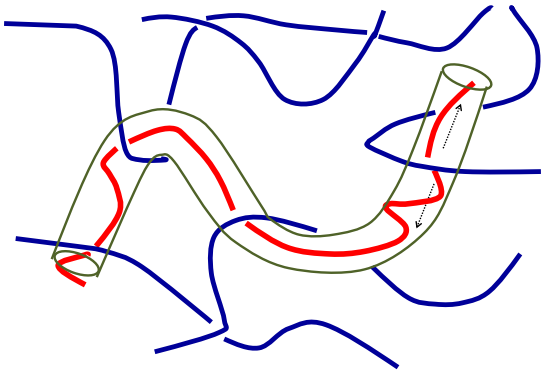

Figure 1.8 – Schematic illustration of an entanglement (reptation) tube. The red chain is undergoing reptation inside the tube while entangled with other blue chains. Scheme inspired by ref. [5].

chain is restricted in the lateral direction of the tube, but the chain may still wriggle along the tube direction. This wriggling motion is called reptation which comes from the idea of reptile like motion. Test chain moves by continuous creation/destruction of its tube. As the chain moves, one end comes out of the tube and a new part of the tube is created. The end of the tube from which the chain has withdrawn is considered destroyed, since it no longer has any influence on the mobility of the test chain. The particular time when the chain moves out of the tube is the longest relaxation time or terminal time known as the reptation time.

The diffusion coefficient of the Rouse-like chain within the tube (not entangled) can be written as: $D_{tube} = k_BT/\varsigma N$. The chain will completely leave

the tube after a time $\tau_{REP} \simeq \langle L \rangle^2 / D_{tube}$, where $\langle L \rangle$ is the length of the tube which is also the contour length of the chain, $L = Nb$. This is also the length of the primitive path of the chain where the potential energy of each monomer is minimum. Here the tube itself undergoes random-walk, which can be thought as random walk of entanglement strands or monomer. Hence,

$$\tau_{REP} = \frac{\langle L^2 \rangle}{D_{tube}} = \frac{\left(Nb/\sqrt{N_e}\right)^2 \varsigma N}{k_B T}$$

$$= \frac{\varsigma b^2}{k_B T} N_e^2 \left(\frac{N}{N_e}\right)^3 = \tau_e \left(\frac{N}{N_e}\right)^3 \tag{1.8}$$

i.e., $\tau_{REP} \sim N^3$. Here $\tau_e \simeq (\varsigma b^2/k_B T) N_e^2$. τ_e is the Rouse time of the entanglement strand containing N_e monomers. This is closely in agreement with the experimental value 3.4. As during the reptation time the chain moves over a distance of its own size hence the corresponding diffusion coefficient: $D_{REP} \simeq \langle L \rangle^2 / \tau_{REP}$, *i.e.*, $D_{REP} \sim N^{-2}$. This is much stronger dependence in comparison to Roussian relationship $D_R \sim N^{-1}$ for shorter unentangled chains. Though the idea of chain reptation was developed theoretically considering the topological constraints around a chain, it has also been observed through fluorescence microscopy. Perkins *et al.* watched relaxation of a labeled and stretched DNA chain along the path of its reptation tube by optical tweezers [10].

It is clear that polymer dynamics is consisting of several types of motions from monomeric, segmental to the whole chain. Time scales of relaxation times for them are also varying from nanoseconds to several years depending on chain lengths and temperature [7]. One can easily visualize different relaxation time scales in a typical plot, showing an approximate variation of the shear modulus (G) with time (cf. **Figure 1.9**). On length scales smaller than the tube diameter, topological interactions are unimportant and the dynamics are similar to those in unentangled polymer melts describable by the Rouse model. The entanglement strand of N_e monomers relaxes by Rouse motion with relaxation time τ_e as, $\tau_e \sim \tau_0 N_e^2$, where τ_0 is the Kuhn monomer relaxation time (shortest relaxation time, $\tau_0 = \varsigma b^2/k_B T$) respectively. According to the Rouse model the stress relaxation modulus on these short time scales decays inversely proportional to the square root of time: $G = G_0 (t/\tau_0)^{1/2}$. At the Rouse time of an entanglement strand τ_e, the chain motion is topologically hindered by surrounding chains. The stress relaxation modulus at τ_e is known as plateau modulus G_e,

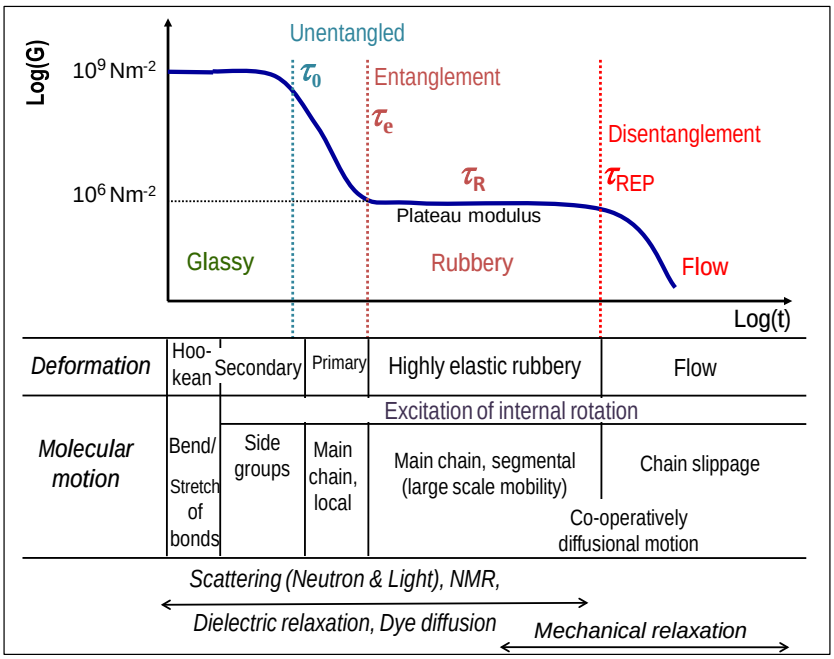

Figure 1.9 – Schematic shape of the complete shear modulus curve of a polymer indicated with possible deformation, molecular motion and relaxation times associated. Scheme inspired from ref. [7, 11].

$$G_e = G(\tau_e) = \frac{\rho R_k T}{M_e} = \frac{k_B T}{V_c N_e} \tag{1.9}$$

Here, V_c is the occupied volume. Rouse time is then,

$$\tau_R = \tau_0 N^2 = \tau_e \left(\frac{N}{N_e}\right)^2 \tag{1.10}$$

Hence from **Equation 1.8**

$$\tau_{REP} = \tau_e \left(\frac{N}{N_e}\right)^3 = \tau_R \frac{N}{N_e} \tag{1.11}$$

1.2.1 Introduction to glassy dynamics of bulk polymers

Nearly sixteen years ago, Philip Anderson wrote, "The deepest and most interesting unsolved problem in solid state theory is probably the theory of the nature of glass and the glass transition" [12]. Almost at the same time, Keddie *et al.* found that a 15-nm-thick ultrathin polystyrene film supported on silica exhibited a glass transition temperature, T_g, that is reduced by several tens of degrees relative to glass transition temperature of the bulk polymer [13]. Since then, hundreds of

studies were published on the area of polymer glass transition, particularly asking how the T_g values are modified by nanoscale confinement. The special case of glassy confined polymer thin films will be discussed in the next section elaborately. Present discussion is particularly focused on the basic phenomenology and theoretical ideas of the glassy state.

If a liquid polymer is cooled down fast enough, the molecules would not have enough time to organize in the configurational degrees of freedom, the system falls out of equilibrium with respect to configurational degrees of freedom and the structure appears frozen on the laboratory time scale, enters a glassy state instead of crystalline state (if it has any crystalline order). This marks the onset of the experimental glass transition. **Figure 1.10** shows a schematic of how the volume of a polymer varies with temperature upon cooling. This trend is similar with entropy (S) and enthalpy (H). If the polymer begins in an equilibrium liquid

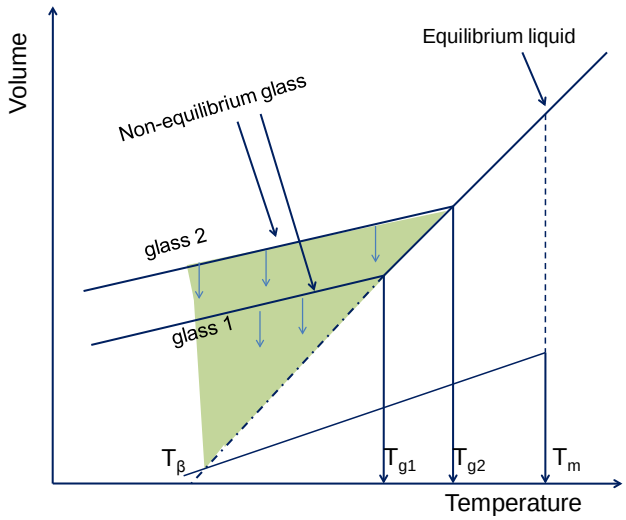

Figure 1.10 – Schematic representation of the specific volume as a function of temperature for a liquid which can both crystallize or form a glass. Highlighted region is affected by physical ageing. Redrawn after ref. [14, 15].

state and is cooled slowly, it will transform into a glass at a given glass transition temperature (T_{g1}), to glass-1. However, if the glass is cooled rapidly (quenched) it will form a glass with a higher volume (glass-2) at a higher glass transition temperature T_{g2}. Glass-2 occupies a higher volume than glass-1, so it will attempt to reach the state of glass-1 through tiny volume relaxations, visually represented by downward arrows from glass. This small volume relaxation is referred to as structural relaxation or physical ageing. Ageing is limited to a temperature range, spreaded between upper limit of glass transition temperature T_g and the lower limit of T_β, the highest possible temperature for secondary β-transition. T_β is close to the Kauzmann temperature T_K [14, 16].

If a crystalline liquid cools sufficiently slowly from T_m to $T \to 0$, its entropy approaches towards zero and becomes zero at a certain temperature, the Kauzmann temperature (T_K) and eventually becomes negative upon further cooling. This impossible scenario constitutes an entropy crisis [14, 15]. The difference between liquid and crystal entropy at the melting temperature T_m can be expressed interms of the difference in heat capacity and Kauzmann temperature as: $\Delta S_m = \int_{T_K}^{T_m} \frac{\Delta C_p}{T} dT$, where ΔS_m is the melting entropy. The entropy crisis arises because the entropy (or heat capacity) of a liquid can not be lower than that of a stable crystal. This fact is also known as Kauzmann paradox. One resolution of this paradox would be the possibility of phase transition (crystallisation) before reaching T_K. In this scenario glass transition is not a kinetic process only rather a thermodynamic phase transition. The entropy crisis is not contradicting with the second law of thermodynamics, as the difference in chemical potential (free energy per unit mass which reduces upon freezing) between the supercooled liquid and the stable crystal at T_K is a positive quantity [14]. As the glass transition takes place before the entropy crisis occurs ($T_g > T_K$), estimates of the Kauzmann temperature involve an extrapolation of liquid properties below T_g, often considered as a lower limit on the experimental glass transition temperature. The validity of such extrapolations, and hence of the very possibility of an entropy crisis, has been questioned by Debenedetti *et al.* [14].

Glass transition can closely be expressed as a second order phase transition process, as the volume (V) (or enthalpy H, entropy S, all are first derivative of free energy G) versus temperature (T) plot shows a change in slope at the glass transition temperature rather than a discontinuity expected from a first order process (such as, for crystalline polymers, there is a discontinuity in specific volume at T_m). However, significant differences exist between truly second order thermodynamic transitions with the glass transition. Such as, the first derivatives of V and H with respect to temperature (*i.e.*, second derivative of free energy G) defining α (thermal expansion coefficient) and C_p (specific heat) exhibit lower value below T_g, than above it [15]. Another difference is found at different cooling rates when T_g shifts to higher temperatures as the cooling rate increases [15]. In the **Figure 1.10** glass-1 is obtained for faster cooling than glass-2. These could not happen for a true second order thermodynamic transition. In other way, no internal thermodynamic equilibrium exists on both sides of the glass transition temperature, indicating the glass solidification or transition process as a kinetic process. The reason that the glass transition temperature depends on the cooling rate of the system is that once the relaxation time of the system becomes larger than the time scale of the measurement, a complete relaxation cannot be seen in

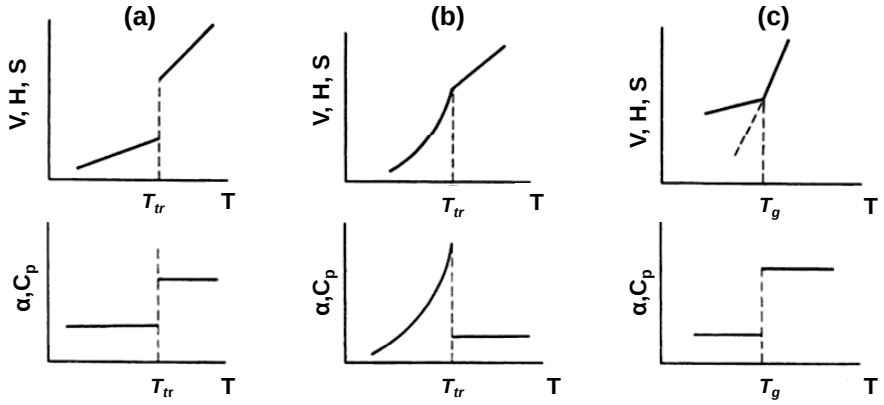

Figure 1.11 – Schematic representation of the changes with temperature of free energy with its first and second derivatives for (a) first order (b) second order (c) glass transition process. Reproduced from ref. [15].

the experiment and the system remains frozen. Measurement at different cooling rates, are probes of different relaxation times.

Due to the cooling down to the glassy state the mobility of the liquid polymer decreases by a large factor of $\sim 10^{13}$. Similarly when a glass is heated up at the point of glass transition viscosity exceeds $\sim 10^{13}$ Pa.s. The dependence of the viscosity (or relaxation time) of a simple liquid on temperature can be expressed by the Arrhenius equation,

$$\tau(T) = A \exp\left(\frac{E_A}{k_B T}\right) \tag{1.12}$$

where A is a temperature independent constant and E_A is the activation energy. Though at low temperatures (close to the glass transition trremperature) substantial deviations are found [14]. Experimental results for many liquids confirm this. This much stronger dependence of relaxation times on temperature is a result of the transition from a liquid to a glassy state. So, mostly Arrhenius behaviour is expected below the glass transition temperature irrespective of the type of glass (either fragile or strong). In general, Arrhenius relation is usually applicable for liquids of some "strong" glasses such as silica glass. But for almost all other liquids form "fragile" glasses including polymer glasses the behaviour of the viscosity can usually be described by an empirical relation called Vogel-Fulcher-Tammann (VFT) equation

$$\tau(T) = \tau_0 \exp\left(\frac{B}{T - T_0}\right) \tag{1.13}$$

where τ_0 and B are temperature independent constants and T_0 is the temperature

at which the system dynamics appears to be diverging [14,17]. The origin of this dramatic slowing down of the dynamics and whether or not it continues below T_g is one of the main questions in the physics of glass transition. Relaxation time appears to diverge at a finite temperature T_0, the Vogel temperature. This temperature is in any case below the glass transition temperature and close to the Kauzmann temperature T_K. It is noticeable that VFT equation implies a "catastrophe" in the relaxation behaviour as the relaxation time becomes infinitely long at a finite temperature, T_0.

Further, Williams, Landel and Ferry found an empirical equation, now called the WLF equation, which fits the dependence of the shift factor on temperature for a large number of amorphous polymers [18].

$$\log_{10} a_T = \frac{C_1(T - T_{ref})}{C_2 + (T - T_{ref})} \tag{1.14}$$

This defines a shift factor (a_T) to determine the relaxation time. C_1 and C_2 are adjustable constants depending upon the material. The WLF and VFT parameters are quantitatively related, $C_2 = T_{ref} - T_0$ and $2.303 C_1 C_2 = E_0/R = B$ [19]. The relaxations responsible for viscoelastic behaviour are the result of various types of molecular motions which are faster at the higher temperature. The shear modulus (G), for instance, is therefore a function of temperature, T and time t, G (t, T). Considering a relaxation experiment from temperature T_1 to temperature T; the effect of a rise in temperature from T_1 is to speed up every stage in a relaxation process by a constant factor that depends on the new temperature T. This is equivalent to saying that the interval of time required for any small change in strain to take place is divided by a factor a_T that depends on T and has the value 1 when $T = T_1$. This means that, if measured values of G (t, T) are plotted against ta_T, curves for all temperatures should be superposed. If time-temperature superposition is possible, this allows introducing a shift factor a_T [20].

1.2.2 Different relaxation processes in glassy bulk polymers

An amorphous polymer usually exhibits more than one transition. There is a high temperature transition, usually labelled as α, which indicates the glass transition and corresponds to the onset of main chain segmental motion. α-relaxation process slows down more rapidly on approaching the glass transition, and it is more affected by vitrification. Therefore, the glass transition is referred to the

temperature where the α-relaxation motions occur on the time scale of the order of 10^2 s. The most prominent features of the α-process close to T_g are the non-exponentiality and the non-Arrhenius temperature dependence of the relaxation time τ_α. These constitute some general signatures of glassy systems. Since α-process is a universal feature of the dynamics of supercooled liquids, it is nowadays generally accepted that it originates from a structural relaxation at the intermolecular level. For polymers, the α-process is based on the idea of a "damped diffusion" of conformational changes (such as gauche-trans transition) along the chain [21]. For an isolated chain, these conformational changes disturb the bond length and also the angles, and enhance the probability that a neighbouring segment will also undergo a conformational transition. Therefore, α-relaxation process is considered as the co-operative motion of polymer chains.

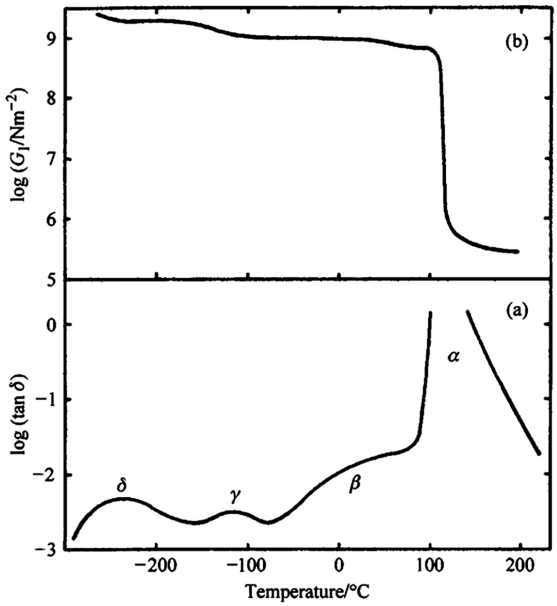

Figure 1.12 – Variations of shear modulus G_1 and tangent δ with temperature for polystyrene. Reproduced from ref. [20].

Secondary transitions may take place at lower temperatures. These are assigned to various types of motion, such as motions of side groups, restricted motion of the main chain or motions of end groups. The secondary relaxations often show up more clearly in the loss modulus or tangent δ. As an example, **Figure 1.12** shows the behaviour of G (real part of the shear modulus known as storage modulus) and tangent δ (loss angle) for atactic polystyrene. Four transitions, labelled $\alpha; \beta; \gamma$ and δ, can be distinguished, with the strongest main peak for α-relaxation being the glass transition. Results from NMR studies suggested strongly that the β-relaxation is due to non co-operative motions involving

both the main chain and the phenyl ring and that the γ transition is associated with 180° ring flips [20]. It is surprising to observe a dynamic motion even in the glassy state mainly dominated by β-process. Johari and Goldstein proposed that this process may be a universal and intrinsic feature of glass forming systems at low temperatures, since it is observed even for rigid molecules having no intermolecular mode [22]. According to them, the β-process itself hindered by its environment, an 'island of mobility' which itself is mobile only through cooperative molecular motions. The actual microscopic nature of the β-relaxation and its possible connection with structural processes still remain unclear.

1.2.3 Phenomenological theories of the glass transition; free volume and conformational entropy

Free volume theories of the glass transition assume that, if conformational changes of the polymer chain backbone are to take place, there must be space available for molecular segments to move into. The total amount of free space per unit volume of the polymer is called the total free volume V_f. The average free volume $v_f = V_f/N$, where N is the number of molecules. It is argued that the fractional free volume v_f can be written as a simple linear function of temperature, as

$$v_f = v_g + \alpha_f(T - T_g) \tag{1.15}$$

where, v_g is the fractional free volume at the glass transition temperature T_g, and α_f is the expansion coefficient of the free volume. The free volume model predicts that from a temperature well above T_g, when the temperature approaches T_g, v_f vanishes and the molecular diffusion is arrested. There is a simple relationship between free volume and relaxation time τ (or viscosity) of the form,

$$\tau(T) = \tau_0 \exp \frac{b}{v_f} \tag{1.16}$$

where, τ_0 and b are constants. This equation follows the VFT equation (**Equation 1.13**) with $B = b/\alpha_f$ and $T_0 = T_g - v_g/\alpha_f$ and also comparable with the WLF equation (**Equation 1.14**). One drawback of the theory is the rather arbitrary assumptions for **Equation 1.15** that makes the theory not really predictive. A comparison with WLF equation yields $C_2 = v_g/\alpha_f$, the predictive v_g value by this equation appears much lower for the amorphous regions of a semi-crystalline polymer [20]. Not all the predictions that the theory does make are confirmed by

experiment [8].

The Adam-Gibbs approach explains the slowing down of the relaxation behaviour of glass forming systems in terms of a decrease of "configurational entropy" [14]. They proposed that any conformational changes require some cooperative motion of a few molecules (cooperative domain). Relaxation is assumed to take place through cooperative rearrangements of groups of molecules (or polymer segments). Any of these groups, called cooperative rearranging regions (CRR), can relax independently from the others. The size of the CRR is related to z, the number of segments inside a CRR having c_1 number of states. When decreasing the temperature the cooperativity increases, leading to an increase of the size of the CRR. In the model the average cooperative transition probability $W(T)$ is given by

$$W(T) = A \exp\left(-\frac{C}{TS_c}\right) \tag{1.17}$$

where $S_c = N_z k_B ln c_1$, C is a constant and A is a temperature independent factor. The relaxation time is reciprocally related to the transition probability.

$$\tau(T) = \tau_0 \exp\left(\frac{C}{TS_c}\right) \tag{1.18}$$

The activation energy is dependent on the number of molecules that have to move co-operatively, what explains the non-Arrhenius behaviour of a glass as the temperature decreases. Using thermodynamic considerations, S_c can be connected to the change of the heat capacitance $\Delta C_p = 1/T$ giving $S_c \sim (T - T_0)/TT_0$ that leads to the VFT equation (**Equation 1.13**).

1.2.4 Phenomenological theories of physical ageing

As already discussed from **Figure 1.10**, after being cooled down from above T_g to a temperature below T_g, the density of a glass becomes higher and the glass would have excess thermodynamic quantities (volume, enthalpy and entropy) and there will be progressive drive towards thermodynamic equilibrium. The movements to establish equilibrium is known as physical ageing involving the relaxation of excess thermodynamic quantities. So, physical ageing is accompanied by a slow decrease of free volume which is reflected by a slow decrease of sample volume. Physical ageing rates can be measured by fitting a straight line to the slope with

graph of volume normalized by the theoretical equilibrium volume V_∞, versus time [23]. The slope of this plot can be defined after Struik as the physical ageing rate as [24],

$$\frac{dV}{dt} = \frac{1}{V_\infty}\frac{V - V_\infty}{\tau} \tag{1.19}$$

τ represents the characteristic relaxation time of the polymer at temperature T. This equation can be presented in terms of free volume v_f as,

$$\frac{dv_f}{dt} = \frac{1}{v_{f_\infty}}\frac{v_f - v_{f_\infty}}{\tau} \tag{1.20}$$

Struik proposed that,

$$\tau = \tau_0 \exp\left(\frac{\Delta E}{k_B T}\right) - \gamma(v_f - v_{f\infty}) \tag{1.21}$$

where ΔE is the activation energy of the relaxation process, τ_0 is pre-exponential factor and γ is a constant.

In a physical ageing process, the specific free volume decreases, which suppresses the segmental mobility, and the suppressed segmental mobility in turn slows down the decreasing rate of the specific free volume. This suggests that physical aging is a self-retarding process, and the equation to describe the ageing process will be non-linear. According to Kohlrausch, Williams and Watts, the relaxation may be considered as an inherently non-exponential process, usually involving the stretched exponential relaxation function $\Phi(t)$, later known as KWW function as,

$$\Phi(t) = \exp\left[-\left(\frac{t}{\tau}\right)^\beta\right] \tag{1.22}$$

in which τ is the relaxation time and $\beta(0 \leqslant \beta \leqslant 1)$ is a stretching exponent [14]. Reasons behind the non single exponential relaxation is still a matter of debate. There are two possible extreme considerations that are able to describe this phenomenon by heterogeneous and homogeneous scenario. In the heterogeneous scenario, the dynamics in one region of a supercooled liquid can be orders of magnitude faster than the dynamics in another region only a few nanometers away. In this case, the relaxation in each region is locally exponential, but the typical relaxation timescale varies spatially. Hence, the response function $\Phi(t)$ becomes non-exponential upon spatial averaging over this spatial distribution of

relaxation times. In an homogeneous scenario, it is possible to imagine that supercooled liquids are homogeneous and that each domain relaxes nearly identically and in an intrinsically non-exponential manner.

Dynamic heterogeneity has been observed experimentally by dielectric spectroscopy [25], nuclear magnetic resonance [26], and other techniques like fluorescence measurements [27,28]. The concepts and experimental evidences for dynamic heterogeneity in glass-forming systems have been reviewed by Ediger [27]. Experiments indicate that the characteristic size of these regions is on the order of few nanometer at T_g. The existence of dynamic heterogeneity has been used to explain the difference in the temperature dependence of translational and rotational diffusion as the glass transition is approached (for $T \leq 1.2\,T_g$) [27]. Recent experiments on ultrathin (ca. 25 nm) polystyrene films revealed heterogeneities could be observed close to the glass transition temperature, but disappear at ca. $1.1\,T_g$ [28]. At higher temperatures, heterogeneities do not exist or they average out on the time and length scales of observation.

Ageing is thermo-reversible. On heating the material to T above T_g, it may reach thermodynamic equilibrium, then ageing history of the sample has been being erased by that process. Ageing therefore is a thermo-reversible process that is reproducible for any arbitrary number of times with the same sample. Ageing is limited to a temperature range, spreaded between upper limit of glass transition temperature T_g and the lower limit of T_β, the highest possible temperature for secondary β-transition (cf. **Figure 1.10**). At T_β the flexibility of the chain segments decreases, since secondary motion becomes frozen. Therefore, segmental motion and ageing will disappear below T_β. So, in principle, ageing should not affect secondary relaxations in bulk polymers. Rather ageing affects the onset of α-relaxation. A common problem to study the exact relaxation process for ageing is the proximal appearance of the β-relaxation peak with the α-relaxation peak, often just as a shoulder of the later. However, there are exceptions where the role of physical ageing on the β-relaxation had been debated [29].

1.2.5 Mobility of glassy polymers induced by deformation

Mobility of supercooled jammed glass even below the glass transition temperature by employing external mechanical stress has been reported by several groups [30–33]. Meijer interpreted yield as “mechanically passing the glass-transition temperature” (European polymer congress 2001 commentary as cited by Reiter)

[34]. Lee and Ediger used an optical photobleaching method to measure the rate of rotation of small dye molecules embedded within thin layers of polymer glasses [30]. These probe molecules provide a direct, local measure of the relaxation by changes in their rotational motion which begins to increase with temperature, adopting the characteristic stretched exponential form of a fluid very close to the glass transition. So, a plastic flow controlled spatially heterogeneous dynamics in glass was observed by external deformation.

Deformation induced mobility is a topic of immense interest especially for polymers as it is related with the mechanical rejuvenation of a structurally relaxed (physically aged) specimen [33]. However, it is not clear whether mechanical deformation actually ''rejuvenates'' a glass in the sense of deleting previous physical ageing history, or whether the process of relaxation is altered in a more complex way by temporarily reaching a different glassy state that undergoes structural relaxation at a different rate. Questions concerning mechanical rejuvenation have been discussed and reviewed in detail by McKenna [35]. Recent work by Lee and Ediger has observed qualitative differences between 'pre-flow' (sub-yield) and 'flow' (post-yield) deformations in the physical ageing characteristics of lightly cross-linked poly (methyl methacrylate) glasses [36]. For deformations in the sub-yield regime, the rotational correlation time of embedded dye returned to the initial trajectory after removal of the applied stress indicating no change in the age of the material. That means deformation at the pre-flow regime cannot delete the ageing history. In contrast, for deformations in the 'flow' regime, the physical ageing process was effectively restarted after the plastic deformation deleting pre-deformation ageing histories. Although the role of external deformation on the enhanced mobility of glassy polymer is clear, the exact structural state of such a glass under deformation is still not clearly known.

1.3 Introduction to glassy thin polymer films

While miniaturization of functional devices demands the thickness of polymer films to reach values even smaller than the diameter of the unperturbed molecule, such films often reveal characteristics strongly deviating properties from those these polymers exhibit in the bulk. The situation can be termed as confined thin polymer films, where in general the film thickness is considered to be less than the radius of gyration (R_g) of the polymer. Already about two decades ago Reiter found enhanced mobility in thin polymer film dewetting [37] and Keddie *et al.* showed the first systematic study of glass transition temperature (T_g)

in thin polymer films with decreasing thickness [13]. Thereafter several diverse measurements have been done on thin polymer films. Several groups have shown anomalous irreversible and reversible density changes after annealing below the bulk glass transition temperature [38–41], unusual ageing [42–45], supposedly faster surface relaxation [46–49], a thickness and history dependent glass transition temperature (T_g) [13, 50–52], distorted chain conformations [53–55], or anomalous dewetting instability [37, 39, 56–58]. These intriguing observations have stimulated an intensive search for a comprehensive explanation in the polymer thin film research community. There are several well written reviews/book chapters which summarize the dynamics of confined polymer thin films [59–62]. Despite of a notably growing literature it is becoming increasingly obvious that a satisfactorily clear understanding of thin polymer film properties has not yet been reached [62]. In the following sections important issues concerning confined polymer thin films will be discussed.

1.3.1 Glass transition of thin polymer films

The first systematic study of the dependence of the glass transition temperature (T_g) on film thickness in thin polymer films was performed by Keddie *et al.* using ellipsometry [13]. Since then, one of the most discussed observations is perhaps the film thickness, (h) dependence of the glass transition temperature, $T_g(h)$, of polystyrene (PS) films. For those PS films supported by silicon wafer, T_g begins to decrease from the bulk value when h is decreased below ca. 50 nm and drops by ca. 30 degrees when h is decreased to ca. 10 nm. A compilation of results obtained for PS films on a variety of substrates using numerous experimental techniques such as ellipsometry, dielectric spectroscopy, X-ray reflectivity, positron annihilation lifetime spectroscopy (PALS), local thermal analysis and probe fluorescence intensity has been shown by Roth *et al.* (cf. **Figure 1.13 a**) [59]. The data were fitted to an empirical function based on the assumption of the existence of a liquid-like layer at the free surface of the film, known as so-called layer model:

$$T_g(h) = T_{g,bulk}\left[1 - (\frac{\alpha}{h})^{\delta}\right] \tag{1.23}$$

where α and δ are fitting parameters with values 3.2 nm and 1.8, respectively, as found by Keddie *et al.* The layer model is by far the most accepted model for the thickness dependence of T_g of polymer films [13, 50, 51, 59, 63, 64].

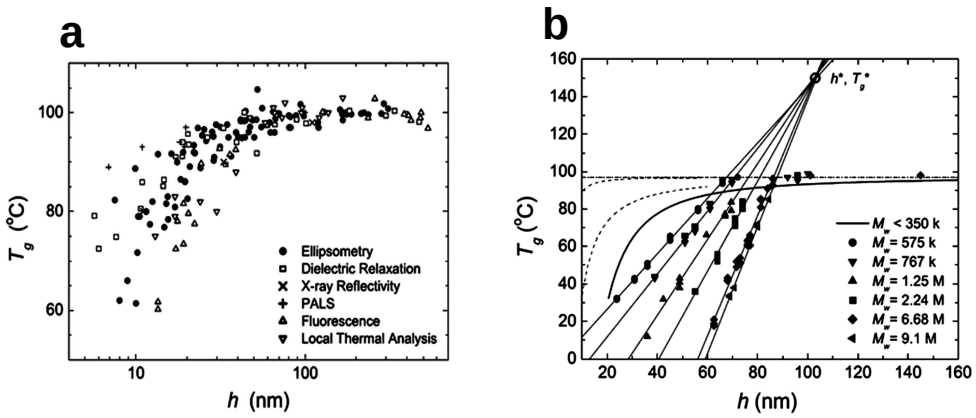

Figure 1.13 – (a) Glass transition temperature T_g as a function of film thickness h measured for polystyrene (PS) of different molecular weights M_w supported on a variety of substrates using six different techniques indicated in the plot legend. (b) Glass transition temperature T_g as a function of film thickness h for free-standing polystyrene films of different molecular weights. High-M_w data, measured using ellipsometry, are displayed using a different symbol for each M_w value, and data for $M_w < 350 \times 10^3$, measured using Brillouin light scattering, are indicated by the thick solid line. The dashed lines for $h < 60$ nm represent the spread and uncertainty in the T_g data obtained for supported PS films. The small circle indicates the common intersection point of the straight line fits to the reduced T_g data for the high-M_w films. Taken from ref. [59].

Generally speaking, it is supposed that the molecular motions near the polymer-air interface are much faster than those in the bulk polymer. On the other hand, the molecular motions at the polymer-substrate interface can be faster or slower than the polymer motions in bulk depending on whether the polymer-substrate interactions are weak or strong, respectively [64, 65]. T_g of a film is a result of the interplay between the effects of the two interfaces of the film. So, a reduced T_g for thin polymer films is interpreted as the influence of enhanced mobility at the free surface and little or no change in mobility at the solid surface. An increase in T_g can be considered as a strong attraction between the polymer and substrate resulting slow dynamics near that interface in comparison to the increased mobility near the free surface [66]. The reduction of T_g of the freely-standing PS films with decreasing h is even more pronounced, with the effect being about twice as large as that found in the supported films [52, 59]. The data show quite different trends for $M_w \geq 575$ kg/mol films and the $M_w \leq 378$ kg/mol films, as a result of which they were referred to as the high-M_w and low-M_w films, respectively (cf. **Figure 1.13 b**). For the high-M_w films, $T_g(h)$ is equal to $T_{g,bulk}$ at large film thicknesses, but starts to decrease linearly with the film thickness below some threshold thickness. This dependence of T_g on h can be interpreted as the interplay between two types of mobility, the bulk mechanism

which dominates for sufficiently thick films, and a new mode of faster mobility.

De Gennes proposed the underlying physics concerning the relaxation of a glassy surface deals with the motion at the segmental scale (sliding motion around the chain loop) and its propagation towards the interior [67]. So the molecular weight of the polymer should not have any effect on it. After the theoretical interpretation by de Gennes explaining the high mobility at the surface layer, notable theoretical contribution on the similar question had been given by Ngai [68]. Considering the coupling (between segmental motions) model he predicted, a large increase of the mobility of the local segmental motions and the lack of such a change for the Rouse modes and the diffusion of entire polymer chains, for the polymer thin films. By using molecular dynamics simulations, Varnik *et al.* showed that an enhancement in the glass transition dynamics could be produced by confining the polymers between two repulsive, impenetrable walls [69]. Later, higher mobility at the thin film free surface has been simulated by Peter *et al.* for non-entangled polymer melt using a coarse-grained (bead-spring) model [65]. Herminghaus *et al.* proposed that the T_g of the films is determined by the fastest surface capillary mode that can penetrate the whole film [70]. As the film thickness decreases, the required wave vector, and hence the relaxation rate of the fastest mode, increases. So, thinner films require a lower temperature to melt. To fit the $T_g(h)$ data, however, the model still requires the existence of a surface mobile layer, which was not considered intially to explain the T_g-reduction.

There are reports showing dynamics are not faster than bulk at the free surface [71, 72]. According to Kremer *et al.*, sample preparation is the key to the conflicting results found in the literature. It all depends on how the films are prepared. Residual solvent can act as a plasticizer, while non-equilibrated films may have metastable states. Both of these effects result in altered dynamics. According to Kremer, annealing of PS at 150 °C in air led to chemical degradation, changing the molecular dynamics. this could be an explanation of T_g-reduction found in the seminal paper by Keddie *et al.* [13]. However, a much more convincing explanation on T_g-reduction in supported thin polymer films has been given by Napolitano and Wübbenhorst [73]. They observed a striking correlation between the deviations from the bulk behavior and the thickness of the polymer layer irreversibly adsorbed at the solid interface. The changes in the properties of polymers at the nanoscale have a finite lifetime which is given by the segmental desorption time. Annealing, favours adsorption and thus modifies the entity of the deviations from bulk behaviour. As the desorption time

might exceed by several orders of magnitude the reptation time, in the case of many polymer/substrate systems, it is not possible to completely remove the T_g shifts introduced by substrate effects. All of these studies essentially emphasize the role of preparation method and motivate our present study to explore the role of out-of-equilibrium chain conformations (produced during preparation by spin-coating) on the relaxation dynamics of polymer thin films.

1.3.2 Residual stresses inside spin-coated polymer films

Spin-coating is a widely used method to prepare polymer thin films. Such film preparation possibly generates residual stresses due to the rapid solvent evaporation during preparation resulting in 'frozen-in' non-equilibrium conformations of polymer chains. Residual stresses obviously have an impact on some still puzzling properties of polymers in the ultrathin film, such as negative expansion coefficient, β ($\beta \equiv (1/h)(dh/dT) < 0$), where T is temperature and h is film thickness) [38, 40, 41], exceptionally fast ageing below T_g [42, 45], dramatically low rubber elastic modulus [74, 75]. Interestingly, the effect of negative expansion coefficient and residual stress can be reduced but typically not removed completely by annealing the film above the $T_{g,bulk}$ of the polymer. These findings illustrate that the non-equilibrium states of ultrathin polymer films, allegedly brought about by the fabrication process, are metastable [39].

Reiter and de Gennes conjectured that rapid solvent evaporation during spin-coating led to a metastable physical polymer network that could lead to negative thermal expansivity and further tried to explain the possibility of early rupture of thinner films [39]. **Figure 1.14** illustrates the key physical stages of the metastable polymer network, starting from the moment it is produced (stage α) to the point where the network structure (stage ϵ) is disintegrated by (sufficiently aggressive) thermal annealing. At stage α, the film has just been solidified from solvent evaporation as the solvent content has reached the characteristic value, ~14-20%, below which the T_g of the polymer solution exceeds room temperature. The following stages β and γ correspond to the ones where the film get completely rid of the residual solvent upon further evaporation (which can take place at ambience). Reiter and de Gennes recognized that the original chain network structure, once formed (at stage α), establishes a rigidity that would resist the film from further volumetric changes [39].

Commencement of rupturing in thinner films was explained to cause by

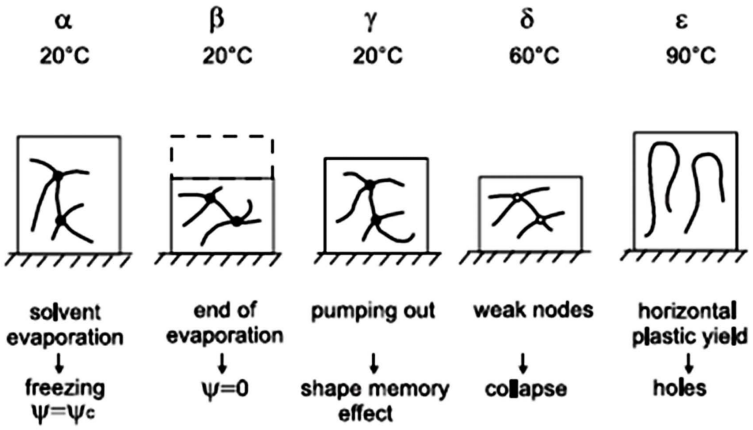

Figure 1.14 – Illustration of the key stages involved in the physical picture proposed by Reiter and de Gennes to explain how a metastable polymer network can result plastic yield in a spin-coated film. Adapted from ref. [76].

plastic yield, which is more probable to occur close but below the bulk-T_g, such as 90 °C. For ultrathin films, the thinner these films, the more the polymer molecules are deformed (which depends on the deviation parameter, $|R^{\perp}-h|/R^{\perp}$, where, h is film thickness and $R^{\perp}$ is the perpendicular size of coil) and so larger stress is stored and the more easily plastic yield can take place. This fact, in turn, gives rise the possibility of greater stress content in the highly squeezed polymer chains confined in the thin film dimensions. The rheological consequences of squeezing a polymer in such reduced dimension should be determined by the response of the entanglement network inside a film to an applied stress. Rowland *et al.* through their flat-punch induced deformation experiment showed, when the film thickness is smaller than the radius of gyration, both the resistance to small scale elastic deformation (contact modulus) and the stress required to induce large-scale plastic deformation (forming stress) are strongly reduced [77].

As all of the puzzling observations in thin polymer films are anticipated to be linked with the residual stresses [62], several attempts has been made to clarify its amount inside a spin-coated thin film, which is already challenging due to the nanoscale dimension limiting the use of conventional stress measurement techniques with appropriate resolution. Residual stress or molecular recoiling stress in polymer thin films was determined from the surface contour around the incipient dewetted holes in polymer thin films by AFM [78]. The recoiling stress was found to be within 1-10 MPa, which increases rapidly with molecular weight while it decreases with increasing film thickness. This is indicative of higher residual stress due to squeezing longer molecules inside the confined thin film. Chung *et al.* used a strain induced surface wrinkling method to determine the residual stress inside a spin-coated PS thin film [79]. Residual stress of ca.

30 MPa was found by them from the measured wavelength of wrinkle patterns. Residual stress has been found to decrease upon thermal annealing above T_g. Thomas *et al.* did direct measurement of residual stress inside a thin spin-coated film utilizing a modified version of conventional beam curvature measurement technique [80]. High molecular weight PS thin film was prepared over a SiN cantilever and the deflection of a FIB (focused ion beam) cut portion was observed under SEM (scanning electron microscopy). Spun-cast films showed surprisingly high residual stress of ca. 135 MPa which was found to decrease upon annealing the film at a temperature above the T_g. Dewetting is an effective tool to probe the residual stress inside a spin-coated film [42,81]. It can be done by heating the spin-coated film at $T > T_g$ after spin-casting. Upon annealing, holes form and grow. Reiter *et al.* showed residual stresses partially relax even in the glassy state of the film [42]. Role of ageing and residual stresses on the dewetting dynamics of thin film is one of the basic aspects of this thesis and will be elaborately described later.

1.3.3 Polymer chain conformations inside a thin film

Polymers confined in a thin film are of immense interest in the area of polymer physics, with a prime focus to interpret the polymer chain conformation and entanglement situation inside the thin film. In the bulk melt state, polymers are considered ideal Gaussian chains which represent random walks with a length scale dependent on the molecular weight, M, as the root-mean-squared end-to-end distance, $R \cong M^{1/2}$. In the polymer melt a polymer chain explores a pervaded volume, $V_p \sim R^3$. Within this same pervaded volume, many other polymer chains can come and can restrict the mobility of a polymer chain due to entanglements, *i.e.*, interactions with other chains through interchain entanglements [53]. Exact conformations representing chain entanglements are not yet known even for bulk polymers, though the statistical nature of entanglements are well described by chain packing models [82,83]. In such models the entanglement molecular weight, M_e, is defined through the ratio of the pervaded volume of a chain, V_p, to the volume occupied by that chain, V_c. According to the chain packing model an entanglement occurs when M is such that ~ 2 chains exist in the same pervaded volume. As chains get larger, they interact with more other chains, thus M_e corresponds to the ratio of $V_p/V_c \sim 2$. One can consider a polymer chain of mass $2M_e$. So, this chain could be confined to the pervaded volume that would be occupied by a chain of mass M_e in the bulk. Thus a chain that was well-entangled in the bulk would be only partially entangled with other chains in the confined situa-

tion. So, the total entanglement density, $\nu = 1/M_e$, consisting of the sum of the self-entanglements and interchain entanglements, remains constant. Interchain entanglements in the bulk are converted to self-entanglements in confinement. It is the fraction of self-entanglements that increases in a confined system because the pervaded volume is smaller in confinement than in the bulk.

Considering bulk polymers as three-dimensional objects, assuming a thickness of the sample $h > R$, one can interpret a polymer thin film as being two-dimensional if $h < R$. An ideal random walk in two dimensions occupies all sites within its perimeter, $R \sim Nb^{1/2}$, b is the length of a segment. Consequently, there is only negligible interpenetration for ideal random walks in two dimensions. One can define the volume fraction of overlap (Φ^*) of a particular chain within its pervaded volume as $\Phi^* = N/R^D$. Here D represents the dimensionality (cf. **Figure 1.15**). For random walks in three dimensions $\Phi^* \sim N^{-1/2}b^{-3}$. Similarly in two dimensions: $\Phi^* = 1.b^{-2}$. Hence it is clear that there are many more chains overlapping in 3D in comparison to 2D. De Gennes expected that polymer chains are slightly swollen and strongly segregated in two dimensions (cf. **Figure 1.15**) [5].

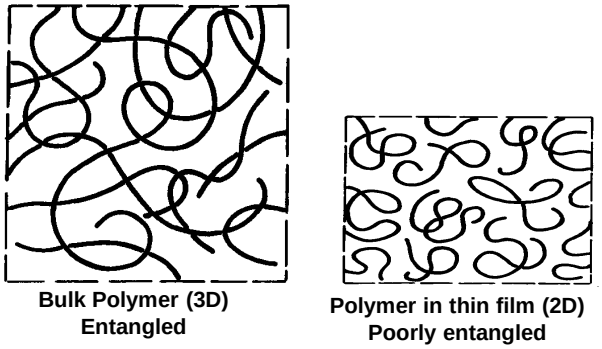

Figure 1.15 – (a) Highly entangled polymer chains in the bulk (3D) polymer. (b) Poorly entangled and segregated polymer chains inside a thin film (2D). Reproduced from ref. [5].

The actual chain conformation of polymer chains inside a polymer film is not clearly known, but several works suggest a possibility of non-equilibrium chain conformations, portraying poorly overlapped chains, reduced inter-chain entanglement density for such sub-R_g confined thin films in comparison to bulk [16, 53, 55, 84, 85]. There are also conflicting observations on the question of entanglement situation inside the film saying no change in entanglement density [86] to enhanced entanglement density (stiffness) [87].

There are several attempts has been made to investigate the entangle-

ment state of a free-standing film experimentally. Si *et al.* studied free-standing PS films which upon the application of uniaxial strain produce crazed structures consisting of a necked region or a craze depth [53]. Their experiment can express the distance between two entanglement points for ideal Gaussian chains before and after applying a strain as a function of film thickness and craze/neck depth. They found lower effective entanglement density in films of thicknesses below ca. 100 nm. For a ca. 30 nm thin film it is lowered by a factor of ~ 2 in comparison to the bulk. Recent work by Rathfon *et al.* on the same question of entanglement situation in the flow-coated thin free standing film has been addressed by probing the life time and break-up of suspended (over lithographically patterned array of micron scale pillars) fiber networks due to capillary thinning [55], in a manner that is consistent with a drastic reduction in inter-chain entanglement. Experimental evidence concerning reduced inter-chain entanglement in a supported thin film (at a film of thickness $h < 4R$) has been given by Mukhopadhaya *et al.* through small angle X-Ray scattering (SAXS) studies [85]. They found a peak in wave vector $S(q)$ nearly at $q = 0$, which grows with decreasing thickness. This peak is attributed to a decreased interpenetration of chains resulting in an enhanced confinement.

Classical theoretical considerations on chain conformations of confined polymers are derived from the Silberberg hypothesis [88]. It states that polymer coils when perturbed by an impenetrable surface are simply reflected at this surface. In that sense, a 3D random walk by a polymer coil can only be perturbed in one dimension (in the direction normal to the interface) without affecting the other two directions parallel to the perturbation (in the plane of the film). Although SANS (small angle neutron scattering) study by Jones and Russell supports the Silberberg hypothesis [16], few other experimental evidences showed an increment of coil size in the surface parallel direction [89], leading to a final correction where strongly perturbed chains show swelling due to the increase of self-density [90]. Such, a change in coil conformation most likely gives rise to a difference in entanglement density. Experimental findings showing reduced effective entanglement density are mostly explainable by the packing model which considers entanglement between two chains when they are in the same pervaded volume. This model only accounts the inter-chain entanglement neglecting the possibility of self-entanglement within a chain. So, the chains in confined thin films have a lowered degree of inter-chain entanglement density, as the volume pervaded by single chain decreases, while the overall monomer density as well as the total entanglement density remains constant [53,54]. Barbero *et al.* performed an electric field destabilisation study on non-equilibrated PS thin films, where

the characteristic onset time of the instabilities, is proportional to the viscosity (hence entanglement) of the film [91]. As-cast films were observed to have a considerably reduced viscosity as compared to the bulk. Annealing the films above T_g, for sufficiently long times prior to destabilisation, resulted in an increase in the measured viscosity. This fact indicates the possibility of reduced inter-chain entanglements in the as-cast film which increases by annealing.

Though most of the studies indicate a lower entanglement density (or viscosity) of polymer chains in a thin film, there are also contradicting thoughts. One of the very recent rheological probes for thin polymer films has implemented by McGraw *et al.* in terms of preparing glassy bi-layer films with height profiles well approximated by a step function [92]. Upon annealing such stepped bi-layer films above the glass transition, the height profiles broaden due to gradients in the Laplace pressure. By using the Stokes equation in the lubrication approximation they have shown that the rate of height broadening is consistent with that expected from polymer rheology in the bulk (viscosity, $\eta \sim M_w^{3.4}$). They observed that the viscosity in as-cast samples was higher than that in annealed samples. Such surprising result of decreasing entanglement density upon annealing was also observed by Tretinnikov *et al.* They showed FTIR spectroscopic experiments on free-standing PS thin films indicating IR bands characteristic of isolated or weakly overlapped chains [84]. These bands increased in intensity with decreasing film thickness and increasing annealing above the glass transition temperature. Assuming that a poorer inter-chain entanglement was responsible for the characteristic peak, annealing lead to a decrease in entanglement density. Results published by O'Connell and co-workers indicated an unusual stiffening in thin films [87]. They inflated micron-sized bubbles inside spin-coated films. They monitored deflation of micro bubbles by atomic force microscopy. From the creep behaviour they drew the conclusion that thin films are stiffer than bulk polymers. The stiffening can be partially explained by the surface tension but the major part of the effect attributed to the unusually highly entangled polymer chains inside the thin film.

1.4 Dewetting as a probe for studying polymer thin films

Dewetting is the retraction of a fluid from a surface it was forced to cover. In general, if a substrate has a lower surface energy than a fluid, this fluid will not form a stable film when deposited onto such a substrate. The opposite process of covering a substrate with a liquid up to the point when an equilibrium state is

reached is called spreading [93, 94]. Spreading and dewetting are important processes for many applications, including adhesion, lubrication, painting, printing, and protective coating. For most applications, dewetting is an unwanted process, because it destroys the applied thin film. Apart from that, these processes are important also in biology, such as for the wettability of surfaces in plants or animals. Wettability of a surface by a liquid is to a large extent characterized by the interfacial tensions and thus by the contact angle (cf. **Figure 1.16 a**). However, consideration of contact angle only cannot provide information on kinetic effects like interfacial friction (energy dissipation) [95, 96]. Spreading/dewetting

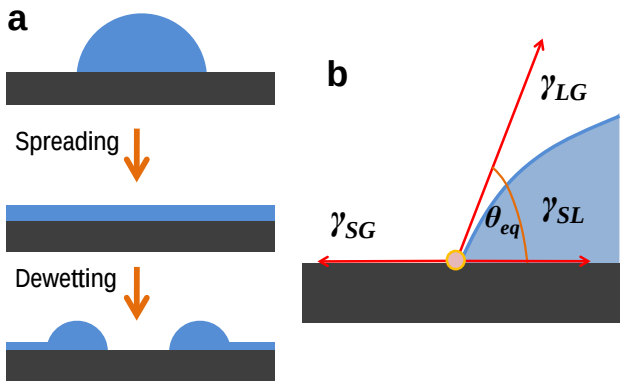

Figure 1.16 – (a) Schematic side-view representation of spreading of a drop toward a thin film and dewetting of an unstable thin film via nucleation and growth of a dry patch surrounded by a rim (cross-sectional view) collecting the removed liquid. (b) Schematic representation of the balance of interfacial forces (represented by the arrows for γ_{SG}, γ_{LG}, and γ_{SL}), which meet at the contact line (indicated by a small circle). This force balance determines the equilibrium contact angle θ_{eq}. Figure redrawn after ref. [96].

is mainly dependent upon short-range forces in the nm or sub-nm range, but long range forces of few tens of nm are also relevant [96, 97]. Because of the complementary process to spreading, dewetting is determined by the same intermolecular forces and the corresponding dissipation route. Both processes can be treated in analogous ways [93, 96]. For spreading or dewetting, the chemistry of the surface is an important controlling factor as well as the process of surface cleaning [97, 98]. Dewetting experiments are attractive because of their rapidity, experimental simplicity and the ability to yield sensitive information on adhesion, friction, slippage etc. of the surface or interface [99]. An ideal liquid for dewetting should have properties like high viscosity (enabling time resolved measurements) and non-volatility (assuring mass conservation). In this context, a thin polymer film is an ideal candidate whose properties can be explored in detail by dewetting studies [96].

1.4.1 Basic theoretical considerations on dewetting of viscous liquid

Contact angle and Spreading:

The simple case of a Newtonian fluid on a smooth and solid substrate can be completely characterized by its viscosity. Viscoelastic and shear thinning or thickening effects are excluded. Gravity (because the mass of the film is extremely small) and inertia (because we investigate cases where the dewetting velocity is comparatively small) can be neglected. The substrate is considered as inert and without the possibility of generating hysteric behaviour, *i.e.* contact line pinning and chemical modifications of the substrate are excluded. At thermodynamic equilibrium (no temperature gradients, concentration gradients, *i.e.*, no net forces are acting) the three surfaces that meet at the three-phase contact line define an equilibrium contact angle (γ_{eq}). The Young equation representing the balance of forces occurring at the three phase contact line can be represented as

$$\gamma_{SG} = \gamma_{SL} + \gamma_{LG} \cos\theta_{eq} \tag{1.24}$$

where, γ_{SG} is the interfacial energy of the interface between solid substrate and the surrounding medium, γ_{SL} is the interfacial tension between substrate and liquid and γ_{LG} is the interfacial tension between liquid and surrounding medium. The spreading coefficient (S), characterizing the tendency of a liquid to spread or not to spread on a substrate, can be represented as

$$S = \gamma_{SG} - (\gamma_{SL} + \gamma_{LG}) = \gamma_{LG}(\cos\theta_{eq} - 1) \tag{1.25}$$

In equilibrium, γ_{SG} can never be larger than (γ_{SL}+γ_{LG}). If it were the case, $S > 0$ indicates that the total free energy (or surface energy) of the system can be lowered by removing the solid-vapour interface. This is the case when the substrate is wetted (covered) by the liquid layer. $S > 0$ ($\theta_{eq} = 0$) is the condition for total wetting. This is possible if the solid to be coated/wetted is initially not in equilibrium with the surrounding medium. Here the initial spreading coefficient can be defined as

$$S_{in} = \gamma_{SO} - (\gamma_{SL} + \gamma_{LG}) \tag{1.26}$$

where γ_{SO} referring the interfacial tension between dry substrate and vacuum. In equilibrium, some liquid adsorbs on the substrate, causing a lowering of γ_{SO} to γ_{SG}. $S < 0$ indicates the condition of partial wetting. Here a liquid drop does

not spread, instead forms a spherical cap. A liquid is said to be "mostly non-wetting" when $\theta_{eq} > \frac{\pi}{2}$ and "mostly wetting" when $\theta_{eq} \leq \frac{\pi}{2}$. The displacement of the three-phase contact line, where the fluid film is meeting with the substrate and the surrounding medium (in most cases this is air), is governed by the balance of driving and resisting forces. For a Newtonian fluid, capillarity represents the main driving force for dewetting. It is related to an imbalance between the three interfacial tensions (γ_{LG}, γ_{SL} and γ_{SG}) which meet at the contact line and are responsible for a dynamic contact angle θ_{dy}. Displacement of contact line from its equilibrium condition requires a deviation from θ_{eq} to θ_{dy}. On an ideal surface the contact angle always tries to (re-)establish its equilibrium value θ_{eq}. Hence, dewetting is thus driven by a capillary force (uncompensated Young force per unit length of the contact line, F_{Young}) which arises from the difference of θ_{eq} and θ_{dy} ($\theta_{eq} \neq \theta_{dy}$). As long as θ_{eq} and θ_{dy} remains valid, the capillary force is negative and the three-phase contact line recedes; the liquid film dewets. Dewetting ends as soon as droplets exhibit their Young's contact angle θ_{eq} on the surface. The driving Young force is

$$F_{Young} = |S| = -\gamma_{SG} + \gamma_{SL} + \gamma_{LG}\cos\theta_{dy} \tag{1.27}$$

Using the relation of equilibrium contact angle for replacing γ_{SG} and γ_{SL} one can get,

$$F_{Young} = \gamma_{LG}(\cos\theta_{dy} - \cos\theta_{eq}) = \frac{1}{2}\gamma_{LG}(\theta_{eq}^2 - \theta_{dy}^2) = \frac{1}{2}\gamma_{LG}\theta_{eq}^2 \tag{1.28}$$

(by expanding the cos-term as $\cos\theta \sim (1 - \theta^2/2)$ for small contact angles and considering ($\theta_{dy} \sim \frac{1}{\sqrt{2}}\theta_{eq}$) [96, 100].

Flow and Dissipation:

Dewetting or removing a fluid from the substrate involves the relative movement of fluid molecules passing each other which results in viscous dissipation within the fluid. The motion of fluid molecules at the substrate causes frictional losses. In general, interfacial friction is responsible for the formation of a rim, *i.e.* the accumulation of the removed fluid from the dried region in a region close to the contact line. Without such friction or in cases where interfacial friction is small compared to viscous dissipation within the fluid, the removed fluid cannot form a rim, rather it gets distributed within the remaining surrounding film, causing an increase in mean film thickness [39, 56]. The work done by capillary forces during

dewetting ($|S|\,V$, where S is the spreading parameter and V is the dewetting velocity is counterbalanced by the work done due to dissipation (F_iV_i, where F_i gives the force per unit length of the contact line and their corresponding velocity is V_i) is

$$|S|\,V = \sum_i F_iV_i \tag{1.29}$$

The energy balance imposes that the viscous dissipations within the liquid film (F_v), and the dissipation due to the friction at the interface with the substrate (F_s), *i.e.* slippage with a finite velocity ($V_s = v(z)_{z=0}$), match the work $|S|\,V$ done by the capillary forces per unit of time with the following balance (the index v stands for 'viscous', s denotes 'slip') [101, 102]:

$$|S|\,V = F_vV_v + F_sV_s \tag{1.30}$$

Depending on fluid-substrate interactions and properties of substrate and fluid, these frictional losses may be localized in a region close to the contact line (no-slip boundary condition). The no-slip condition implies a friction force that is proportional to the liquid viscosity and dewetting velocity. The dissipation is solely due to viscous friction within the liquid. The velocity of the molecules in contact with the substrate is approximately zero (hence, no-slip boundary condition) (cf. **Figure 1.17**). The largest strain rates occur in the direct vicinity of the

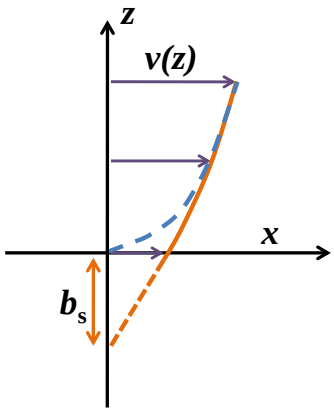

Figure 1.17 – Schematic representation of the velocity profile of liquid flow within a thin film. For the no-slip boundary condition (broken line) the velocity at the substrate ($z = 0$) is zero. In the case of slippage (full line), the liquid velocity is not zero at the substrate surface and only extrapolates to zero at a distance b_s (= slippage length) within the substrate. Figure redrawn after ref. [96].

three-phase contact line [101]. The dissipation is therefore mainly independent

from the size of the dewetting rim. However, the flow geometry (characterized by the dynamic contact angle θ_{dy}) at the contact line influences viscous dissipation. Strict application of no-slip boundary condition would not allow any displacement of a liquid on a solid substrate. Thus, to account for the experimental fact of movable contact lines, various approximations, partially based on proposed molecular mechanisms can be considered [93, 96, 103]. From the hydrodynamic theory based on lubrication approximation which compares the flow in the wedge with flow in a thin film and considers a parabolic velocity profile for a film of local thickness $h(x)$ one can arrive at

$$F_v = \int_{h_{min}}^{h_{max}} \frac{3\eta V_v}{h(x)} dx = \frac{3\eta V_v}{\theta_{dy}} ln \frac{h_{max}}{h_{min}} \tag{1.31}$$

here V_v is the mean of this velocity profile along the z-direction and thus the velocity of the contact line. h_{max} and h_{min} are the maximum and minimum cut-off film thickness limits, within those continuum theory works. These two can be denoted as position Re and Fr of a dewetted hole rim (cf. **Figure 1.18**). In the

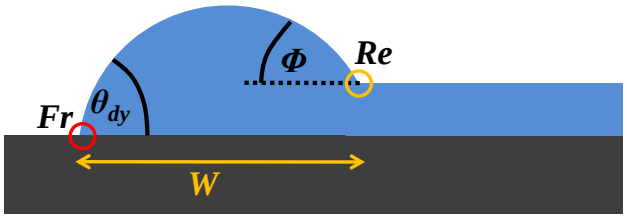

Figure 1.18 – Schematic representation of the rim forming in the course of dewetting of a thin liquid film. At the front position Fr of the rim, the contact angle assumes its dynamic value θ_{dy} and at the rear position Re it takes the value ϕ. The width of the rim is given by W. Figure redrawn after ref. [96].

case of no-slip boundary conditions, the movement of the contact line (position Fr) with dewetting velocity V_v results from a balance between driving force and viscous dissipation in the wedge close to the moving contact line (cf. **Figure 1.18**). So, the viscous dissipation force and the unbalanced Young force should be equated. So, from **Equation 1.28** and **1.31** one can write:

$$\frac{1}{2}\gamma_{LG}(\theta_{dy}^2 - \theta_{eq}^2) = \frac{3\eta V_v}{\theta_{dy}} ln \frac{h_{max}}{h_{min}} \tag{1.32}$$

or

$$V_v = \frac{V_v^*}{6k}\theta_{dy}(\theta_{dy}^2 - \theta_{eq}^2) \tag{1.33}$$

here, $V_v^* = \gamma_{LG}/\eta$ and $k = ln(h_{max}/h_{min})$ [39, 100]. Assuming that the Laplace pressure is the same everywhere within the rim (*i.e.*, the same curvature is assumed to exist everywhere in the rim) requires that $\theta_{dy} \approx \phi$, (cf. **Figure 1.18**). For thin films in the nanometer range and a size of the rim in the range of micrometers, the logarithmic factors at positions *Re* and *Fr* are similar. Consequently, a highly useful relation is obtained between dynamic and equilibrium contact angle for the case of viscous dewetting (with $\theta_{dy} \approx \phi$):

$$\theta_{dy}.(\theta_{dy}^2 - \theta_{eq}^2)\gamma_{LG} = \gamma_{LG}\phi^3 \tag{1.34}$$

Again, considering, $\theta_{dy} = \theta_{eq}/\sqrt{2}$, one can arrive at

$$V_v \sim \gamma_{LG}/\eta\theta_{eq}^3 \sim V_v^*\theta_{eq}^3 \tag{1.35}$$

For growing holes of radius R and dewetting velocity $V_v = dR/dt$, integration of **Equation 1.35** gives a linear proportionality of the radius versus dewetting time t as $R \sim t$.

In case of slipping fluids, similar calculation can be done by introducing an extrapolation length or slippage length (b_s) (cf. **Figure 1.17**). For strong cohesion fluids like entangled polymers, apart from the viscous dissipation within the rim, one may encounter slippage of the fluid on top of the substrate and thus frictional losses originated from the whole region moving (slipping) over the substrate [104]. In the case of slippage, the frictional force F_s (force per unit surface) at the interface between the liquid on the substrate is characterized by a friction coefficient ζ, and proportional to the velocity V_s with which the whole rim of width W is moving past the substrate: $F_s \sim \zeta V_s$. As has been shown by de Gennes, ζ is given by the ratio of fluid viscosity over slippage length, *i.e.* $\zeta = \eta/b_s$ [95, 101]. De Gennes theoretically predicted for the entangled polymer melts on a non-adsorbing surface, slip length b_s in the steady-state flow should increase with increasing chain length, such as $b_s = a(N^3/N_e^2)$, where a is the monomer size, N is the polymerization index, and N_e the number of segments between entanglements [95]. For a slippage length b_s larger than the film thickness h_0, the velocity of the dewetting fluid does not vary significantly in the direction normal to the substrate. Thus, the fluid roughly flows like a plug [104]. As the flow profile is almost constant, in such a case, energy is dissipated mostly (but not fully) at the liquid/substrate interface where the highest velocity gradients exist [102, 105]. Schematic views on the differences of the no-slip or slip boundary condition in the context of dewetting are given in **Figure 1.19 a-b**. In case of

large slippage viscous dissipation may play a minor role. Dissipation occurs along the distance of the solid/liquid interface, where the liquid molecules moved over the substrate. Dissipation can be easily characterized by the rim width (W).

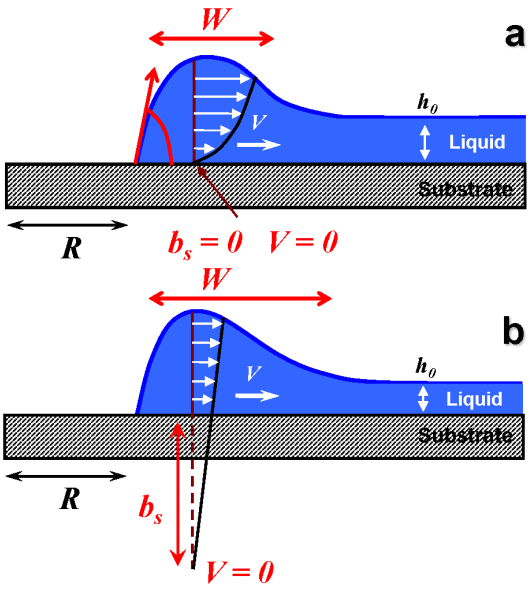

Figure 1.19 – Schematic presentation of late stages of dewetting of Newtonian fluid on a substrate with (a) a non-slip and (b) a slip boundary condition. Adapted from ref. [57].

Thus, the frictional force within the rim (force per unit length of the contact line) is

$$F_s = \zeta V_s W \sim \frac{\eta}{b_s} V_s W \sim \frac{1}{2}\gamma_{LG}\theta_{dy}^2 \tag{1.36}$$

Consequently, for the opening of a hole of radius R in a film of thickness h_0 mass conservation ($R^2 h_0 \sim 2RW^2\theta_{dy}$) lead to ($V_s = dR/dt$):

$$\frac{dR}{dt}(Rh_0)^{1/2} \sim (\frac{\gamma_{LG}}{\eta})b_s\theta_{dy}^2 \tag{1.37}$$

or

$$R^{3/2} \sim (\frac{\gamma_{LG}}{\eta})\theta_{dy}^2(b_s/h_0)^{1/2}t \tag{1.38}$$

For the polymer films where the film thickness (h_0) is smaller than the slip length b_s, a characteristic length (Δ_0) has been determined by Brochard-Wyart *et al.* [106]. Stress propagation in films is limited to that characteristic

length, $\Delta_0 \sim (h_0 b_s)^{1/2}$, which is related to the transition between an initial fluid flow viscous dissipation dominated regime to a regime where dissipation due to friction at the film/substrate interface controls the dewetting velocity [107, 108]. Eventually, Δ_0 is similar to the rim width (W). For a hole radius $R < \Delta_0$, *i.e.* during the regime of building up of a rim, the capillary driving force for dewetting can be expressed by the dissipation of the capillary energy, essentially within the fluid. Here the viscous dissipation dominates over the dissipation due to the interfacial friction. Then, the opening dynamics are exponential ($R \sim \exp(t/\tau)$, where τ is the relaxation time), and no rim can be detected. For larger hole diameters such as $R > \Delta_0$, frictional dissipation at the solid/fluid interface starts to dominate over the viscous dissipation within the film. The shape of a rim has no influence on the dewetting dynamics which gets comparable to the one for a straight edge dewetting geometry. The birth of a rim is observed with a rim width (W) proportional to a characteristic length (width) Δ_0 and a constant dewetting velocity

$$V_s = \frac{|S|\,.b_s}{\eta}\Delta_0^{-1} \tag{1.39}$$

At later stages, in the mature rim regime (when dewetted distance $R \geq b_s$ and W much larger than Δ_0), V_s decreases with time t according to $V_s \sim t^{-1/3}$, giving the law $R \sim t^{2/3}$ (cf. **Equation 1.38**), which is usually used to infer dewetting with strong slippage [57, 104, 106]. In the absence of a solid or liquid substrate (*e.g.*, hole opening in a free-standing film) the velocity profile within the film corresponds to true plug flow, b_s thus becomes infinite, and only the first regime (exponential growth) is observed ($R < \Delta_0$, for all times) [58, 108].

1.4.2 Dewetting of viscoelastic polymer thin films

It is well known that capillary forces resulting from intermolecular interactions are capable to retract a purely liquid film from a solid surface. It is somewhat surprising to see similar dewetting phenomenon for viscoelastic films where, on the timescale of the experiment, the material cannot flow like a liquid, rather it behaves like an elastic body. Experiments on thin polystyrene (PS) films at temperatures not too far above the glass transition temperature are of that kind, which contributed a lot for the study of thin polymer film properties through several studies performed specially in the last decade and still under immense interest for investigation with increasing number [39, 42, 57, 81, 102, 105, 109, 110].

To study the dewetting phenomenon of highly elastic PS films, process of hole growth could be followed from the very early stages. At the first place, a wealth of information on the elasticity can be expected from temporal evolution of a dewetting hole and the rim collecting dewetted polymer. To reduce the resistance from interfacial friction, the choice of highly non-wettable substrate can be achieved by using PDMS-coated Si-wafers. This PDMS-coating "screened" all heterogeneities of the solid substrates and thus represented an ideally homogeneous surface of low surface tension and rather low interfacial friction for the moving PS-film.

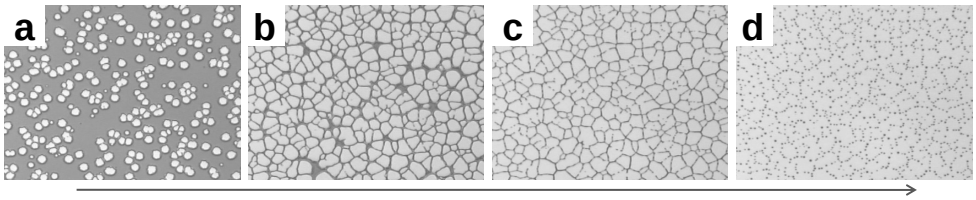

Figure 1.20 – Optical micrographs (size of each: 806 x 645 µm^2) showing dewetting of a thin film of polystyrene (M_w = 4840 kg / mol, h = 40 nm) nucleation and growth on a silicon substrate coated with a monolayer of adsorbed PDMS (M_w = 139 kg/mol, thickness = 11 nm). The temperature of dewetting is 180 °C. At the end, a multitude of dewetting droplets were arranged in polygons. The time between images is about 30 s. Adapted from ref. [111].

During dewetting from the substrate, holes grow and a rim is formed at the three-phase contact line due to the conservation of polymer volume, if a sufficient film-substrate interfacial friction exists. Further propagation of dewetting proceeds with the growth of the holes until the rims of the adjacent growing holes touch each other, forming an interconnected structure of polymer, which is often referred to as the polygonal or cellular pattern (cf. **Figure 1.20 c**). The polymer ribbons subsequently break down due to Rayleigh instability, forming a polygonal array of isolated polymer droplets, as shown in **Figure 1.20 d**. In principle, the final stage of dewetting is given by such equilibrium configuration of liquid droplets ideally of single curvature since the Laplace pressure should be same. **Figure 1.20** is showing different stages of dewetting of a thin viscoelastic PS film over PDMS.

One of the earliest reports on viscoelastic dewetting of PS on PDMS coated Si-wafer was from Reiter [39]. AFM results for the early stages of hole formation obtained from the thinnest films showed most holes were formed within a narrow time interval at the very beginning. Interestingly, these holes initially do not show any rim. This implies that the material removed from the holes had been distributed throughout the remaining film. Surprising rheological behaviour of the polymer has been noticed, as during these initial stages of dewetting, the

molecular weight of the polymer does not seem to play any significant role. After 10 min of annealing at 105 °C the hole size of two different molecular weights (differing by nearly a factor of 30) thin polystyrene films appears nearly the same. Further, somewhat thicker films were used in order to have fewer holes so that one can follow the different stages of hole growth up to much larger hole diameters. In addition to this, higher temperature was chosen, still close to the glass transition temperature ($T_{g,bulk}$ of PS is ca. 105 °C). As the annealing time increased, hole diameter became progressively larger. Later stages of hole growth, *i.e.*, at diameters larger than about 1μm clearly showed the formation of rim (cf. **Figure 1.21 b-c**). Such a transition is expected as soon as the viscous dissipation

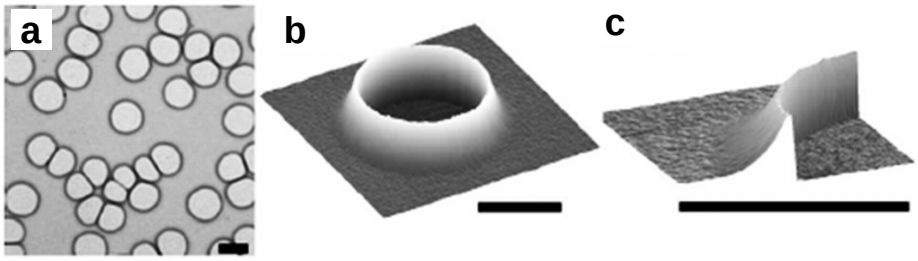

Figure 1.21 – Typical examples for holes and the corresponding rim formed in a 24 nm thick PS film. This film is thick enough for holes being separated by several μm on average. (a) Optical micrograph after annealing for 80 min at 120 °C. AFM images (b) and (c) focus on the asymmetric shape of the rim. The length of the bar represents 5 μm in each case. Adapted from ref. [39].

at the substrate-film interface is getting important. Initially the removed material (related to the dewetted hole radius, R) has been redistributed within the film over a certain distance Δ_0 which is characterized by film thickness h_0 and frictional properties:

$$\Delta_0 \sim \left(\frac{h_0\eta}{\zeta}\right)^{1/2} \tag{1.40}$$

with ζ being the friction coefficient at the interface and η the viscosity of the film [102]. As the dewetted hole radius (R) gets larger than Δ_0, dissipation as well as friction at the substrate/film interface become important. As a result of such friction, the velocity is damped over the distance Δ_0 within the film. As a result, a highly asymmetric rim is observed, with a steep side reaching a height H next to the three-phase contact line and an approximately exponential decay on the other side, with a decay length Δ_0 (cf. **Figure 1.22)**. The highly asymmetric shape of the rim indicates that the polymer is not flowing like a liquid but rather behaves like a solid. For a viscous fluid, one could expect

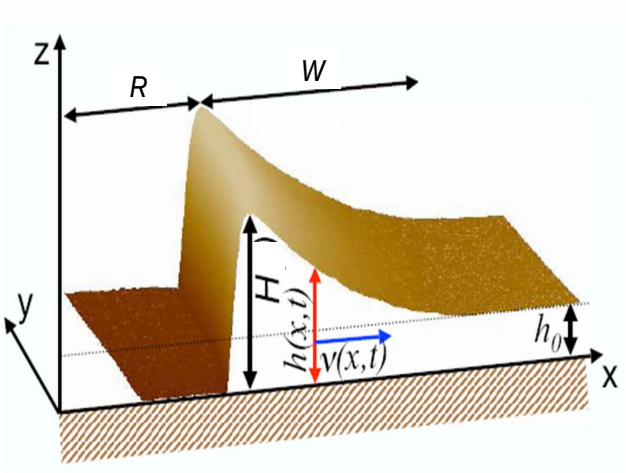

Figure 1.22 – 3D-view (measured by atomic force microscopy) of a section of a typical hole obtained by dewetting a polystyrene film on a PDMS-coated substrate at temperatures close to the glass transition of PS. $h(x,t)$ is the profile of the film, h_0 is the initial height of the film, H is the height of the front, R is the dewetted distance, W is the width of the rim, and $v(x,t)$ is the velocity inside the film. Adapted from ref. [42].

equilibration of the Laplace pressure (which is proportional to curvature) through viscous flow during the experiment. This can lead to a more symmetric rim shape (mature rim). The asymmetric shape of the rim is a characteristic feature of dewetting of viscoelastic fluids at temperatures close to T_g, which changes further during the course of dewetting [109]. The transition from a highly asymmetric rim to a more symmetric mature rim shape characterizes the transition from elasticity to viscosity dominated dewetting. All these experiments demonstrate that a thin film does not need to be purely liquid in order to allow for dewetting. At that time, it was concluded that the intermolecular interactions responsible for capillary forces may be sufficiently strong to plastically deform the thin and almost glassy polymer films. A simple comparison of the acting stress S due to capillary forces [$\sigma \sim S/h_0 \sim$1 MPa (with S = - 20 mN/m and $h_0 \sim$ 20 nm)] with the plateau modulus (G) of PS ($G \sim$1 MPa) supports this possibility. Changes in film morphology were also found to occur below the glass transition temperature (T_g) supporting the idea of plastic deformation [34].

1.4.3 Role of residual stresses on viscoelastic dewetting

Further advancement on dewetting phenomena in thin polymer films incorporates the role of residual stresses on dewetting dynamics [42, 81, 102, 105]. Residual stress is generated during rapid evaporation of solvent during spin-coating of

polymer solution, leading to a frozen-in non-equilibrium conformation of polymer chains. Reiter *et al.* studied the effects of physical ageing on thin PS films coated over a PDMS coated non-wettable Si-wafer [42]. They found growth of the rim width (W) follows a logarithmic function of dewetting time until it reaches a maximum. Further, it remains constant or may decrease. This maximum in rim width defines the beginning of the transition of rim shape from an asymmetric towards symmetric. The time taken by the rim to reach the maximum value (W_{max}) is considered as the relaxation time of the residual stresses denoted as τ_1 (cf. **Figure 1.23 b**). The non-monotonous behaviour of rim shape has been interpreted by the viscoelasticity of polymer (PS), the nonlinear friction at the interface of PS/PDMS and the extent of residual stresses present in the film of PS. Theoretical models can describe quite well the asymmetric shape of the rim, and can also explain the dynamics of dewetting. During the early stages of rim build-up, both the dewetted distance and rim width increased in a logarithmic fashion in time, up to a time τ_1 when W reached a maximum (cf. **Figure 1.23 a-b**). Correspondingly, V decreased continuously according to $V \sim t^{-n}$. Around τ_1 the exponent changed from -1 to -1/2, and after the reptation time it changes to $\sim$ -1/3 (cf. **Figure 1.23 c**). The logarithmic time dependence of R and the corresponding t^{-1} decrease of V are not expected for a Newtonian liquid and indicate the viscoelastic behaviour of the polymer film during the experimentally accessible time. Later we can see that is indicative of the presence of residual stresses inside the film.

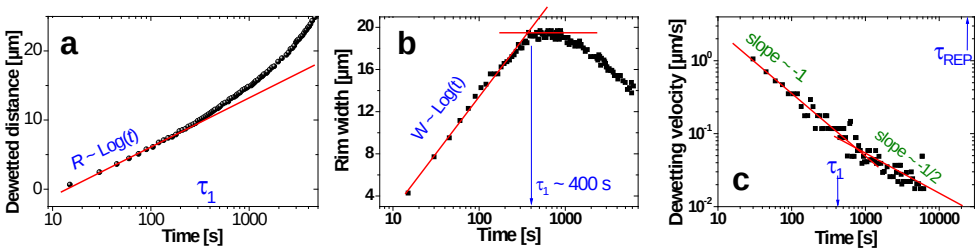

Figure 1.23 – Typical results for dewetting of PS thin films on a non-adsorbing substrate. (a) Dewetted distance R from the edge versus t. (b) Width of the rim W versus t. (c) Dewetting velocity V versus t. The data were obtained for a 65 nm thick PS (M_w = 390 kg mol^{-1}) film at 140 °C. The characteristic time τ_1 is indicated. Under the conditions of the experiment, τ_{REP} of the polymer is about 25,000 s. The lines in c represent expectations from theory, that is $V \sim t^{-1}$ for $t < \tau_1$ and $V \sim t^{-1/2}$ for $t > \tau_1$. Adapted from ref. [42].

Physical ageing experiments by Reiter *et al.* showed that the maximum width of the rim (W_{max}) decreases with time of ageing in an almost exponential

way (cf. **Figure 1.24**), exhibiting a characteristic decay time $\tau(W_{max})$ [42].

$$W_{max}(t_{ageing}) = W_{max}(\infty) + W_{max}(0)\exp(-t_{ageing}/\tau(W_{max})) \tag{1.41}$$

Interestingly, the time when the rim reaches the maximum (τ_1) is not affected by the duration of ageing. They also studied the probability of rupture of the film, defined by N_{max}, the maximum number of holes per unit area as a function of ageing time of the film. The aged films showed a significant decrease in the number density of holes (cf. **Figure 1.24**). The maximum number of holes (N_{max}) decreases exponentially with ageing time similar to the W_{max} behaviour.

$$N_{max}(t_{ageing}) = N_{max}(\infty) + N_{max}(0)\exp(-t_{ageing}/\tau(N_{max})) \tag{1.42}$$

Later, we will see (in **Chapter 3**) that the dewetting velocity (or radius, R) and

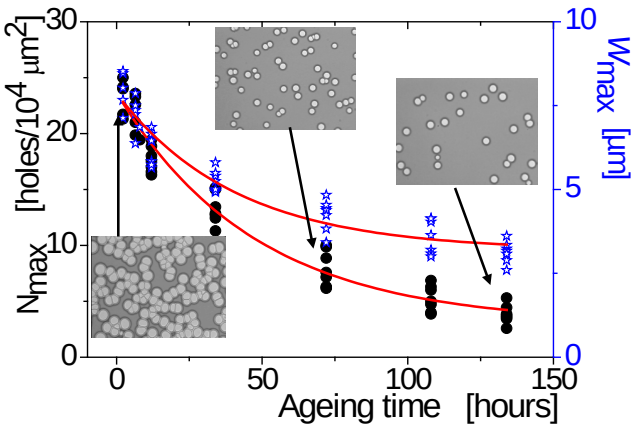

Figure 1.24 – A systematic study of W_{max} (blue stars) and (b) N_{max} (black hexagons) PS films (thickness = ca. 40 nm, M_w = 4060 kg/mol), stored at 50 °C for various times. The insets show some typical corresponding optical micrographs (310 × 230 μm^2). The solid lines represent the fit to the exponential equations described in the text. Adapted from ref. [42].

the rim height (H) also follows a similar exponential decay as

$$R(t_{ageing}) = R(\infty) + R(0)\exp(-t_{ageing}/\tau(R))$$

and

$$H(t_{ageing}) = H(\infty) + H(0)\exp(-t_{ageing}/\tau(H)) \tag{1.43}$$

Value of all the relaxation times (or decay times) found from different measurements, such as $\tau(W_{max})$, $\tau(N_{max})$, $\tau(R)$ and $\tau(H)$ were found to be in agreement to each other. All of these observations indicate that the residual stress (dominant driving force for dewetting) decreases exponentially with ageing, as the polymer chains try to adopt an equilibrium conformation.

Experimental results by Bodiguel and Fretigny also indicated the role of residual stress and friction on dewetting [56]. They found the absence of a rim in their experiments during dewetting of PS film on liquid substrate. They concluded that rim formation can not be due to the intrinsic properties of the film, and as it is only observed on rigid substrate, it is probably due to friction effects. Lateral contraction of the film throughout the global film shape indicated the presence of residual stresses inside spin-coated film irrespective of the substrate. Annealing of the films could verify that residual stress plays an important part in the dewetting of non-annealed films, and found an unusual slow relaxation process occurring during annealing.

In the case of dewetting of purely elastic films, for the time regime $\tau_0 < t < \tau_{REP}$, one can expect a drastic influence of elasticity on rim formation. The strain, ϵ, can be approximately represented in terms of the dewetted distance, R and width of the rim, W, by using the volume conservation as: $\epsilon = (H - h_0)/h_0 \sim 2R/W$ (cf. **Equation 1.48**). This relation between R, W, H, and thus ϵ, was confirmed by atomic force and optical microscopy [81]. The rim height first increases continuously with the rim width up to its maximum value, in agreement with the theoretical model proposed by Vilmin *et al.* [102]. In experiments [81], the deformation of the viscoelastic fluid was given by the relation

$$\epsilon = \frac{\sigma}{E} = \frac{\sigma_{S+}\sigma_0}{E} \tag{1.44}$$

This is further determined by capillary stress at the film, $\sigma_S = S/h_0$ (S =10^{-2} N/m^2, being the spreading coefficient of the film of thickness h_0), residual stress (σ_0) and elastic modulus (E) [81]. Damman *et al.* separately calculated the capillary stress and residual stress. **Figure 1.25 a** clearly shows that the observed elastic deformation calculated from the dewetting morphology, $\epsilon = (H - h_0)/h_0 \sim 2R/W$, is one order of magnitude larger than the strain calculated from the bulk equilibrated PS films, using $\epsilon \sim S/h_0 E_{bulk}$. This fact indicates the presence of residual stress inside the film. The evolution of strain with molecular weight is

even more interesting (cf. **Figure 1.25 b**).

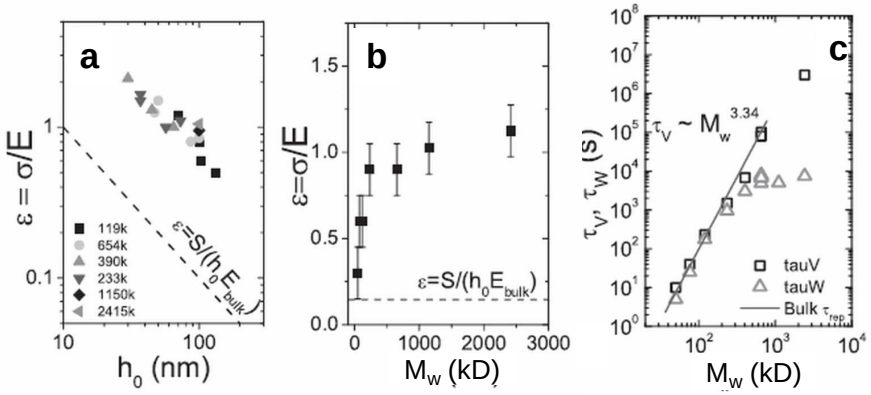

Figure 1.25 – Evolution of the strain, $\epsilon = (H - h_0)/h_0$, with (a) film thickness (M_w as indicated) and (b) molecular weight (h_0~100 nm). The broken line in both graphs corresponds to the strain which would be expected for equilibrated PS films: $\epsilon = S/h_0E_{bulk}$. (c) Evolution of the relaxation times τ_W and τ_V deduced from the rim width and the dewetting dynamics with molecular weight (dewetting temperature 403 K). The film thickness was set at 100 nm. The solid line corresponds to bulk reptation times as determined from rheological measurements. Adapted from ref. [81].

For equilibrated PS films, at constant film thickness, elastic deformations should be independent of molecular weight (the elastic modulus is determined by the entanglement molecular weight, M_e). Instead of that, they observed a large increase of strain with chain length, which saturates for molecular weight larger than 300 kg/mol. The behaviour of the shortest studied PS chains is close to the one of equilibrated bulk polymers. Interestingly, from the molecular weight 300 kg/mol, the τ_W values of their PS thin film saturate and deviate from the bulk τ_{REP} values (cf. **Figure 1.25 c**). τ_W corresponds to the time during dewetting at which the rim width reaches its maximum value, similar to the τ_1 used in the theoretical description of dewetting [102]. τ_V values were found to be in agreement with the τ_{REP} values of the bulk polymer irrespective of molecular weights of polymers used in that study. τ_V also represents the time when rim fracture takes place corresponding to a transition of the behaviour of dewetting velocity from $V \sim t^{-1}$ to $V \sim t^{-1/3}$.

Observations by Damman *et al.* indicated several interesting points which need to be emphasized [81]. High strains were observed even for film thicknesses much larger than the unperturbed dimension of the chains represented by the end-to-end distance of the polymer coils (R). Thus, chain confinement can be ruled out as the cause for high values of ϵ. As ϵ is given by the ratio of $\epsilon = \sigma/E$, the explanation of high values of ϵ may be linked to both, large resid-

ual stresses and/or small elastic modulus. High value of total stress (σ) can be due to the large residual stresses inside the film which were supposed to be due to frozen-in strongly out-of-equilibrium conformations of polymer chains. These conformations have been generated by rapid solvent evaporation in the course of film preparation. Because in solution the chains were rather diluted but they did not have sufficient time to establish the equilibrium state during the process of spin-coating. Most of the literatures found lower entanglement density in films of thicknesses below ca. 100 nm, by a factor of ~ 2 in comparison to the equilibrated bulk system [53, 55, 84, 85, 112]. Lower entanglement density is possibly indicative of a lower elastic modulus (E) in such thin films [74, 75].

1.4.4 Theoretical approaches on viscoelastic dewetting considering residual stresses

Ever since the early theoretical description by Brochard-Wyart *et al.*, which was primarily used to describe a viscous fluid [106, 107], enormous efforts had been engaged on the complete description of dewetting, especially in viscoelastic thin polymer films [102,105,113–116]. Until the role of residual stress on dewetting was recognized, the important experimental findings on viscoelastic polymer films on a slipping substrate which needed to be explained are the following: (i) the radius of the hole increases with time in an exponential manner (short time behaviour); (ii) the growth slows down considerably at long times (iii) the hole grows with a highly asymmetric raised rim. Although the first two observations can be well described by the theoretical descriptions by Brochard-Wyart *et al.* [106, 107], the explanation of asymmetric shape of rim was not provided.

In order to explain this deviation from the behaviour of simple Newtonian liquids, theoretical models assuming radial geometry, have been proposed independently by Saulnier *et al.* considering shear-thinning properties of polymer fluid [113] and Shenoy *et al.* considering a viscoplastic strain-hardening power law solid [114]. Later, experiments by Damman *et al.* revealed the existence of a highly asymmetric rim and a strong decrease of the dewetting velocity during rim build-up for both the radial and the straight edge geometries [109]. This observation limited the previous ideas only applicable to radial geometry and demanded a unified model of description. Vilmin and Raphael considered interfacial friction and viscoelasticity in thin film responsible for the asymmetric shape of the rim, both for the radial and straight edge geometry of dewetting [102, 116]. The rim profile can be represented as in **Figure 1.22**.

The dewetting dynamics of such viscoelastic thin films can be described by a *Jeffrey rheological model* considering E the elastic modulus (mainly due to chain entanglements), η_0 a short time viscosity (mainly due to intra-chain movements) and η_1 the melt viscosity. The time response of such a fluid can thus be divided into three regimes. At short or long times ($t < \tau_0$) or ($t > \tau_1$); the liquid behaves like a simple Newtonian liquid with small (η_0) or large (η_1) viscosities, respectively. Relaxation time, τ_1 can be compared to the reptation time of the chains. But experimentally τ_1 is found to be significantly shorter than the reptation time, particularly for high molecular weight bulk polymers [42,81,116]. This might be consistent with the fact that the entanglement length should be longer in thin confined films [53,55]. At times longer than the reptation time, the polymer chains start to flow as a viscous fluid of high viscosity and thus the decrease in dewetting velocity is described by the classical power law related to viscous dewetting on slippery substrates, $V \sim t^{-1/3}$. For the intermediate regime, the liquid behaves like an elastic solid of modulus E and in this regime the height of the rim increases very slowly with time as

$$H \approx h_0 + |S|(1 + t/\tau_1)/E \tag{1.45}$$

or (for $t << \tau_1$)

$$H \approx h_0 + |S|/E \tag{1.46}$$

Assuming that only capillary stress (S/h_0) is acting at the contact line, with $|S|$ being the spreading coefficient. Energy balance approach by Brochard-Wyart, Vilmin *et al.* assumed viscous dissipation within the film is nearly of the same order as the dissipation due to interfacial friction [102,106]. So the energy balance (per unit of length) between the work done by the capillary force per unit of time and the dissipation due to friction is

$$|S|V \approx \zeta W V^2 \tag{1.47}$$

here V is the dewetting velocity and W is the rim width. This width can be expressed by the volume conservation with the dewetted distance R and rim height H as

$$W \approx h_0 R/(H - h_0) \tag{1.48}$$

Combination of **Equation 1.47 and 1.48** results in a scaling law describing the dewetting dynamics:

$$|S|V \approx \zeta.V^2.h_0R/(H - h_0) \tag{1.49}$$

The experimental results for short times showed that the evolution of the velocity follows a $t^{-\alpha}$ law ($1/2 < \alpha < 1$), which cannot be described by a model based solely on the viscoelastic nature of the polymer and sliding chains. The only way to model this behavior is to consider the presence of residual stress and a nonlinear friction [102]. Vilmin *et al.* showed that the combination of residual stress and a nonlinear friction law can reproduce the unexpected experimental observations of the non-monotonous behaviour of the rim width and the speed of dewetting according to the law $V \sim t^{-\alpha}$. Theoretically, the role of residual stresses to the dewetting dynamics is equivalent to an additional driving force ($h_0\sigma_0$), in parallel to the capillary forces. However, this additional force will decrease during dewetting. Addition of the power $h_0\sigma_0 V$ to the left-hand side of **Equation 1.49**, can lead to an increase of the initial dewetting velocity (V_i) by a factor $\left(1 + \frac{h_0\sigma_0}{|S|}\right)$, with S being the spreading coefficient. So,

$$V_i = V_0 \left(1 + \frac{h_0\sigma_0}{|S|}\right) \tag{1.50}$$

By adding non-linear friction, they determined the expression of the initial velocity of dewetting $V_i(\sigma_0)$:

$$V_i = V_{0\alpha} \left(1 + \frac{h_0\sigma_0}{|S|}\right)^{\frac{2}{2-\alpha}} \tag{1.51}$$

Here, σ_0 represents the residual stresses acting in (positive) short times compared to the relaxation time τ_1, V_i is the initial velocity of dewetting in the absence of residual stresses, h_0 is the initial film thickness and α is an exponent that characterizes the non-linearity of the friction ($\alpha \leq 1$). For times shorter than τ_0, viscoelastic liquid dewets like a simple liquid with velocities V_0 (linear friction) and $V_{0\alpha}$ (non linear friction). Between times τ_0 and τ_1, the decrease in the dewetting velocity occurs by:

$$V(t) = V_i(t/\tau_1)^{-\frac{1}{2-\alpha}} \tag{1.52}$$

This expression actually corresponds to the maximum in rim width (Δ_m) ,

$$\triangle_m \approx \triangle_{0\alpha}\left(1+\frac{h_0\sigma_0}{|S|}\right) \tag{1.53}$$

because the relaxation of residual stress around the time τ_1 led to a decrease in dewetting velocity to the dewetting velocity $V_{0\alpha}$, and a decrease in width of the rim to the width $\Delta_{0\alpha}$ corresponding to the "equilibrated" value (simple viscous liquid).

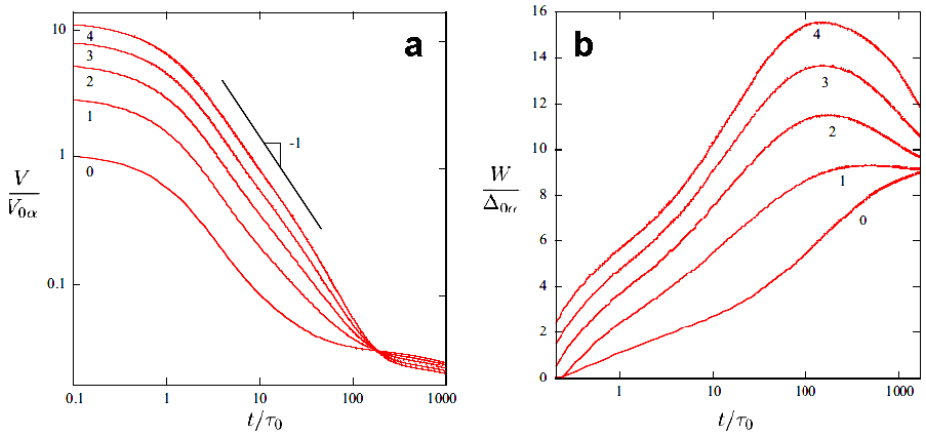

Figure 1.26 – Numerical calculations of the (a) reduced dewetting velocities $V/V_{0\alpha}$ and (b) reduced rim width $W/\Delta_{0\alpha}$ versus the reduced time t/τ_0 for a viscoelastic film ($\tau_1 = 100\tau_0$, $h_0E/S = 5$,) with the residual stresses $\sigma_0/E = 0$, 0.2, 0.4, 0.6, and 0.8, dewetting on a substrate with the friction exponents $\alpha = 2/3$. Adapted from ref. [102].

These theoretical predictions are in perfect agreement with experimental results (cf. **Figure 1.26 a-b**). **Figure 1.26 b** shows that the width of the rim increases to its maximum value of W_{max} ($\sim\Delta_m$) and then decreases. The maximum of the rim width increases with the residual stresses without affecting the relaxation time τ_1, which was confirmed during ageing of the films below the T_g of PS [42]. In summary, theoretical and numerical treatments by Vilmin *et al.* considered the non-linearity in friction between substrate and the film along with the initial presence of residual stresses which slowly relax during the course of dewetting, using the qualitative scaling arguments [102]. Considering the residual stress driven temporal evolution of dewetting Ziebert *et al.* explored the process in detail [105].

1.5 Deformation and failures in glassy polymers

For an ideal linear elastic medium, the material recovers fully from a deformation under a constant stress, if the stress (load) is removed. For many polymers these conditions are approximately satisfied for low stresses, but a very different type of behaviour may be observed for some polymers under suitable conditions. For stresses above a certain level, the polymer yields. After yielding the polymer either fractures (a local separation of an object or material creating new surfaces) or retains a permanent deformation on removal of the stress. Polymers do not always fail mechanically by yielding, *i.e*, by becoming ductile. Fracture without yield is called brittle fracture. Ductile fracture needs sufficient mobility in polymer chain segments, *e.g.* multiple crazing, shear yielding (plastic flow without crazing). Unlike the case of ductile fracture; in brittle fracture no apparent plastic deformation takes place before fracture. Depending on the environmental condition brittle soloids can exhibit time-delayed fracture.

Application of linear elastic fracture mechanics is only valid for materials that are perfectly elastic for small linear strains, often expressed by Griffith's treatment. Applying Griffith's idea to polymeric solids may look questionable at first, as these are neither ideally elastic nor linear in the response at strains near to failure [117]. To establish Griffith's criterion for fracture, plate geometry as shown in **Figure1.27** can be considered, which contains a crack of length $2c$. The plate has a thickness d, a Young's modulus E, and its surface area is assumed to be infinite.

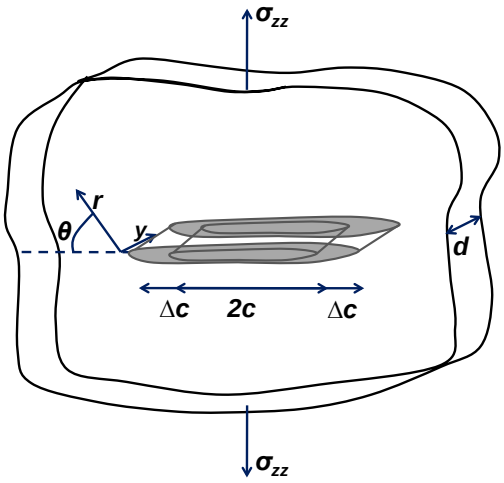

Figure 1.27 – Standard configuration (opening mode-I) considered in linear fracture mechanics: Infinite plate containing a crack of length $2c$ subject to a tensile stress σ_{zz}. Adapted from ref. [117].

If a tensile force is applied perpendicular to the crack direction, one finds a uniform uniaxial stress far from the crack, denoted as σ_{zz}. It is possible to calculate the drop of the elastic free energy (ΔF) of the plate, which results if the length of the crack is increased by $2\Delta c$. The solution of the problem is given by the expression

$$\Delta F = \pi c \sigma_{zz}^2 d 2\Delta c / E \tag{1.54}$$

The increase of the crack length produces additional surfaces on both sides and this requires a work ΔW, which is proportional to their area

$$\Delta W = 2\gamma d 2\Delta c \tag{1.55}$$

This equation includes γ as proportionality constant. Treating perfectly brittle solids, Griffith identified γ with the surface energy. For polymers, the meaning of γ has to be modified. As will be discussed, other contributions appear and even take control. The condition for fracture follows from a comparison of the two quantities ΔF and ΔW. A crack grows if the strain energy release rate G exceeds a critical value G

$$G = \Delta F / d 2\Delta c = \pi c \sigma_{zz}^2 E \tag{1.56}$$

It is the work needed to create the new surface. This is the case for

$$G \geq 2\gamma = G_c \tag{1.57}$$

The crack will be stationary for applied strain energy values below G_c ($G < G_c$) and propagates at higher values ($G \geq G_c$). G_c is also known as the fracture toughness or energy required to create a unit of fractured surface area.

Equation 1.57 is known as Griffith's fracture criterion. It includes a critical value of the strain energy release rate, G_c, (also denoted as G_{Ic} , the subscript 'I' is used to indicate reference to the crack opening mode-I of **Figure 1.27**). For a simple completely elastic, purely brittle fracture process (Griffith process), critical fracture energy will occur when the strain energy release rate is comparable to the surface energy of the two surfaces created; $G_c = 2\gamma$. For most of the polymeric materials, this would result in critical fracture energy of ~ 0.08 J/m^2, which is significantly lower than what is commonly observed. This indicates that there are additional contributions to the total fracture energy that need to be accounted for. So, some other processes must be involved in fracture. These

processes are in fact various localized yielding processes, the most important of which is the formation of a craze at the crack tip.

From **Equations 1.56** and **1.57** the critical value of the tensile stress follows as

$$\sigma_{zz,c} = (2E\gamma/\pi c)^{1/2} \tag{1.58}$$

$\sigma_{zz,c}$ sets the stability limit for the crack. For tensile stresses below that limit, the crack just opens maintaining a constant length of $2c$. If the tensile load exceeds $\sigma_{zz,c}$ the crack starts growing, until it has crossed the sample cross-section, *i.e.*, until it has completed the fracture.

Mechanical responses for amorphous glassy polymers under large stress can be represented in terms of true stress–strain curves. Let us first consider the behaviour shown in **Figure 1.28 a**. At small strains, the material responds purely elastically (linearly), so the initial part of the stress-strain plot is linear. For higher stress value, a slight departure from linearity is observed, which is more pronounced with increasing stress level. Further on, the true stress reaches a maximum, denoted as σ_y, corresponding to the yield point. At this stress value, the specimen no longer goes back to zero strain, permanent deformation remains. Straining the specimen beyond ϵ_y, a decrease of true stress is observed; this is the

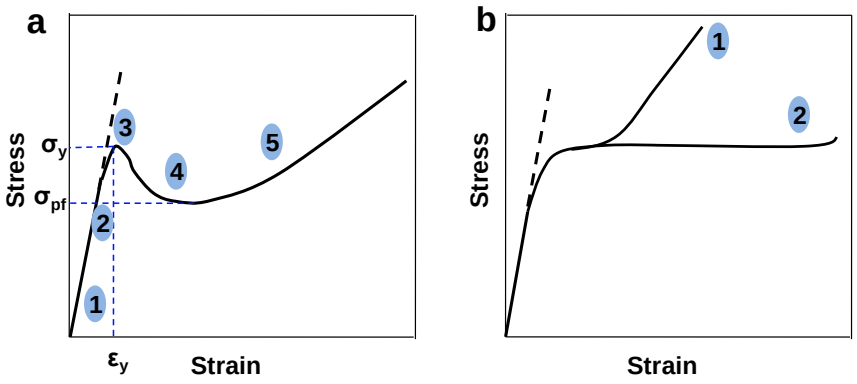

Figure 1.28 – Typical stress–strain curves for amorphous polymers. (a) Elastic, strain softening, plastic flow and strain-hardening regions can be seen. (a) 1-Reversible elastic and linear viscoelastic region at low stress. (a) 2-Non-linear elastic to viscoelastic transition at moderate stress. (a) 3-Yield region at high stress. (a) 4-Strain softening at moderate strains. (a) 5-Strain hardening at large strains. (b) 1-Strain hardening occurs very close to yielding, suppressing both strain softening and plastic flow behavior. (b) 2-Plastic flow occurs at the same stress level as required for yielding so strain softening does not exist. Figure inspired by ref. [20].

strain softening behaviour. This region of negative slope is associated with mechanical instability and is often associated with localization of strain. Once the

maximum is passed the material begins to flow at a constant stress. At a certain level, denoted as σ_{pf}, the true stress stabilizes and a plateau is obtained. It corresponds to the plastic flow behaviour, associated with an increase of strain under a constant stress, the plastic flow stress, σ_{pf}. At higher strain, a new increase of stress occurs, the strain hardening behaviour, which ends up with specimen fracture. Depending on the material and deformation conditions (strain rate, temperature etc.) other stress–strain curve shapes can be observed (cf. **Figure 1.28 b**). Depending on the polymer chemical structure, entanglement density, molecular weight, and on the deformation conditions, two types of deformations are possible: crazes and shear deformation zones.

1.5.1 Basics of the crazing process in polymers

Crazing can be considered as the localized process of yielding in polymers. Even by human eye crazes can be visible, such as craze whitening when a polymer bar/fiber is stretched. A craze consists of arrays of nanosized fibrils separated by voids that bridge the two surface of un-crazed polymer. Thus unlike a crack, a craze is still load-bearing, keeping the mechanical integrity (cf. **Figure 1.29**). Fundamental mechanisms for the craze development process and craze failure (leading to cracking) can be divided into following steps: craze initiation, craze growth and break down of craze fibrils leading to cracks (in case of considerably high strains) [118, 119].

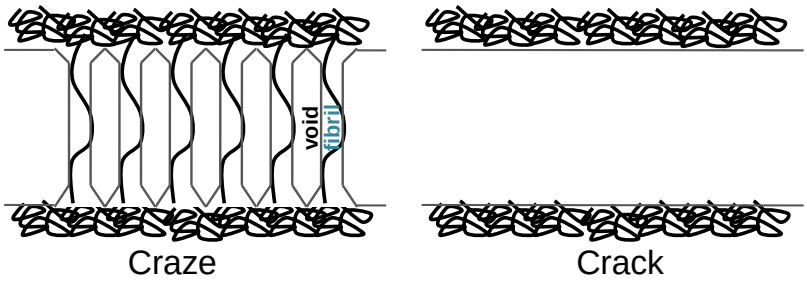

Figure 1.29 – Schematic representing crazes containing connecting polymer fibrils and cracks.

Craze Initiation:

Craze initiation is probably the least well understood part of crazing. Most of the studies considered it as a heterogeneous nucleation process [120]. Kramer viewed craze nucleation involving three types of processes: (i) local plastic deformation in the vicinity of a flaw (defects/edges of inclusion), leading to the build-up of a significant stress concentration. Specifically, yielding is initiated at the sites of

stress concentration. Further deformation of the material gets localized in this yielded region due to the strain-softening of glassy polymers. Locally a triaxial stress state is developed. (ii) This triaxial constraint is further released by the nucleation of voids within the locally yielded region. (iii) After void initiation, the voids grow in length, and the nucleus of the craze forms. Molecular orientation proceeds by strain-hardening of the intervening polymer. In this way the incipient craze nucleus structure get stabilized and can thereafter propagate if an appropriate stress condition is present.

Craze Growth:

After a craze nucleus forms, the craze grows in length (advancing) and width (widening) with the increase in stress or strain [118]. A more recent study revealed craze growth is also occurring in depth, known as micronecking, up to an equilibrium value [121]. The mostly accepted views on advancing and widening of crazes are the mechanisms of meniscus instability and surface drawing respectively [118]. For craze advancing, a craze-tip (pre-craze) forms ahead of fibrillated crazed region of a premature craze. This craze tip propagates by breaking up into a series of fingers running through the thickness of the film. For craze widening, fibrils grow in length by drawing new polymer chains from un-crazed region into fibrils.

Polymer chains staying within craze fibrils are in an extended state with a certain craze extension ratio, λ. For a given polymer, drawn under a given temperature and strain rate, λ is a constant along the vast majority of the craze length and only high just behind the craze tip [118]. λ is an important property of a craze and is the ratio of the width of the material that went into forming the deformation to the width of the deformed region after application of strain. A craze extension ratio can be defined as the ratio of the distance between two entanglement points for ideal Gaussian chains before (R, end to end distance) and after (l_e) an applied strain (cf. **Figure 1.30**). λ is related to the density of

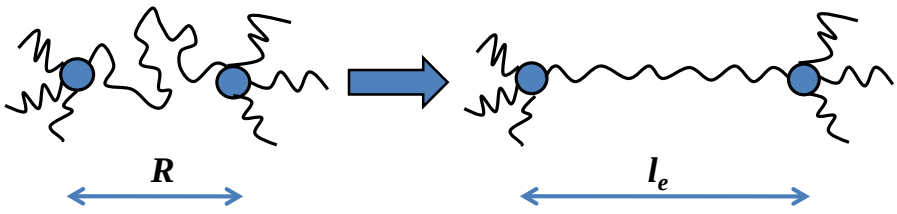

Figure 1.30 – Diagram of the Gaussian chain between two entanglement points before (R) and after (l_e) an applied strain. Reproduced from ref. [53].

chain entanglements (ν_e) as

$$\lambda \sim l_e/R \sim M_e/M^{1/2} \sim M_e^{1/2} \tag{1.59}$$

To separate two craze-bulk interfaces, a normal tensile stress, called the surface drawing stress or crazing stress (S_c), is applied on the craze-bulk interfaces. Kramer *et al.* have shown that craze stress (S_c) is crucially dependent on the total craze surface energy (Γ), yield stress (σ_y) and strain rate ($\dot{\epsilon}$) as

$$S_c = \sqrt{\Gamma(\gamma, \nu_e, U)\sigma_y(T)}.(\dot{\epsilon})^{1/2m} \tag{1.60}$$

The crazing stress is crucially dependent upon Γ as new void surface is created during craze widening [118]. Kramer *et al.* have also shown that the craze microstructures (void or fibril diameter D) is directly related to the surface energy and crazing stress as: $D \sim \Gamma/S_c$ [118]. Γ depends on the van der Waals surface energy (γ), the primary bond breaking energy (U), and the density of entanglements ($\nu_e \sim 1/M_e$), M_e is entanglement molecular weight).

The mechanism of fibrillation during craze widening is believed to proceed through both scission and disentanglement. If scission is operative, the stress for craze growth depends on the entanglement density via Γ. Disentanglement dependent crazing should have a molecular weight dependence of the crazing stress, since it can be anticipated that shorter chain will disentangle more easily. The process would be more favorable closer to T_g. Some thought must be given to how the chains can move at all in the glassy state, since naively the glassy state is thought to be a state in which long range motions of polymer chains are frozen out. However, the presence of external stress in itself provides a mechanism on the mobility of the chains, known as forced reptation [122]. There is currently no direct experimental evidence that shows if craze fibrils in bulk, high molecular weight polymers fail by processes of disentanglement. In case of thin polymer films, since the base of the fibril where the drawing is occurring, is of course a free surface, an additional drive for the disentanglement dependent crazing should be more probable, due to the enhanced surface mobility [13, 123].

Breakdown of craze fibrils:

High crazing stress at the craze-bulk interface contributes to the higher probability of fibril breakdown. Yang *et al.* found that high strain rate results in early fibril breakdown and material failure [124]. They found that fibril breakdown always occurs at the craze-bulk interface during widening of the craze. After fib-

ril breakdown, voids form within the craze and crack propagation subsequently initiates. Therefore, increasing fibril stability can lead to the increase in failure strain of materials. Beyond molecular considerations, also flaws like dust particles or scratches within materials can facilitate fibril breakdown.

1.5.2 Fracture toughness and craze-crack transition

Fracture processes in polymers demand a unified understanding at the molecular level correlating cracks and crazes propagation with the fracture toughness. Brown proposed the molecular interpretations for the failure of glassy polymers in the crazing regime [125]. He considered the geometry of a pure shear fracture mechanics specimen. The craze was considered as an anisotropically elastic sheet held between two rigid polymer boundaries (cf. **Figure 1.31**). The craze is assumed to have much lower elastic modulus than the surrounding uncrazed materials. A crack is supposed to advance within this strip. In this specimen geometry the local crack-tip driving force is a function of the sample width (w). The dominant contribution to the fracture energy is the work needed to craze the material in the process zone ahead of the crack tip [15]. As the crack advances, each region is expanded at the constant craze stress, S_c. In steady state, advancing the crack over an area has the net effect of expanding a region of this area at constant stress from its initial width to the final width w, at which the craze cracks. Hence, a criterion of breakage force per polymer chain can be related to the sample width or maximum craze width (w) and the material toughness (G_c) as

$$G_c = S_c w_0 \tag{1.61}$$

Here the movement of the craze-bulk interface w_0, corresponds to the crack opening displacement like $w_0 = w(1 - 1/\lambda)$; where λ is the craze extension ratio and S_c the craze stress. Thus,

$$G_c = S_c(w - w/\lambda) \tag{1.62}$$

Rottler and Robbins considered the identical specimen geometry like Brown, where G_c is primarily limited by the craze width w and the stress at the crack tip, *i.e.* the maximum stress $S_c(\max)$ that the craze fibril can withstand (cf. **Figure 1.31**) [126, 127]. The crazing stress diverges as the crack tip is approached. This divergence is cut-off at the characteristic fibril spacing D_0, below which the material can no longer be treated as a homogeneous elastic medium. They represented the ratio of crazing stress in terms of craze width and

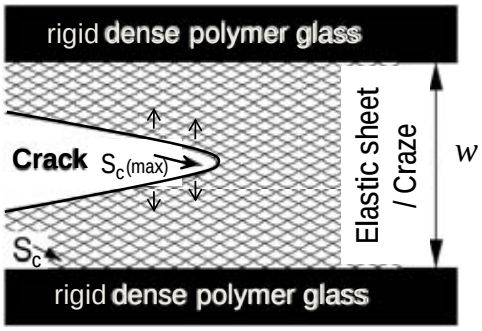

Figure 1.31 – Diagram of the geometry of a craze at the crack. The elastic sheet of width w is held between rigid boundaries of dense polymer glass. Redrawn after ref. [126].

fibril spacing as

$$S_c(max)/S_c \sim (w/D_0)^{1/2} \tag{1.63}$$

Their calculation of $S_c(\max)/S_c$ revealed several interesting observations relating chain length and fracture toughness of polymers. Short chains of length $M_w/M_e \leq 2$ can easily disentangle rapidly and the stress drops monotonically. Fracture energy rises rapidly as M_w/M_e rises above 2 and then saturates above M_w/M_e around 8-10 [126]. Interestingly, their simulation results agreed with several experimental observations in greater detail. Sha *et al.* have compiled values of G_c for PS and PMMA as a function of polymer molecular weight [128]. Neither polymer showed large fracture energy when molecular weight was less than $2M_e$. Previously Kramer showed that long craze fibrils are not stable below a critical molecular weight $M_c \sim 2M_e$, after that, a steep increase in G_c value was experimentally observed. From the above discussions it is clear that length of a polymer chain and entanglement has a deterministic role on the craze fibril stability.

Chapter 2

Experimental Techniques

This chapter deals with the materials and methods applied for the preparation of samples for all the experiments. Instrumental techniques used for all the experiments are also explained with respect to the basic working principles and the importance in the particular experiments.

2.1 Materials and methods

2.1.1 Polystyrene

We are interested in the property of polystyrene (as a model flexible polymer) in ultrathin films. Polystyrene (abbreviated as PS) is a polymer made from the aromatic monomer styrene, a phenyl containing aromatic hydrocarbon. Polymers are made of chains consisting of many monomer units. Polystyrene is made (usually) by radical polymerization, from the monomer styrene (**Figure 2.1 a**). The isomer where all the phenyl rings are on the same side of the backbone is called isotactic polystyrene (**Figure 2.1 b**). Ordinary atactic polystyrene has the phenyl groups randomly distributed on both sides of the chain. This random positioning prevents the chains from aligning with sufficient regularity and thus avoids any crystallinity. Atactic polystyrene is glassy at room temperature. The glass transition temperature for bulk PS is about 105 °C. The surface tension is approximately 40 mN/m at 20-25 °C. Other important parameters are density = 1.05 g/cm^3 and refractive index = 1.59 at ambient temperature. Kuhn statistical segment has a value of b = 0.68 nm and a monomer molecular weight of 104

g/mol [129]. Utilizing above parameters in the common statistical relations for polymers, we can calculate several other physical parameters for polystyrene close to experimental values.

One can interpret the plateau modulus as rubber type elasticity in which instead of having permanent cross-links we have temporary entanglements. The distance along the chain between entanglements can be estimated inspired from the rubber elasticity formula for the shear modulus

$$G = \rho R_k T / M_e \tag{2.1}$$

where ρ is the density of the polymer, R_k is the gas constant and M_e is interpreted as the molecular weight between entanglement points (for rubber this is the average molecular weight between permanent crosslinks M_c). The entanglements are not permanent, but have a finite lifetime, which is the terminal time (τ_t). The zero shear viscosity be related to the modulus like $\eta_0 \sim G\tau_t$. From the value of b and using the random-walk model, the root mean squared distance in space (R_{RMS}) between entanglements in polystyrene can be estimate to be $b\sqrt{N}$which is ca. 8.5 nm for polystyrene, where N is the degree of polymerization, obtained by dividing the relative molecular mass of the polymer M_e by that of the monomer unit. M_c is a material constant for a given polymer; it is about twice the value of M_e for the same polymer. For polystyrene M_c is in between 35-36 kg/mol. So, M_e is ca. 17.5-18 kg/mol [8,129]. Polystyrene samples used in this study were ob-

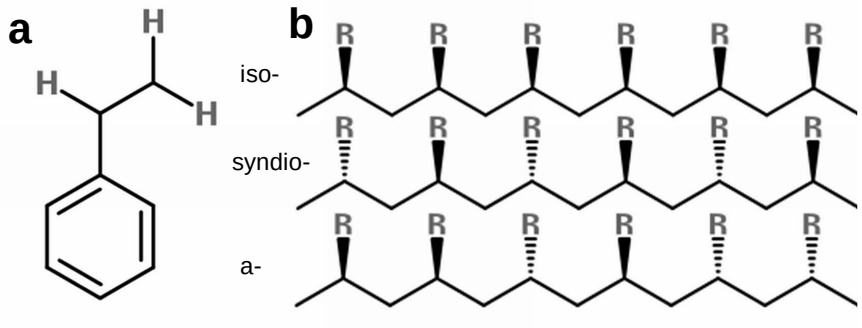

Figure 2.1 – (a) Chemical formula of styrene monomer. (b) Tacticity: the relative stereochemistry of adjacent chiral centers within a macromolecule. In case of PS, R = Phenyl group. From top to bottom: Isotactic, Syndiotactic and Atactic

tained from PSS (Polymer Standards Service GmbH, D-55120 Mainz, Germany). Their molecular weights and polydispersity indices are shown in table 2.1

M_w(kg/mol)	M_n(kg/mol)	PDI = M_w/M_n
52	48	1.08
125	120	1.04
532	497	1.07
1070	1010	1.06
4060	3510	1.15
16800	12600	1.33

Table 2.1 – Polystyrene (PS) samples used in this study with molecular weight (M_w) and polydispersity index (PDI)

2.1.2 Polydimethylsiloxane

Polydimethylsiloxane (PDMS) belongs to a group of polymeric organosilicon compounds that are commonly referred to as silicones. PDMS is the most widely used silicon based organic polymer, and is particularly known for its rheological properties. For our purpose of dewetting a PS thin layer, we prepared PDMS coated silicon wafers, where PDMS acts as a non-wettable liquid underlayer enabling slippage and serve as a reproducible substrate. Dewetting dynamics is partially determined by the dissipation of the capillary energy due to the friction at the PS-PDMS interface [99]. PDMS are formed of a siloxane (Si-O-Si) backbone with attached methyl groups (cf. **Figure 2.2**). This gives rise to an apolar and hydrophobic character. The glass transition temperature (T_g) is -125 °C. Surface tension γ is ca. 21 mN/m and refractive index = 1.46 at ambient temperature [129]. We mainly used 139 kg/mol silanol terminated PDMS (DMS-S51, 0.02% -OH, viscosity = 75000-115000 cSt.). In a particular case, 77 kg/mol silanol terminated PDMS (DMS-S21, 0.8-0.9% -OH, viscosity = 90-120 cSt.) was also used in this work. Both PDMS were obtained from ABCR, D76189, Karlsruhe, Germany.

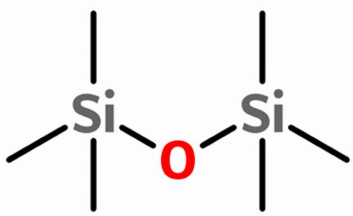

Figure 2.2 – Chemical formula of two dimethylsiloxane units.

2.1.3 Preparation of the non-wettable layer on Si/SiO_2 wafer

Activation (hydroxylation) of Si/SiO_2wafer: In silicon crystals the atoms are sp^3 hybridized and bonded to four nearest neighbours in tetrahedral coordination. When the crystal is cut or cleaved, bonds are broken, creating dangling bonds at the surface [130]. Dangling bonds are the source of chemical activity of silicon surfaces. The interaction of silicon surfaces with atmospheric oxygen gas can lead to production of a native oxide layer of about 2-3 nm on the surface (passive oxidation): $Si(s) + O_2 \rightarrow SiO_2(s)$. For our experiments we used Si (100) wafers (supplier: Silchem Handelsgesellschaft mbH, D-09599, Freiberg, Germany). It needs a pre-cleaning and activation before preparing a monolayer of PDMS on $Si/SiO_2(100)$ surface through chemical and physical adsorption. The high energy UV photons interact and break the hydrocarbon bonds of any possible organic contaminant. Hydroxylation proceeds through oxidation of $Si/SiO_2(100)$ surface (in presence humid environment) finally leading to the formation of dangling Si-OH.

For our experiment, we used a standard procedure, by keeping the Si/SiO_2 (100) wafer under UV-radiation (UVP, Pen Ray®) for 60 minutes in a moistened environment containing some liquid water, putting the whole set-up in a closed container. The UV-lamp was a low pressure mercury lamp, having the main spectral peak at 254 nm ($h\nu = 4.89$ eV). A secondary peak at 185 nm ($h\nu = 6.71$ eV) is typically used for generating ozone (it actually dissociates O_2, which causes the atomic O to attach to surrounding O_2 producing O_3) [131]. 254 nm UV light can dissociate the ozone by breaking it up. However, the ozone creation occurs at a faster rate and the net result is a propagation of ozone in air. Fink *et al.* explored the oxidation of $Si/SiO_2(100)$ and found it proceeds through different oxidation stages at the $Si/SiO_2(100)$ surface and interface (cf. **Figure 2.3**) [132].

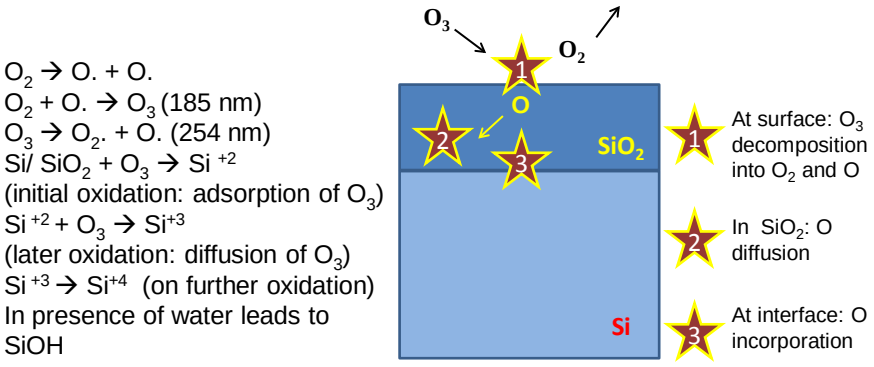

Figure 2.3 – Schematic representation showing Si/SiO_2 surface oxidation by O_3 . Redrawn from ref. [132].

There are several types of hydroxyl groups can be on the $Si/SiO_2(100)$ surface. The most common are isolated, freely vibrating SiOH groups (free hydroxyl groups), isolated pairs of SiOH groups bonded to each other (vicinal), and adjacent pairs of SiOH groups with hydrogens bonded to each other [133]. We need the hydroxylated Si-surface for further adsorption of PDMS through preferential hydrogen bonding between surface silanol (–OH) and siloxane (–O). There is always the chance that water molecules reach the surface and bind through H-bonding, creating a thin layer of water at the surface making it hydrophilic. However, oxidized surfaces can also be hydrophobic to a certain degree when the Si-O bonds wrap back upon the surface, closing the bond. This closed bond is a Si-O-Si, or siloxane bond. However, this siloxane bond formation is not feasible at room temperature. UV light is known to modify the SiOH surface by dehydroxylation of the surface. So, prolonged UV activation may not be useful for our purpose [134].

Adsorption of PDMS on activated Si-wafer: In our method, we spin-coated a 1% solution of PDMS (silanol terminated) in heptane (good solvent for PDMS) to cover up the hydroxylated Si-wafer. To ensure the PDMS adsorption, the wafer was kept at a temperature of 160 °C for 6 hours. During such incubation, the PDMS molecules were adsorbed progressively more and more strongly by gradually bringing more segments per chain to the substrate where these segments could form hydrogen bonds with the hydroxyl groups of the substrate. This reaction finally leads to irreversible adsorption of the chains. The surfaces were then washed in a heptane bath for 1 hour to eliminate all the unadsorbed PDMS chains. Heptane being volatile at room temperature easily dried up from the PDMS adsorbed Si-wafer. Ellipsometric measurements showed that the dry thickness of the PDMS monolayer (M_w= 139 kg/mol) is about 14-15 nm. Interestingly, this dry thickness value is considerably higher than the calculated redius of gyration, indicating stretched chains.

PDMS forms hydrogen bonds between the silanol sites of the silica surface and the oxygen atoms of the backbone of the chains, and thus spontaneously adsorbs on an activated silica surface. This adsorption is quasi-permanent, and can be permanent by using di-hydroxyl terminated PDMS chains. So, the end groups of PDMS chains play an important role in the adsorption as hydroxyl-terminated chains are absorbed in greater amount [135]. An investigation on the interactions between PDMS and silicon dioxide using electronic structure calculations and molecular dynamics simulations, however, has challenged the conventional view that oxygen atoms in the PDMS backbones form hydrogen

bonds with silanol groups on silica surfaces [136]. This study shows that the PDMS end groups dominate the interactions between PDMS and the silica surface due to the steric hindrance caused by methyl groups on the PDMS backbone.

The process of adsorption involves both of the physical and chemical way. Physisorption takes place due to the H-bonding between siloxane -O with the silanol group of activated Si-wafer. The case of chemisorption comes when end terminal –OH groups of a hydroxylated PDMS bonded with silanol sites in the surface. To test the modified Si/SiO_2 surfaces separate contact angles of water were investigated on the treated surface of silicon wafers by Gabriele [137]. Highest contact angle was found for the adsorbed PDMS layer indicative of its non-wettability (cf. **Figure 2.4**). A UV-cleaned Si/SiO_2 surface was found to be more wettable than the untreated one.

Figure 2.4 – Different situations of a drop of water on (a) a non-treated/cleaned Si-wafer, (b) a Si-wafer cleaned under UV light and (c) a Si-wafer cleaned and covered with a 5 nm thick adsorbed PDMS layer. Taken from the thesis of Gabriele [137].

Theoretical ideas on irreversibly adsorbed polymer brush: When a strongly attractive surface is exposed to a polymer melt, a certain amount of polymer becomes permanently bound to the surface. That means, when the plane solid surface is put in contact with a polymer melt, all the monomers touching the surface adsorb instantaneously and irreversibly; assuming that the time necessary to saturate all the surface sites is small in comparison to the time of chain diffusion in the bulk. Conformation of the chains is thus not modified during the adsorption process and the distribution of loops and tails is related to the chain statistics in the melt. If the polymer layer is then exposed to a good solvent, only the initially adsorbed chains are retained on the surface and the layer swells. The resulting layer is made of loops and tails, with a large polydispersity of loop sizes as a succession of loops and tails. The structure of such irreversibly adsorbed layers has been described by Guiselin [138]. Theoretical scaling laws validated by experiments give expressions of surface chain densities (Σ) as well as pseudo brush dry thicknesses (h) in good solvent conditions as

$$h \cong aN\Sigma \cong aN^{1/2}\phi^{1/2} \tag{2.2}$$

where N is the number of monomers per polymeric chain, ϕ is the volume fraction of polymer in the solvent and a is the monomer size (ca. 0.5 nm for PDMS) [139]. This relation essentially points out the role of molecular weight (chain length) on thickness. Although this relationship is a simple scaling law, it can be roughly correleated to our measured dry thickness of ca. 15 nm (by calculation: considering $\phi = 1$ for the melt, thickness becomes ca. 21 nm). Incubation condition essentially modifies the film thickness. Using the same PDMS solution, changing the incubation temperature to 200 °C, leads to a dry thickness of ca. 40 nm. Probably, this thickness increase is due to an increase in the number of chemically end-grafted PDMS chains per unit area as well as indicates large stretching of polymer chains inside the irreversibly adsorbed polymer brush.

Hamieh *et al.* described a series of experiments by preparing varying thickness of PDMS layers (by varying molecular weight and incubation temperature) to illuminate the influence of the energy-dissipation mechanism at the interface between the PDMS coated silicon wafer and the PS film on the dewetting process [99]. The initial opening velocity of holes was found to increase with the thickness of the PDMS layer. The maximum width of the dewetting rim increased significantly with PDMS layer thickness, indicating an increase of an effective velocity-dependent slippage length (b_s).

2.1.4 Preparation of polystyrene thin films by spin-coating

Spin-coating is a method for preparing a thin film of uniform thickness on a substrate. In our case, it involves the preparation of a thin PS film from a dilute PS solution over the non-wettable Si-wafer. The spin-coating process has been conceptually divided into four steps: deposition, spin-up, spin-off and evaporation [140]. First step involves deposition of polymer solution on a flat smooth rotatable substrate. ”Spin-up” is the acceleration of the substrate from its initial rotational speed to its final rotational ”spin-off” speed. During spin-up the liquid spreads out to cover the substrate. At the end of spin-up, the substrate is covered by liquid, but the thickness is not uniform. During “spin-off” some liquid can flows off of the edges of the substrate. The remaining liquid layer becomes uniformly flat, rapid solvent evaporation starts and the entire layer thins, and solidifies. After solidification the film thins by further solvent evaporation. However, it is hard to differentiate between “spin-off” and evaporation, as evaporation

can be started already from the spin-off stage. In case of polymers, spin-coating starts from equilibrium polymer chains in solution, passes the glass transition temperature and ultimately leads to a dry sample, where the chain conformations become "frozen-in" (vitrified). For PS in toluene vitrification takes place at 14-20% solvent content at room temperature that is long before the complete evaporation [141]. At the point of vitrification removal of remaining solvent has to rely on volume/density change inside the film (for thickness below $\sim 2R_g$ of PS) leading to stress generation, known as residual stress, which has been discussed elaborately in **Section 1.3.2**.

Ideally, the film thickness (h) depends only on the spin speed (ω) during spin-off and on the initial concentration (c) of the liquid [142],

$$h = K\eta^{\gamma}c^{\beta}/\omega^{\alpha} \tag{2.3}$$

where K is an overall calibration constant, η is the intrinsic viscosity. α, β, γ are exponents. These exponents can be determined experimentally. A simple account of the spin-coating process and the resulting thickness was given by Chakraborty *et al.,* where the film thickness (measured by the UV-Vis interferometric method and FTIR using the Lambert-Beer law of absorbance) as a function of the initial PS concentration showed a nearly linear relationship ($\beta = 1$) [142]. The film thickness can be estimated through the interference colour (apart from ellipsometry or X-ray reflectometry which give the thickness value more precisely). Details of these processes will be discussed in next sections of this chapter. The spin-coating device used in this study is a Convac® 1001 spin-coater that consists of a spin head fixer that uses vacuum pump suction to hold the substrate during the spinning process, and a digital controller. The spin coater is capable of spin speeds from 100 rpm to 6000 rpm. In general 3000 rpm spin speed was used for preparing thin films in this study (if not mentioned otherwise). An overall scheme for the film fabrication process is given in **Figure 2.5.**

2.1.5 Thermal treatments during ageing, cracking/crazing and dewetting

Thermal treatments are known to have impacts on molecular motions of polymers.

Ageing: Glassy materials are not in equilibrium. They undergo slow physical process towards the equilibrium, a process known as physical ageing. Generally, this ageing process is slow at temperatures well below T_g; therefore, most studies

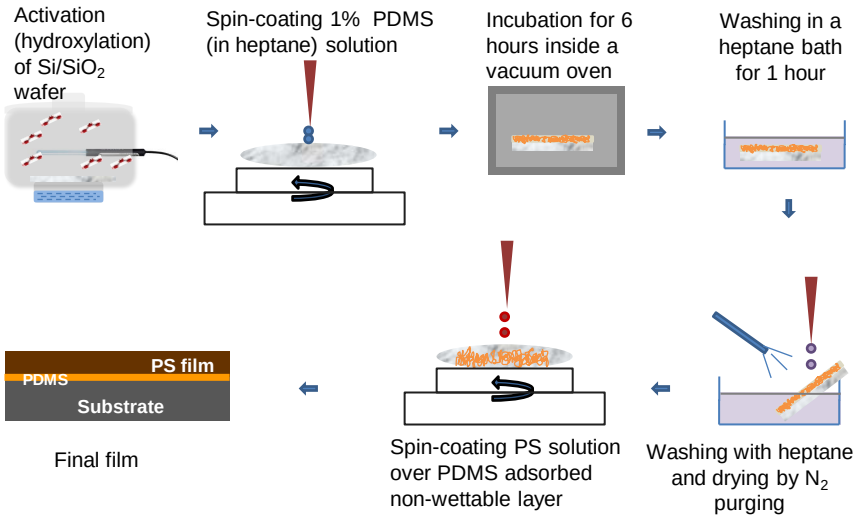

Figure 2.5 – Scheme representing all the steps associated with PS film preparation over non-wettable (PDMS adsorbed) Si-wafer.

of physical aging have been carried out at temperatures from room temperature upto close to T_g ($T_{g,bulk}$ of PS is ca. 105 °C), such as at 50 °C, 60 °C, 70 °C, 80 °C and 90 °C. Ageing was always performed inside a vacuum oven. Keeping in mind the sensitivity to temperature, the temperature inside the oven was calibrated through thermo-couple sensors.

Cracking/crazing: Cracking/crazing was found as a combined effect of physical ageing and thermal stress (due to the difference in thermal expansion coeffiecnts between PS film and the substrate). Crack/craze growth was found during cooling of films from the elevated ageing temperatures (such as 80 °C or 90 °C, close but below the $T_{g,\ bulk}$ of PS, down to room temperature). We found that the lower limit of ageing temperature for crazing (in long chain PS) is $T_a = T_{g,bulk} - (20 \pm 5)$ °C and for cracking (in short chain PS) is $T_a = T_{g,bulk} - (30 \pm 5)$ °C. Upon cooling of films which were aged at 90 °C, cracking generally started from (60 ± 5) °C whereas crazing for higher molecular weight PS films started from (40 ± 5) °C.

Dewetting: Dewetting is the process of retraction of a liquid on a non-wettable or poorly-wettable substrate. PS films on a non-wettable substrate have to be heated sufficiently above-T_g to see hole growth in terms of dewetting. Most of the dewetting studies discussed in this thesis were performed at 125 °C. In few cases, for reasons of comparison we also used temperatures from 130 °C to 160 °C. Mostly, dewetting dynamics was followed to judge the extent of residual stress inside a film [42]. For that reason dewetting was performed after ageing and crazing (if any) of the film. **Figure 2.6** schematically depicts a typical thermal treatments of a PS film. We used a Linkam®THMS 600 hotstage for dewetting,

equipped with a light microscope to follow the dewetted hole growth.

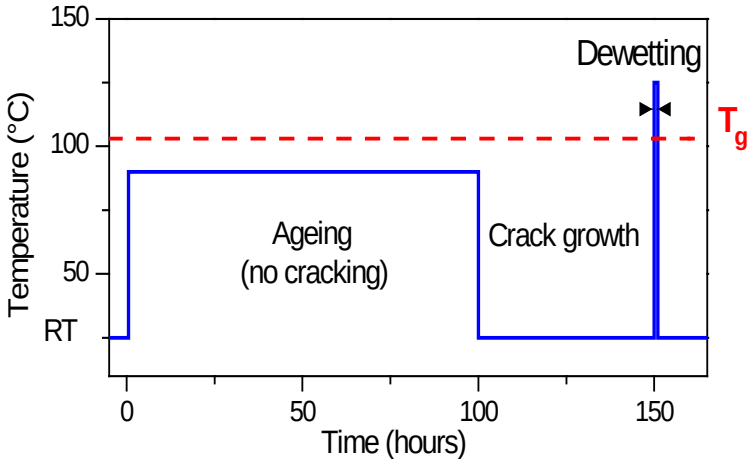

Figure 2.6 – Scheme of thermal treatments performed on a PS thin film during ageing, crazing/cracking and dewetting.

2.2 Optical microscopy

Optical microscope is the classical type of microscope which uses visible light and a system of lenses to magnify images of objects too small to be seen with the naked eye. In our study, we used Olympus BX-51M® upright microscope (equipped with UC 30® camera and objectives ranging from 5X to 100X) and Zeiss AxioScope A1® (equipped with AxioCam ICc.1® camera and objectives ranging from 10X to 100X)

2.2.1 Basic principles of optical microscopy

A typical compound microscope consists of a stand, a stage to hold the specimen, a movable body-tube containing the lens systems (a single light path, multiple lenses, each lens magnifies the image over the previous one), and mechanical controls for easy movement of the body and the specimen. The image produced is a two dimensional (2D) image. In digital microscope, a microscope and a video camera are integrated together with a digital output. There are two kinds of digital cameras, both of which convert light into electric charge and process it into electronic signals, namely CCD (Charge-Coupled Device) camera and CMOS (Complementary Metal Oxide Semiconductor) camera.

In microscopes, magnification is usually indicated by the abbreviation "X". So, a 100X objective will magnify the image by 100 times. Modern microscopes utilize infinity corrected optical systems with a tube lens of finite length. The magnification power of the objective lens is the focal lengths of the tube lens divided by the focal length of the objective. With a number of optical elements contributing to the overall image magnification, it is important to remember that the final image is not just magnified only by the objective. To magnify an object even more, two lenses in combination have to be used (objective and eyepiece). The magnification of a microscope (when viewed through the eyepiece) is thus a product of $M_{objective}$ x $M_{eyepiece}$. So, finally for digital imaging with video monitor it becomes, $M_{video\ monitor} = M_{objective}$ x $M_{video\ camera\ adapter}$ x *Monitor magnification* [143].

The power of resolution is given exclusively by the objective. Magnification is not the only parameter to consider for an objective. The numerical aperture ($N.A$) of a microscope objective is a measure of its ability to gather light (brightness) and resolve fine specimen detail (resolution) at a fixed object distance. $N.A$ can be expressed as

$$N.A = n \sin \alpha \tag{2.4}$$

The medium is usually air with a refractive index of $n = 1$. The numerical aperture hence never exceeds 1. The maximum actual value is 0.95, since the distance between objective and the surface of the cover glass or sample cannot reach zero. The aperture of 0.95 corresponds to $\alpha \approx 72°$. The visual field brightness (B) of the microscope is determined by the following formula in relation to the objective lens magnification (M) as

$$B \sim (N.A)^2/M^2 \tag{2.5}$$

Therefore brightness will increase as the $N.A$ increases and/or as the objective magnification decreases. Resolution is another important parameter describing the ability to separate two elements in the viewing field from each other. The degree of resolution (d) is dependent upon wavelength of light (λ) and the numerical aperture ($N.A$) as

$$d = \lambda/N.A \tag{2.6}$$

If we try to calculate the degree of resolution in air considering yellow light wavelength = 570 nm and $N.A$= 0.95, it becomes 0.6 µm.

2.2.2 Importance of interference on polymer thin films

Considering the wave-particle duality of light, some fundamental principles of wave optics can be applied in order to be able to interpret microscopic image formation. The wavelength of visible light is between 400 and 800 nm. Interference is the mutual influence of two waves on each other, whereby the resulting wave may be either enhanced or flattened (enhancement of amplitude: constructive interference or reduction of amplitude: destructive interference). Interference between light waves is the reason that thin films, such as soap bubbles or nanometer thick polymer films show colourful patterns. This is known as thin-film interference, because it is the interference of light waves reflecting off the top surface of a film with the waves reflecting from the bottom surface. To obtain a nice coloured pattern, the thickness of the film has to be similar to the wavelength of light [144].

When a thin polymer film was deposited on a solid silicon substrate, two interfaces were created: air/polymer and polymer/substrate. The incoming light ray (I) was reflected at the air/polymer interface generating the ray R_1. The refracted part of I was reflected at the second interface, polymer/silicon and transmitted as ray R_2 at the polymer/air interface (cf. **Figure 2.7 a**). The reflected rays (R_1 and R_2) interfered producing interference colours [145].

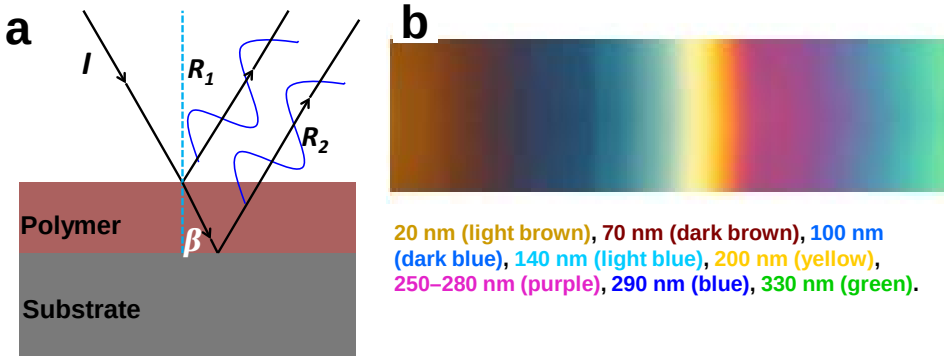

Figure 2.7 – (a) Schematic representation of the interference phenomenon in a thin polymer film deposited onto a silicon substrate (b) Interference colors from a polystyrene film on a silicon wafer. The film thickness changes from left to right (not on a linear scale): Taken from the thesis of Schäffer [146].

For a polymer film characterized by the thickness h and a refractive index n_{poly}, the optical pathlength difference will be given by

$$\delta = 2hn_{poly} \sin \beta \tag{2.7}$$

Here, β is the angle between the surface normal and the transmitted wave. When such a film is illuminated with monochromatic light with the wavelength λ, we can have constructive or destructive interference. The condition for constructive interference can be expressed as

$$\delta = (2k)\lambda/2 \tag{2.8}$$

The condition for destructive interference is obtained if

$$\delta = (2k+1)\lambda/2 \tag{2.9}$$

Here, k is an integer. For simplicity we considered a single polymer layer for the total film thickness; in our case, this thickness comprises of PS and PDMS.

By first calibrating the thickness-RGB colour (for a given system), one can determine film thickness with a resolution of a few percent. For sufficiently small total film thickness, (up to the first minimum in the interference intensity) a single channel can be used. Schäffer nicely documented PS film thickness over Si-wafer, where colors follow a periodic scheme with increasing film thickness, starting with a light brown (20 nm) up to green (330 nm) (cf. **Figure 2.7 b**) [146]. This interference phenomenon is limited by the coherence length of the light used (several microns for conventional light sources). Due to decoherence, the intensities of the various wavelengths become similar. More colors are mixed in and appear faded, eventually having the same intensity distribution as the incoming white light.

2.3 Atomic force microscopy (AFM)

In 1985 Binnig *et al.* developed the Atomic Force Microscope to measure ultra small forces (less than 1 µN) present between the AFM tip and the sample surface [147]. Binnig and Rohrer were awarded with the Nobel Prize in Physics in 1986. At present AFM is one of the most popular scanning probe technique used for characterizing nanoscale materials and surfaces. Tapping-mode atomic force microscopy was employed as one of the main analysis techniques in our study. In our study, we used the JPK BioMAT™ setup consisting of a NanoWizard® AFM, the BioMAT™ base and a Zeiss AxioImager optical microscope.

2.3.1 Basic principles of AFM

The information obtained by AFM is gathered by "feeling" the surface with a mechanical probe utlizing short-range interactions (mostly van der Waals interactions). AFM consists of a cantilever (**Figure 2.8 a**) with a sharp tip (**Figure 2.8 b**) at its end that is used to scan the sample surface. The cantilever is typically silicon or silicon nitride with a tip radius of curvature on the order of nanometers. The cantilever is fixed to a glass block, which is locked to the AFM during scanning. The important parameters of an AFM cantilever are the material, the spring constant and the resonance frequency. For our measurements, AFM cantilevers were made of silicon (type: PPP-NCL-W) provided from Nanosensors®. The silicon resistivity was about 0.01-0.02 Ω cm. The properties of the cantilevers used are given by thickness (7 ± 1 μm), length (225 ± 10 μm), width (38 ± 7.5 μm), height (10−15 μm), resonance frequency (146−236 kHz) and force constant (21−98 N/m). The cantilevers and tips were not coated. We used tapping mode imaging. When the tip is brought into proximity of a sample surface, forces be-

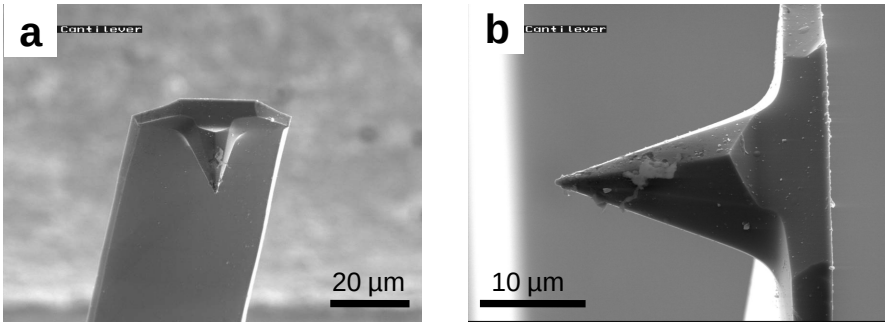

Figure 2.8 – (a) Electron micrographs showing (i) an AFM cantilever and (ii) a tip lying on the top of the cantilever. Taken from 'Wikipedia' and available under free content licence or GNU free documentation licence.

tween the tip and the sample lead to a deflection of the cantilever according to Hooke's law. As the tip of the cantilever is scanned across the sample its motion is detected by a laser beam that must be focused onto the cantilever. The angle of the reflected beam from the cantilever is detected by a four-segment photodiode. The reflected laser spot must be at the centre of the detector to give maximum sensitivity for imaging and force control (cf. **Figure 2.9**).

Besides other modes, AFM can be performed in two distinct imaging modes: contact and non-contact modes. In contact mode, the tip is in direct contact with the surface and the forces are the consequence of the short-range repulsive interactions between the tip and the surface. In non-contact mode, the tip scans over the surface at a distance, and the longer-ranged attractive van der

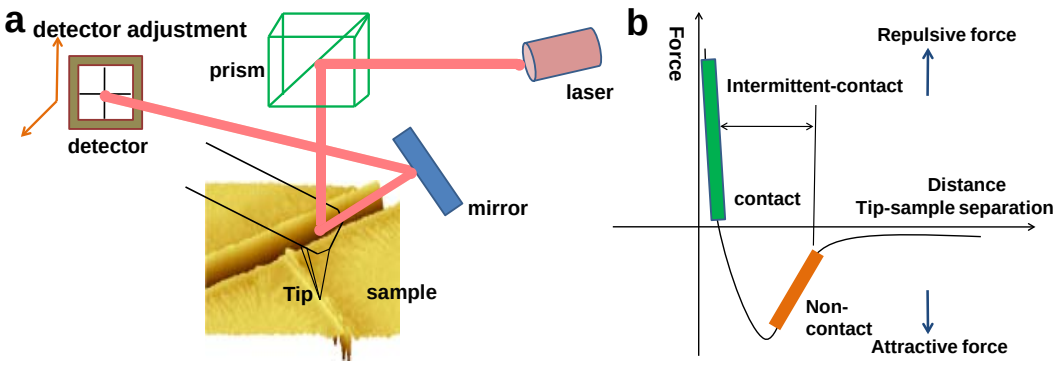

Figure 2.9 – (a) Schematic illustration of the basic optical path followed by the laser in JPK NanoWizard® AFM. (b) Interaction potential for contact, non-contact and tapping AFM imaging modes. For all the case a short-ranged repulsive and longer-ranged attractive force is operating. Redrawn after inspired from 'Wikipedia'.

Waals interactions are determined. The main drawback of contact mode is the friction force applied by the tip on the surface which can cause damage to soft morphological features on the surfaces of polymers. In case of non-contact mode, although it avoids the risk of damaging the probe, requires that the tip remains sufficiently far from the surface. This requires that the forces must have a small but quite nonetheless detectable on the cantilever which affects the amplitude of the measured signal and the resolution of images.

Tapping mode (intermittent contact mode) represents an imaging technique which corresponds to a controlled oscillation of the cantilever. By cantilever oscillation it is not possible to directly measure the force, but the difference in force which is experienced by the cantilever. The oscillation is imposed to the cantilever at its resonance frequency. When there is a difference in force, it is detected by the tip, and then the oscillation frequency is changed. By detecting and adjusting the change in the oscillation frequency (via the feedback loop), AFM can detect very small variations in forces. Tapping mode is a combined mode of contact and non-contact AFM. The oscillating cantilever is placed closer to the surface than in non-contact imaging mode which helps the tip to actually come into contact with the surface at every oscillation. This results in a shift in the oscillation frequency and amplitude, modified by the feedback loop. Thus, tapping mode has the resolution of contact mode AFM, but due to the very short period of effective contact between the tip and the surface, destructive lateral friction is reduced, preserving the advantages of non-contact mode imaging.

2.3.2 Imaging polymer surfaces by AFM

AFM is extremely useful for studying the local surface molecular composition and mechanical properties of a broad range of polymer materials, including self-assembled polymers, crystalline polymers and polymer blends [148–150]. Uses of AFM is not limited to the case of amorphous polymer surface without any significant morphology. Goldbeck-Wood *et al.* addressed the question of the structural organization at the surface of a typical amorphous polymer, atactic polystyrene (aPS), by means of direct structural investigation by high-resolution AFM accompanied by coarse-grained simulation approach [151]. They found a characteristic feature in the surface autocorrelation function, having a length scale close to the radius of gyration of the polymer. Deformation and stiffness on amorphous polymeric surface is often characterized through AFM [152]. Maganov *et al.* showed the importance of phase imaging of amorphous surface showing that it allows one to distinguish different surface features of both multicomponent materials and one-component systems with different density distributions [153].

Phase images recorded at moderate tapping are related to surface stiffness variations associated with Young's modulus change. In general, by mapping the phase of the cantilever oscillation during the tapping mode scan, phase imaging goes beyond simple topographical mapping to detect variations in composition, adhesion, friction, viscoelasticity, and perhaps other properties. Phase imaging results when there is a difference in phase between the imposed oscillation signal and the detected oscillation of the cantilever. This phase shift results from the dissipation of energy occurring during the tapping of the tip on the surface. Different materials will induce different energy dissipation, allowing their differentiation in an image, even on a topographically flat surface. Phase imaging is effective in the here studied polymer thin films in case of characterizing *e.g.* the stripe-pattern orthogonal to the craze direction (hinting at periodic 'stiffening', a localized deformation, cf. **Figure 2.10**). Detailed studies concerning craze microstructures will be presented on **Chapter 5**.

In our case, tapping-mode AFM was very useful in order to get a three-dimensional surface profile for the crazes which were helpful in order to measure the width and depth of the crazes along with the sizes of fibrils/voids. Additionally, samples imaged by AFM in our studies did not require any special treatments. Scanning in a direction parallel to a craze line could clearly show fibrillar craze nano/mcrostructures inside it (cf. **Figure 2.11**). The scanning direction is important for scanning the junction of two perpendicular crazed lines. This

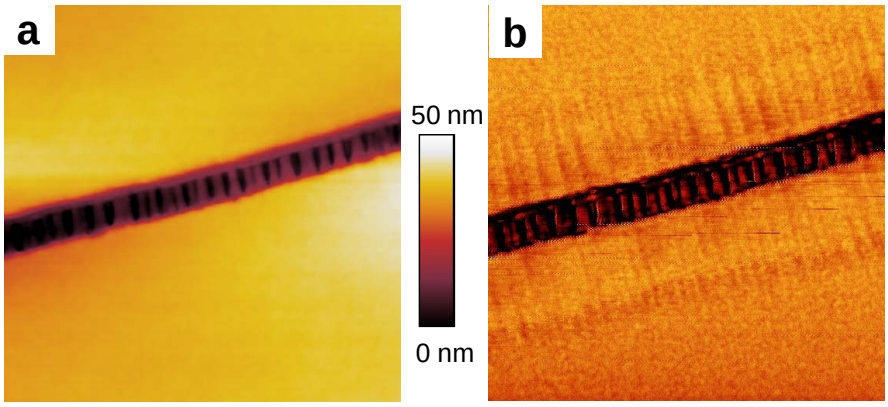

Figure 2.10 – AFM image (size 1 x 1 µm²) of craze nano/microstroctures consisting of voids and fibrils in a ca. 40 nm thin film of PS (M_w = 4060 kg/mol) aged for 24 hours at 90 °C. (a) height image (b) phase image, showing a stripe-pattern orthogonal to the craze direction, hints at periodic 'stiffening'.

problem was overcome by changing the scan angle in such a way so that both crazed lines were scanned at some angle. Our observations are in agreement with Yang *et al.*, where they concluded fine craze fibril structures were quite sensitive to the scan contact force and the fibril topography was insensitive to the perpendicular (to the crazed line direction *i.e.* parallel to the craze fibril direction) scanning direction [121]. They also noticed permanent tip induced damages when scanned in the paralllel (to the crazed line direction *i.e.*, normal to the craze fibril direction) scanning direction.

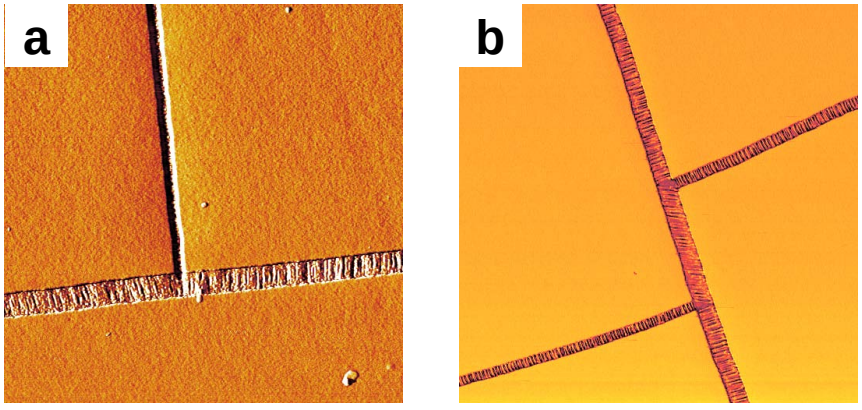

Figure 2.11 – AFM phase images of typical craze junctions in a ca. 40 nm thin film of PS (M_w = 4060 kg/mol) aged for 24 hours at 90 °C. Size of each image: 5 x 5 µm² (a) Image with artifacts. Due to high scan speed and nearly perpendicular position of the smaller width craze line (b) Fibrils inside all of the craze lines are visible. None of the craze line is perpendicular to the scanning direction.

Employing high scan speed can lead to an artifact in a form of a white line at the edge of the crazes (cf. **Figure 2.11**). This problem was successfully

overcome by applying an optimum scan rate for imaging. Part of this work is dealing with cracking/crazing due to immersion of PS thin films in plasticizing non-solvents (*e.g.* heptane). These films, exposed to non-solvents, had a surface that was not totally dried but covered with a very thin liquid layer. Consequently, it was not possible to see the morphology of the solid objects using very weak force. Thus, we had to increase this force (tapping harder) to go through the thin liquid layer covering the film morphology. As such non-solvent immersed "sticky" sample surfaces were measured, the tip was often contaminated with amorphous polymer molecules which got attached to the tip, introducing artifacts. In order to avoid such tip contamination, high oscillation amplitudes (> 50 nm) were used. Another important consideration when measuring our samples concerns convolution effect resulting from the finite AFM tip diameter. In our case the tip diameter is ca. 8 nm. So, the tip could not measure voids between fibrils with widths (or void between fibrils) smaller than the size of the AFM tip.

Considering our viscoelastic thin PS films, the dewetting hole growth dynamics is governed by the ratio $\frac{\sigma}{E}$ of the total stress σ acting on the film to the elastic modulus E. Rim shape, especially rim height H can be considered as the signature of residual stress (as the capillary stress is constant), or the elastic modulus inside the film [45,81,102]. So, proper implication of tapping mode AFM was important in our experiments, to obtain the rim profile (height) of dewetted holes. Detailed studies concerning rim shape and extent of residual stress present inside the thin film will be presented on **Chapter 3**.

2.4 Ellipsometry

Ellipsometry is an optical technique to characterize thin film properties such as film thickness, index of refraction. In our work, we use ellipsometry to measure thickness of thin polymer films [154]. We used Optrel Multiskop®in the ellipsometry mode.

Due to the change of the polarization state of light reflected off or transmitted through film samples, an ellipsometer can measure film thicknesses ranging from several angstroms to micrometers. **Figure 2.12** depicts the major schematic outline of an ellipsometer. Linearly polarized light with two components p and s is shined onto the film sample at an incidence angle θ_i, then the sample reflection will introduce amplitude variation and phase shift to the p and s components of the reflected light. Since the p-electric field oscillates in the plane of incidence and

the s-electric field oscillates perpendicularly to the plane of incidence, from mathematics we know that two vectors oscillating perpendicularly with each other with a non-zero phase difference will produce a resultant vector oscillating elliptically. As shown in **Figure 2.12**, the reflected beam is an elliptically polarized light with

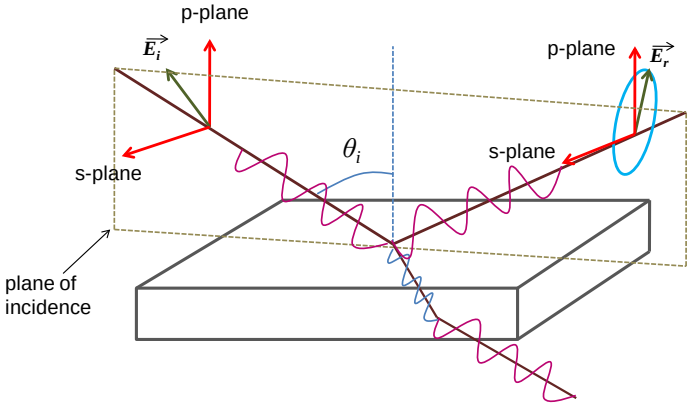

Figure 2.12 – Schematic geometry of the reflection ellipsometry. Reproduced inspired from ref. [137].

the resultant electric field vector E_r. For a self-nulling ellipsometer, the system will adjust the polarization state of the incident light to a specific situation where the p and s components have some amplitude and phase differences which can be cancelled out by the sample reflection and accordingly the reflected light is just linearly polarized. This is actually an application of the reversibility principle in optics. Conventionally, an ellipsometer uses a combination of a polarizer and a quarter wave plate to adjust the polarization state of the incidence light, and the linearly polarized light can be detected using another polarizer named analyzer. When the direction of the oscillating electric field of the reflected light is perpendicular to the transmission axis of the analyzer, there will be no light reaching the optical detector, which is the null condition.

The quantities measured by an ellipsometer are the ellipsometric angles φ and Δ. These angles are related to the ratio of the complex Fresnel reflection coefficients r_p and r_s for p and s polarized light with respect to the plane of incidence according to

$$\frac{r_p}{r_s} = \tan(\varphi)\exp(i\triangle) \sim \frac{R_p}{R_s} \tag{2.10}$$

Since the reflected and incident wave propagates in the same medium and make same angle with the surface normal, the amplitude reflection coefficient (Fresnel coefficient, r) can be related to total reflection coefficient R as $R = |r|^2$. The total sample reflection coefficients R_p and R_s include sample properties such as

thickness and index of refraction of the individual materials. In the conventional self-nulling ellipsometer, the directly measured variables are angles of the polarizer and analyser with the fixed angle of incident, which are related to φ and Δ. The reflectance ratio (R_p/R_s) is completely determined by the amplitude ($\tan\varphi$) and phase (Δ). The differential changes in amplitude and phase are related to the transformation of the shape and orientation of the ellipse of polarization. From **Equation 2.10**, we see that the ellipsometry actually measures the ratio of reflection of the p and s components. Therefore, the absolute values of intensity of the light beam do not matter . To find the sample property parameters from the measured variables Δ and φ, an optical model consisting of layered media is necessary, adjusting individual layer thickness (or index of refraction) as variables. An iterative fiiting procedure can give the thickness data. For our films, we used $n_{\mathrm{PS}} = 1.59$ and $n_{\mathrm{PDMS}} = 1.46$ as the refractive index.

Chapter 3

Relaxation Dynamics of Residual Stresses in Glassy Thin Polymer Films during Physical Ageing

3.1 Abstract

The fabrication process of a thin polymer film, involving the transition from a (dilute) solution to a dry glass, is believed to have an impact on film properties, often related to poorly entangled out-of-equilibrium chain conformations and corresponding residual stresses. Thus, a central question concerns the possibility of relaxation of such chains even in the glassy state. Physical ageing of polymer films at temperatures below the glass transition was found to lead to a progressive decrease in dewetting velocity, which is indicative of a decreasing residual stress or an increasing modulus with ageing time. Dewetting shows a close to exponential decay with ageing time, defining a characteristic relaxation time. We found, at all ageing temperatures these relaxation times were much faster than the relaxation times of the bulk polymer. Variation of relaxation times with temperature seems to follow Arrhenius temperature dependence. This suggests a process of relaxation which takes place at the segmental level of the polymer and is sufficient to relax part of the residual stresses. The relaxation dynamics of residual stresses appears to be in close agreement with some earlier reports, concerning relaxation solely at the surface of polymer thin films. This intriguingly invokes the possibility to correlate the surface mobility in thin polymer films with non-equilibrium conformations of polymer chains. Films prepared from solutions close to the theta temperature were aged for varying times at room temperature and theier dewetting behaviour was measured. The characteristic relaxation time of ageing varied

strongly with the quality of the solvent, which is attributed to distorted chain conformations in the as-cast films. This signifies the non-equilibrium nature of thin polymer films, possibly causing some of their unexplained properties, such as fast relaxation.

3.2 Introduction

3.2.1 Enhanced mobility and physical ageing in thin polymer films

Enhanced mobility in thin glassy polymer films has been debated controversially since the last two decades and as a major concern in the area of polymer physics [61]. Already about two decades ago Reiter found enhanced mobility in thin polymer film dewetting [37] and Keddie *et al.* reported the first systematic study of glass transition temperature (T_g) reduction in thin polymer films [13]. Since then, several attempts have been made to characterize relaxations in a glassy thin films, probing the global dimension as well as the surface or interface selectively. A special attention has been given to physical ageing, a process of sub-T_g relaxation, possibly occurring at the segmental scale of the glassy polymer. Most of the earlier studies tried to explore the effects of film thicknesses on the physical ageing of PS thin films. Kawana *et al.* did ellipsometric measurements on supported PS films [44]. Structural relaxation can produce an overshoot in the expansivity-temperature curve when aged samples are reheated. They needed to age their PS thin films at 80 °C for 7 days to observe a characteristic relaxation peak upon heating through the T_g ($T_{g,\ bulk}$ of PS is ca. 105 °C). With decreasing film thickness there was a reduction in the development of ageing relaxation peak indicative of decreasing ageing rate, ultimately to disappearance for the thinnest film of 10 nm. Another interesting observation was the appearance of the expansivity overshoot always at ca. 100 °C while the T_gs of sub-30 nm films were distinctly reduced with respect to the bulk. These results suggest the existence of a spatial distribution of T_gs inside the film leading to a spatial distribution of physical ageing rates, depending upon the difference of ageing temperature and glass transition temperature [43].

Nearly at the same time, the Torkelson group developed a fluorescence multilayer method to determine distributions not only of T_g but also of physical ageing in thin PMMA films [155, 156]. By inserting dye-labelled molecules at known positions inside the film, they mapped out the effective glass-transition

temperatures as a function of distance from the surface of the film. For a relatively thick film, it was found that within 14 nm of the free surface of the film, there is a region of higher mobility showing depression in glass transition. They found that perturbations to T_g at a free surface or polymer-substrate interface can propagate several tens to hundreds of nanometers into a film and that the strength of the gradient in T_g is strongest at the free surface or interface. Theoretical prediction by de Gennes, on the mechanism of glass transition on free-standing polymer film states: enhanced relaxation (mobility) of a glassy surface deals with the motion at the segmental scale (sliding motion around the chain ''loops or bridges'') and its propagation towards interior [67]. This argument was later questioned by Kim and Torkelson [157]. By probing a multilayer free-standing PS film by fluorescence spectroscopy they found no mid-layer chain loops or bridges reached a surface. Instead of that, major T_g reductions were observed in such mid-layers disproving that mechanism. Furthermore, Priestley *et al.* had shown that the length scales over which physical ageing can be affected by confinement can exceed those associated with changes in T_g [156]. They found physical ageing rate is extended some 200 nm from both the interfaces while dealing with a PMMA multilayer film on a solid substrate. While ageing at $T_{g,bulk}$ - 87K, the middle layer showed highest ageing (representing bulk behaviour), reduced ageing at the free surface and almost complete suppression of ageing at the substrate-polymer interface.

Questions concerning the thickness dependence of physical ageing have also been addressed by several authors. Pye *et al.* showed a decreased rate of physical ageing in thin PS films which can be correlated with the thickness dependent glassy dynamics of thin polymer films, usually accepted as the layer model [13,59,63,158]. Another possibility employed by them was a gradient model considering an exponential decay of the physical ageing rate from zero at the free surface to its bulk value at a depth sufficiently far from the free surface. According to both of these models, thickness of mobile surface layer grows with decreasing ageing temperature. This observation appears just opposite to what Ediger *et al.* found both for supported and free standing films [49, 66]. Very recently Frieberg *et al.* tried to disentangle the physical ageing dynamics from the corresponding average T_g of the whole polymer thin film [159]. According to them, the slower physical ageing rate in thin films (compared to the bulk polymer) is associated with the difference between local T_g at the interfaces and temperature of ageing. They reconcile these changes in physical ageing in terms of a model that accounts for gradients in the local T_g of the film in the vicinity of interfaces. Apart from that, a dependence of physical ageing rate on macromolecular architecture was

found. A star shape PS showed higher rate of physical ageing as compared to linear PS.

Though most of the literature reported a reduction of ageing rate with decreasing film thickness, few studies pointed out the opposite. Such as, gas permeation study of micron thick glassy polysulfone (PSF) gas separation membranes [160, 161]. Variable energy positron annihilation lifetime spectroscopy (PALS) studies on PSF films (thickness ca. 450 nm) showed a decreasing ortho-positronium life time at the free film surface, indicative of smaller free volume elements near the film surface in comparison to the bulk interior [162]. These surface regions of the films age dramatically faster than the bulk PSF. They commented such accelerated ageing is in accordance with the enhanced mobility of the thin film surface. This allows polymers near the surface to reach a lower free volume state more quickly than the bulk.

The search for surface relaxation in thin films shares the long-standing question of reduced glass transition of thin films mostly pointing towards the existence of a highly mobile film surface. There are several surface sensitive techniques to particularly probe the surface relaxation such as atomic force microscopy (AFM) [46, 47, 163, 164]. Fakhraai and Forrest measured the surface mobility of PS thin films by probing the healing of nano-deformation on the surface by measuring the depth by AFM at different temperatures well below the $T_{g,bulk}$ of the polymer [46]. Although the enhanced mobility and faster relaxation at the glassy film surface were already shown previously, it was the first quantitative measurement of the surface relaxation over a wide range of temperatures. This showed the markedly different surface relaxation process in polymer thin film in comparison to the bulk relaxation. On the same line of thought, a very recent study has been reported by Siretanu *et al.* [47]. They probed the near-free surface dynamical properties of thin polystyrene films by AFM by measuring the height of nano-sized bumps, which were produced on polystyrene thin films under the influence of ions dissolved in degassed water, over a wide range of temperature below the glass transition. Relaxation times were found in close agreement with the findings by Fakhraai *et al.* [46].

3.2.2 Different relaxation processes in polymers

In equilibrated bulk samples, the existence of entanglements implies that the longest relaxation time (reptation time) strongly depends on molecular weight

(M_w) according to a power law, $\tau_{REP} \sim M_w^{3.4}$. In general, glassy polymers exhibit more than one relaxation processes on various timescales. There is a high temperature relaxation, usually labeled as α, which indicates the glass transition and corresponds to the onset of main chain segmental motion [20]. Generally, for bulk polymers the α-process of relaxation represents a cooperative dynamics at the segmental scale, which can be described well by the Vogel-Fulcher-Tamman function,

$$\tau_\alpha = \tau_\infty \exp \frac{E_0}{R_k(T - T_0)} = \tau_\infty \exp \frac{B}{T - T_0} \tag{3.1}$$

(τ_α = relaxation time, τ_∞ = constant depending upon the material, B = constant = E_0/R_k, R_k = gas constant , E_0 = Vogel activation energy and T_0 is a constant temperature depending upon the material) or by the equivalent William-Landell-Ferry function [18],

$$\log a_T = \frac{-C_1(T - T_{ref})}{C_2 + (T - T_{ref})} \tag{3.2}$$

This defines a shift factor (a_T) to determine the relaxation time. C_1 and C_2 are adjustable constants depending upon the material. The WLF and VFT parameters are quantitatively related, $C_2 = T_{ref}$-T_0 and 2.303 $C_1C_2 = E_0/R_k = B$ [19].

α-relaxation data (in the region $T \geq T_g$) for bulk polystyrene by Lupascu *et al.*(through capacitive dilatometry and dielectric spectroscopy) and Dhinojwala *et al.* (through dye-orientation dynamics by second harmonic generation and dielectric spectroscopy) was found to follow VFT and WLF laws respectively [165, 166]. They found below the T_g, the relaxation time showed an apparent Arrhenius temperature dependence,

$$\tau(T) = A \exp\left(\frac{E_A}{k_B T}\right) \tag{3.3}$$

(τ = relaxation time, B is a constant, k_B = Boltzmann constant and E_A = activation energy). Interestingly, α-relaxation time (both for thin film and bulk PS) follows VFT dynamics, while the secondary α-relaxation process for the thinner films follows a non-cooperative Arrhenius dynamics at the sub-T_g region, invoking the possibility of a distinct surface layer of higher mobility or a region with an increased heterogeneity in the dynamics [165, 167, 168]. It is surprising

to observe a dynamic relaxation in the glassy state. Such relaxation process is mainly dominated by β-relaxation processes, which involves non co-operative motions at the segmental scale of the main chain and also the motion of side chains. Such non-cooperative processes (such as β-relaxation or any secondary relaxation) follow Arrhenius dynamics.

Activation energy values corresponding to different relaxation processes in thin films could be of interest, in order to determine the type of motion associate with that process. The literature value of activation energy for the β-process in bulk PS was estimated to be ca.125 kJ/mol. [169] Dhinojwala *et al.* found Arrhenius temperature dependence of relaxation time at the sub-T_g region with estimated activation energy of 190-210 kJ/mol for bulk PS [166]. Recent result for unentangled short chain PS thin films (for thickness < 9 nm) indicated the possibility of the presence of a highly mobile surface layer of thickness less than 2.3 nm [164]. They have shown that such surface exhibit Arrhenius relaxation dynamics corresponding to activation energy of 185 kJ/mol. Experiments through the lateral force microscopy measurement attempted to identify the process of surface relaxation and the values of apparent activation energy for PS thin films of varying thicknesses [48]. They found a surface relaxation peak (α_a, similar to a secondary α-relaxation process) in lateral force corresponding to segmental motion of polymer chains well below the bulk glass transition temperature. This is invariant with film thickness and corresponds to activation energy of ca. 230 kJ/mol. For confined thin films, they found a broadening of that α_a-peak, finally leading to the generation of another peak interpreted as surface β-relaxation process. The apparent activation energy of the β-relaxation process was found to be decreased with decreasing film thickness. While for a ca. 65 nm thick film it was close to the value corresponding to the α_a-process (ca. 200 kJ/mol), for the β-process it was decreased upto ca. 55 kJ/mol [48]. Observations by Akabori *et al.* invoked the important question, whether β-relaxation at the film surface is induced by ultrathinning. Recent experiments by Paeng *et al.* indicated the existence of a highly mobile surface layer in thin PS films, which is constant irrespective of film thickness but increases upon increase in temperature to ca. 7 nm at $T_{g,bulk}$ [49, 66]. The sub-T_g fast relaxation in their experiment was an Arrhenius process of ca. 100 kJ/mol. This value is close to the activation energy found from the surface sensitive measurements on the relaxation of nanobumps [47] and nanodeformations [46] on thin PS films.

Activation energy values by Lupascu *et al.* (through dieletric spectroscopy) was found to be around 80 kJ/mol and initially interpreted as a sec-

ondary relaxation process (similar to α_a) which might be assigned to distinct non-cooperative surface dynamics in polystyrene films, as suggested mostly in recent papers [165]. Later, they explained it as a different dynamic process which cross the α-relaxation region without merging, might be indicative of a molecular mechanism involving a region phase-separated from the amorphous PS fraction [170]. Arrhenius temperature dependence was valid for a wide range of temperature below and above the $T_{g,bulk}$ of the polymer. Preliminary argument by them considers the presence of high fraction of syndiotactic sequences in the atactic molecule resulting spatially organized aggregates of helices as PS gels and hence operative for PS samples prepared from solutions. Such, secondary relaxations (termed as β_1 and β_2 respectively for the fast and slow mode) was supposed to be originated from cooperative helix inversion events [170]. Eventually, presence of a distinct gel-like skin layer was much discussed as a rapidly vitrified 'crust' for spin-coated thin polymer films [171, 172]. Details of this possibility will be followed in the next section.

3.2.3 Relaxation in non-equilibrated thin polymer films

Dealing with non-equilibrated glassy films, one cannot expect the same type relaxations as reptation in them, which occurs in equilibrated bulk polymers. Several attempts have been made to correlate the thin film relaxation dynamics with the out-of-equilibrium polymer chain conformations inside the spin-coated film, allegedly generated due to the fast evaporation of solvent during spin-coating. As the solvent content is reduced during spin-coating, during a time depending upon the volatility of the solvent, the glassy state freezes-in below a certain solvent content, which for the polystyrene-toluene pair is $\sim$ 14-20% by mass of toluene. This indicates a large shrinkage in the glassy state during evaporation of the remaining solvent molecules. Apart from that, several puzzling observations in thin spin-coated polymer films, such as negative expansion coefficient [38,40,41], faster sub-T_g ageing [42] and enormously low elastic modulus [74,75] essentially demand some unification of arguments correlating mobility (relaxation) and polymer chain conformations inside the film. Grohens *et al.* came up with the possibility to correlate the enhanced surface mobility (in other way the reduced glass transition temperature) of the polymer thin film with the presence of a skin-like structure at the surface of the thin film [172]. De Gennes argued that such a 'crust' layer turns glassy much more rapidly compared to the interior regions of the film [171]. Such layer is supposed to be highly stressed and more out-of-equilibrium than the rest of the film while less entangled. This fact was supported by a recent

observation where Thomas *et al.* observed stabilizing surface pressures and lowered viscosity in their electro hydrodynamic destabilization experiments in thin polymer films [173]. Contribution of non-equilibrated and distorted chain conformations might be related to a nearly constant thickness region of non-equilibrated polymer layer (similar to 'crust) irrespective of total film thickness. Recent experiments by Paeng *et al.* indicated the existence of a highly mobile surface layer (both for supported and free-standing films), which is constant irrespective of film thickness [49, 66].

One has to also consider the effect of chain conformation and entanglement situation in the spin-coated film. Polymer chains are generally believed to have a distorted (oblate polymer coils due to a possible radial stretching during spin-coating) chain conformation with reduced inter-chain entanglement in a thin spin-coated film (discussed in detail in **Section 1.3.3**) [45,59,76,91]. Prior experimental observations largely suggested that the reduction of entanglement density has no relation with the enhanced surface mobility of thin polymer films [86,174]. This observation might be supported by the following: If distorted and poorly entangled chain conformations are responsible for T_g reductions, this mechanism should not be operative for short chain polymers (below entanglement length). But high surface mobility (or T_g-reduction at surface) was also found for unentangled polymer thin films [164]. Apart from that, lower film thickness should contribute to higher distortion of polymer chain coils (more oblate shaped); in that sense there should be a thickness dependence of T_g which would be similar for supported and for non-supported films. Prior reports distinctly identified two different thickness dependences of T_g for supported and free-standing films [59].

Though, at present we have no explanation to correlate high mobility of chains in a highly non-equilibrated layer. Our recent results on varying relaxation times in polymer films, casted from different quality of solvents, clearly indicate the role of non-equilibrated chain conformations on the mobility of thin films [45]. The basis of the present work has been originated after the observation of fast ageing by Reiter *et al.* [42]. They interpreted their result in terms of relaxation of residual stresses, which can be generated inside the films due to distorted chain conformations, providing an additional driving force for dewetting and thereby accelerating this process. Reiter *et al.* showed residual stresses are (partially) relaxing even in the glassy state of the film (even 80 °C below the $T_{g,bulk}$ of PS), which is quite surprising. By the increase of ageing duration they found a systematic decrease in number of spontaneously nucleated holes per unit area, dewetting velocity and rim shape (rim width and rim height), which has been

related to the decay of residual stresses. Present work is focused to follow the dynamics of residual stress relaxation over a wide range of temperatures below the $T_{g,bulk}$ of PS.

The process of dewetting actually involves displacement of whole polymer chains in the thin film. Dewetted hole formation takes place when the film is heated at a temperature above the bulk glass transition temperature (ca. 105 °C) of the polymer. In our experiments where a generated in-plane stress dominates dewetting, the dynamics is governed by the ratio of the total generated stress (σ) in the film to the elastic modulus (E) as

$$\frac{\sigma}{E} = \frac{\sigma_{S+}\sigma_0}{E} \tag{3.4}$$

σ is determined by capillary stress (σ_S) at the film (being determined the spreading coefficient $|S|$ over the film of thickness h_0), residual stress (σ_0) and elastic modulus (E) [81]. Damman *et al.* tried to disentangle the capillary stress and residual stress. Numerical calculation by Vilmin *et al.* clearly showed that the residual stress constitutes an additional driving force for the dewetting. In the presence of a residual stress, in the consideration of the linear friction regime, and at times shorter than the relaxation time of the polymer the initial velocity of the dewetting process is increased by a factor of $(1 + \frac{h_0\sigma_0}{|S|})$ [102, 105]. The rim height in a dewetted hole can be expressed as

$$H = h_0 + \frac{|S|}{E} + \frac{h_0\sigma_0}{E} \tag{3.5}$$

In terms of **Equation 3.4 and 3.5** one can see that the σ_0/E ratio can contribute significantly to the initial hole-opening kinetics. The decay of σ_0/E with time supports the hypothesis that the chains in the films, which were initially out of equilibrium, equilibrate while dewetting.

3.3 Experimental

All the experiments involved systematic ageing of thin PS films at different temperatures, starting from room temperature (25 °C) up to 90 °C. Ageing is followed by dewetting of the same film at 125 °C to check the extent of residual stress inside the film by investigating the hole growth kinetics (temporal evolution of hole growth, cf. **Figure 3.1**). The experiments were performed mainly on high molecular weight polystyrene films (PS, M_w = 4060 kg/mol, M_w/M_n = 1.15,

thickness = ca. 40 nm thick), spun-cast from solutions of toluene, an athermal solvent for PS. Comparison was also made with the faster relaxation times at room temperature found from similar films spun from a trans-decalin (a theta-solvent for PS at 21 °C). Higher molecular weight PS (16800 kg/mol, M_w/M_n = 1.3) had been used to compare the relaxation time at few of the examined ageing temperatures. All the films were spun at 3000 rpm on Si (100) substrates, which were previously coated with an irreversibly adsorbed thin non-wettable PDMS (M_w =139 kg/mol) layer of ca. 15 nm thickness [42].

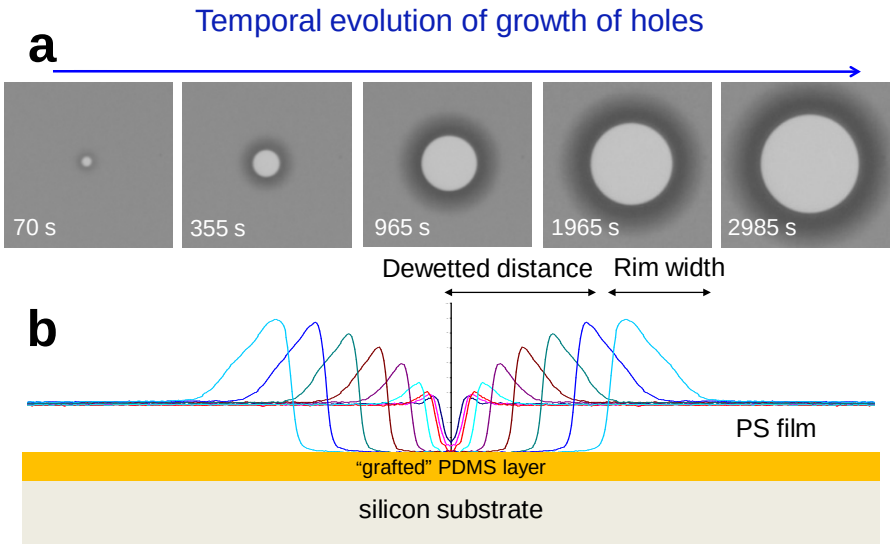

Figure 3.1 – (a) Temporal evolution of growth of holes in an as-spun PS film (ca. 40 nm thickness, M_w = 4060 kg/mol) during dewetting at 125 °C, obtained by optical microscopy. Size of each of image is 32 x 32 μm^2. (b) The similar process is shown in terms of growing hole profiles obtained from optical micrographs considering the gray channel. **b** is adapted from ref. [175].

The procedure to preparation of PDMS layer has been discussed in **Section 2.1.3** of this thesis in details. The PDMS layer acts as a liquid layer enabling slippage, thus facilitating dewetting of PS film. Systematic ageing at different temperatures below the $T_{g,bulk}$ had been done in an oven equipped with an oil free vacuum pump, for periods of several hours to days. Subsequently, all those already aged films were subjected to dewetting to determine the extent of changes caused by ageing. Temporal evolution of dewetted hole growth was followed in real time by optical microscopy during the early stage of dewetting at 125 °C for ca. 1 hour. Dewetting experiments were used to highlight the presence of a characteristic time, τ_W, corresponding to the dewetting time at which the rim width reaches the maximum value ($W_{\max}$) [42]. This time can be related to the relaxation of residual stresses present in the film and is drastically shorter than

the longest relaxation time of the polymer in an equilibrated bulk, the reptation time τ_{REP} [57]. While dewetting at 125 °C, $W_{\max}$ in our films was reached around 9000 s after inducing dewetting (PS of M_w = 4060 kg/mol), irrespective of the duration of ageing. It is important to follow a hole right from its birth to know the exact thermal history applied to it. It is also important to exclude any hole which appeared to be nucleated from dirt particles or flaws that can be avoided by careful film preparation.

3.4 Results and discussions

3.4.1 Dynamics of residual stress relaxation during physical ageing

Hole growth in a film is believed to occur through a heterogeneous nucleation and growth mechanism where the probability of hole nucleation and hole growth dynamics are largely dependent on the residual stresses inside the film [42]. Time evolution of dewetted hole radius for a typical PS film with varying duration of ageing is shown in **Figure 3.2** for three different ageing temperatures. Dewetting is decelerated with time, which means dewetting velocity is decreasing in the course of hole growth. In addition, the dewetting velocity depends on ageing time. It can be seen at a fixed dewetting time in terms of decreasing dewetted hole radius (R), rim width (W) and rim height (H) upon physical ageing (cf. **Figure 3.2, Figure 3.3, Figure 3.5**).

One can follow the dewetting velocity (or hole radius) at a particular dewetting time as a function of ageing time to see the extent of residual stress present inside a film. Dewetted hole radius (R) at particular times (such as at 1000 s of dewetting) can be followed to see its variation upon ageing. The dewetted hole radius showed an exponential decay with ageing time (t_{age}) as, $R(t_{age}) = R(\infty) + \Delta R(0)\exp(-t_{age}/\tau)$, defining a characteristic relaxation time (τ) for ageing. Further, we used normalized hole radius (by the hole radius of the corresponding as spun sample) for all the PS films at different ageing temperatures and followed its decay upon ageing. Exponential decay defining a characteristic relaxation time (τ_A) for ageing can be obtained.

$$\frac{R}{R_0}(t_{age}) = \frac{R}{R_0}(t_{age} = \infty) + \Delta\left(\frac{R}{R_0}\right)\exp(-t_{age}/\tau_A) \tag{3.6}$$

It was found that a single exponential can be used to describe the present case

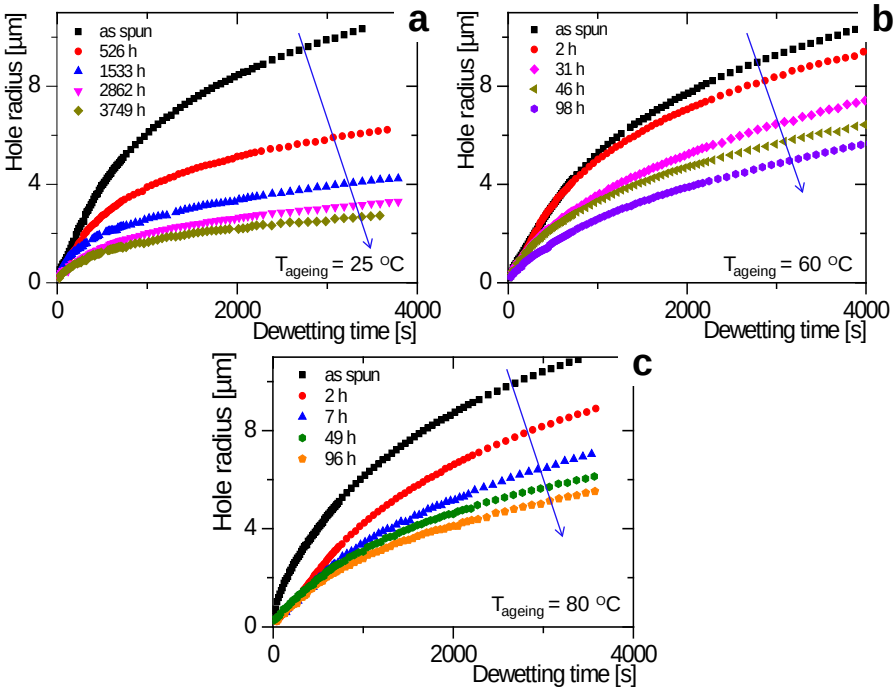

Figure 3.2 – Growth of dewetting holes nucleated immediately upon heating to 125 °C in PS films (42 ± 2 nm thickness, $M_w = 4060$ kg/mol) that have been aged at (a) 25 °C, (b) 60 °C and (c) 80 °C, exhibiting at any dewetting time decreasing hole growth velocities (slope of hole radii) with increasing ageing time. At a fixed dewetting time hole radii can be compared as a function of ageing time. Blue arrows are showing the direction of increasing ageing time.

of relaxation of residual stresses for all the ageing temperatures. **Figure 3.4 a** is showing the exponential decays of dewetted hole radius as a function of ageing time at different ageing temperatures. Similarly, we have also considered the decay of the rim width maximum value ($W_{\max}$) upon ageing as reported earlier on PS films of similar thickness and molecular weight ($M_w = 4840$ kg/mol) (cf. **Figure 3.4 b**) [176]. Similar exponential decay defining a characteristic relaxation time (τ_A) can be found.

$$\frac{W_{max}}{W_{max}(0)}(t_{age}) = \frac{W_{max}}{W_{max}(0)}(t_{age} = \infty) + \Delta\left(\frac{W_{max}}{W_{max}(0)}\right)\exp(-t_{age}/\tau_A) \qquad (3.7)$$

It is possible to find a shift factor, a_T, in time such that the relaxation curves at different temperatures can be superimposed. This is a commonly used technique to describe the temperature dependence of relaxation times in glass-forming materials. **Figure 3.4 a-b** shows the exponential decay plot (for invidual ageing temperatures). **Figure 3.4 a'-b'** show the shifted cumulative master plots where the normalized radius or rim width is plotted with a dimensionless ageing time (here divided by the ageing time when the normalized radius or rim width

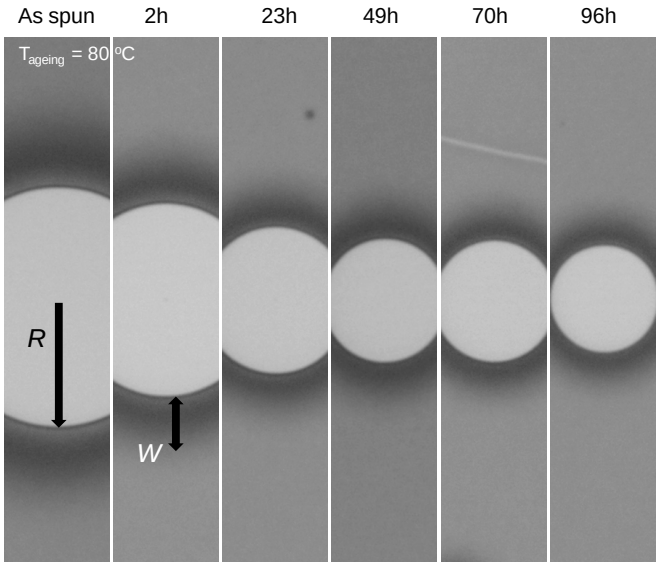

Figure 3.3 – Section of dewetted holes (optical micrographs of size 14 x 70 μm^2 each) after ca. 1 hour dewetting at 125 °C in PS films (42 ± 2 nm thickness, M_w = 4060 kg/mol) that have been aged at 80 °C for varying periods (mentioned above each image, from 2 hours to 95 hours). It is clear from the images that dewetted hole radius and rim width (after a certain period of dewetting) decreases upon increasing duration of ageing.

was at 0.75).

The rim shape of a dewetting hole is dependent on the viscoelastic properties and energy dissipation mechanisms of the film in which it grows. As already discussed, strongly asymmetric rim shapes with a gradual monotonic decay to the unperturbed film are observed, until a characteristic time when the rim width reaches maximum, defining a characteristic time for residual stress relaxation. For the case where a generated in-plane stress dominates dewetting, rim shape (both rim width and rim height) is dependent upon the capillary stresses (σ_S) at the dewetting front, residual stresses (σ_0) inside the film and elastic modulus (E) (cf. **Equation 3.4 and 3.5**) [45, 81, 102]. Apart from that, rim width (W) is dependent upon the interfacial (film-substrate) friction of the film ($W \sim h_0\eta/\zeta$, where η is the viscosity and ζ is the friction coefficient) [42, 102]. It is clear that the rim height is not directly related to the interfacial friction and entirely depends upon the total generated in-plane stress inside the film. So, a decreased rim-height upon physical ageing signifies either a lower residual stress in the film or a higher modulus (cf. **Figure 3.5**) [45,102]. Rim height showed an exponential decay with ageing time (t_{age}) as, $H(t_{age}) = H(t_{age} = \infty) + \Delta H(0)\exp(-t_{age}/\tau_A)$, defining a characteristic relaxation time (τ_A) for ageing. The chararacteristic relaxation times (or shift factors) found from the experiments of decay of hole radius (R), rim width maximum (W_{max}) and rim height (H) upon ageing were

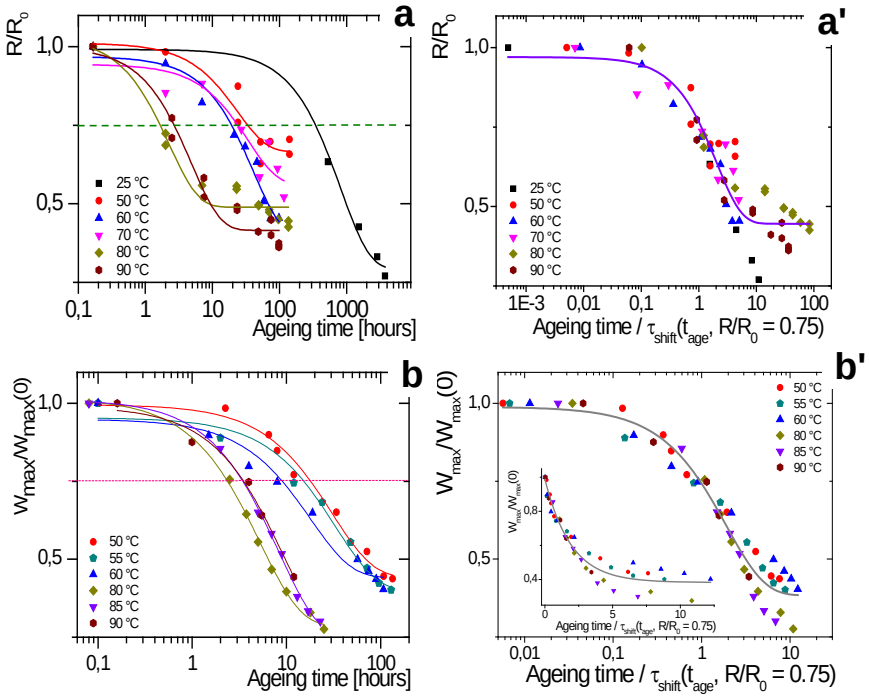

Figure 3.4 – (a) Hole radii [taken at 1000 s of hole growth] and (b) rim width maximum ($W_{\max}$) follow an exponential decay with a characteristic time as a function of ageing time. Solid lines represent the fit to the exponential **Equations 3.6 and 3.7**. For all the cases PS film thickness was set at 42 ± 2 nm over a 15 nm PDMS layer. Molecular weights of PS were, M_w = 4060 kg/mol (for hole radii experiments) and M_w = 4840 kg/mol (for rim width experiments). Ageing temperatures are mentioned in the corresponding plot legends. (a'-b') Shifted cumulative master plots where the normalized radius or rim width is plotted with a dimension less ageing time (here divided by the ageing time when the normalized radius or rim width was at 0.75). Data for the rim width experiments were taken from ref. [176]. Inset in (b') is indicating the same plot on linear-linear scales.

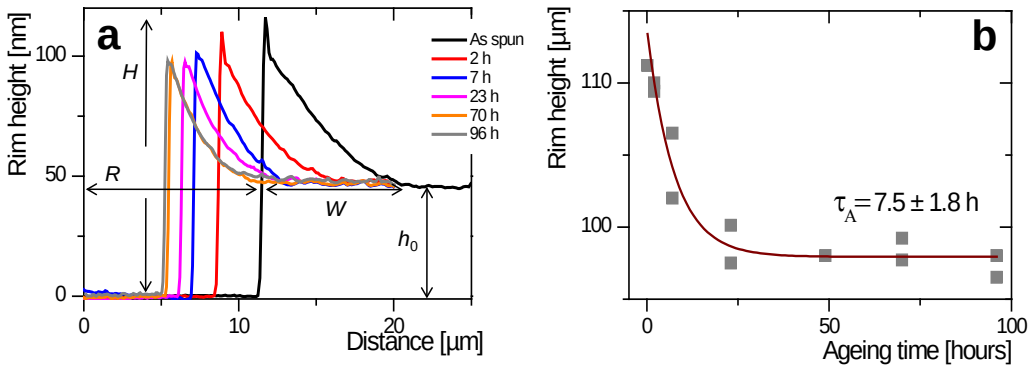

Figure 3.5 – (a) AFM rim profiles of holes grown in PS films (film thickness = 42 ± 2 nm, M_w = 4060 kg/mol) after dewetting at 125 °C for ca. 1 hour. These films have been aged at 80 °C for varying periods (mentioned in the plot legend). (b) Exponential decay of rim height upon physical ageing defines a decay time of 7.5 ± 1.8 hours.

compared (cf. **Figure 3.6**). Those were found to be in good agreement.

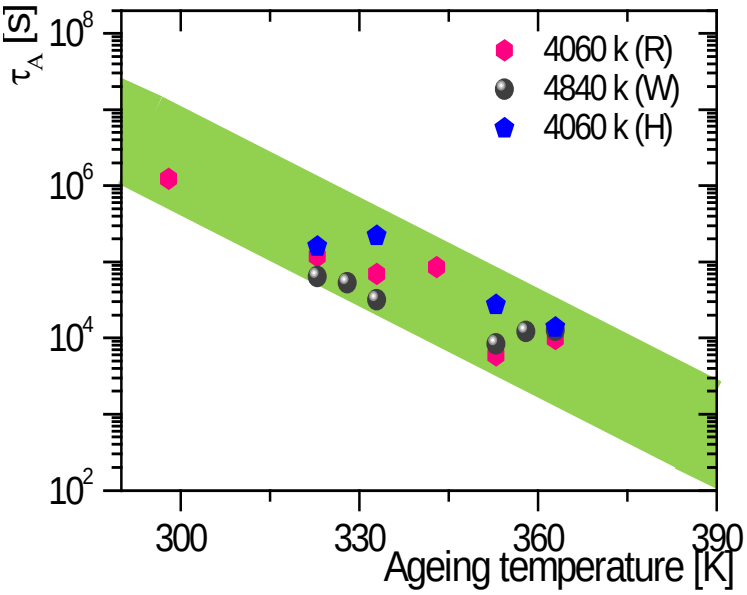

Figure 3.6 – Calculated relaxation times found from ageing experiments (determined through dewetting) on PS films (M_w = 4060 and 4840 kg/mol) with various values of relaxation times found for nominally similar films prepared from toluene. Relaxation times found from the decay of hole radius (R), rim width maximum (W) and rim height (H) are indicated. The green highlighted area is showing the Arrhenius dependence of relaxation times with ageing temperatures. For all the cases PS film thickness was set at 42 ± 2 nm over a ca. 15 nm PDMS layer.

Later on, comparison was made between the relaxation times found for two high molecular weight polymer films (ca. 40 nm films of PS 4060 kg/mol and 16800 kg/mol) while ageing at 90 °C. Though no big difference in the relaxation times of residual stresses was found, the dewetting velocity was found to be higher (faster) for the higher molecular weight film (cf. **Figure 3.7**). Due to its higher bulk viscosity ($\eta \sim M_w^{3.4}$), one would expect a slower dewetting velocity for the higher molecular weight film, but the opposite was observed. This may be attributed to the higher amount of residual stresses for the longer polymer chains confined in the reduced film thickness. Detailed discussion on the role of residual stresses on dewetting dynamics has already been made in **Sections 1.4.3 and 1.4.4**.

3.4.2 Effect of solvent quality on residual stress relaxation

In comparison to films spun from toluene, faster relaxation at room-temperature (up to two orders of magnitude faster) was found for those films spun from trans-

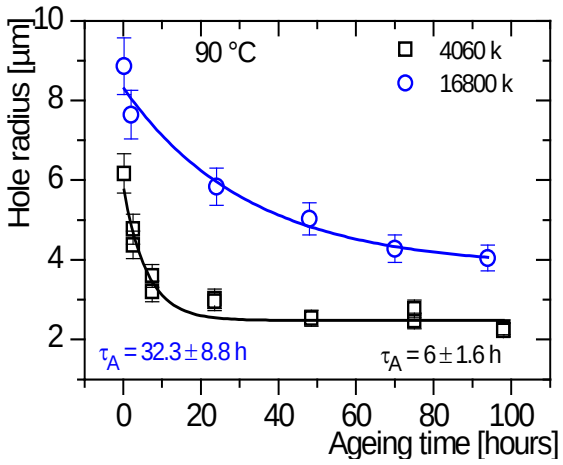

Figure 3.7 – Exponential decay of dewetted hole radii with ageing time for PS films (M_w = 16800 and 4060 kg/mol) for different duration of ageing at 90 °C). Higher dewetting velocity was found for the higher molecular weight polymer indicated by the larger hole radius at 1000 s of dewetting for the higher molecular weight polymer.

decalin (cf. **Figure 3.9**). Relaxation times were taken from **Figure 3.8 (a)**. This was interpreted by suggesting a variation of quenched chain entanglements with the quality of the solvent from which the film was spun cast [45]. The state of polymer chain entanglement in solvent was transferred to the dried film, leading to non-equilibrium conformation of chains, imparting certain residual stresses to be generated inside the film. This corresponds to faster relaxation in a film prepared from near-theta solvent (trans-decalin, T_Θ = 21 °C), than a film spun from a good solvent (toluene). Increase in the casting solution temperature above theta-temperature increases the degree of swelling (radius of gyration), leading to higher overlap between chains. This corresponds to an increase in observed relaxation times. The variation of the solution temperature thereby provides control over the swelling of PS chains in the solution over a considerable range, given by [177].

$$\left[\frac{14}{3N\alpha_{min}^3}(\alpha^3-\alpha^5)+\frac{2}{3}\frac{\alpha_{min}^3}{\alpha^3}+....\right]/c=\frac{T_\Theta}{T}-1 \tag{3.8}$$

where $\alpha = \sqrt{\frac{\langle R_g^2\rangle}{\langle R_{g0}^2\rangle}}$ is the amount of swelling. R_{g0} is the radius of gyration under ideal melt conditions, α_{min} is the amount of swelling in the fully collapsed state, N is the number of chain segments, T_Θ is the theta temperature, T is the temperature, and c is defined as $(1-\Delta S/k_B)$, with ΔS, the entropic change associated with segment-segment interactions, and k_B Boltzmann's constant.

Variation of the temperature of the spin-coating solution in **Figure 3.8**

a has a substantial effect on the room temperature relaxation times of the TD-spun films, with a change in relaxation times by a factor of 4. Films cast from toluene had a relaxation time of $\sim$ 700 hours at room temperature, in agreement with the extrapolation of **Figure 3.8 a** to the athermal limit (*i.e.*, a relative coil diameter of 2.5 with respect to theta-temperature). Conceptually, the final state

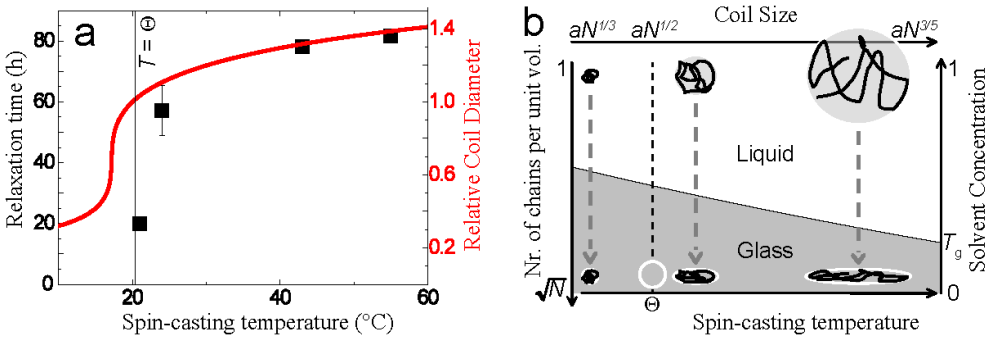

Figure 3.8 – (a) Relaxation times as a function of temperature of the solution from which the films were spun. The curve is the result of **Equation 3.8** with c as a fitting parameter. (b) Schematic of polymer coil conformations upon spin-coating for temperatures above and below T_Θ. The open circle indicates a fully entangled chain in equilibrium. Adapted from ref. [45].

of polymer chains inside the thin film must depend on the chain size in solution, which is determined by the solvent quality. Second, chain deformation must depend on the solvent concentration's at which the solution turns glassy. Both quantities are temperature dependent. The former is determined by **Equation 3.8**, while the latter is given by the Fox equation [178].

$$\frac{1}{T_{gs}} = \frac{\phi_s}{T_m} + \frac{1-\phi_s}{T_g} \tag{3.9}$$

with T_{gs} the glass transition temperature of the solution and T_m = - 35 °C the melting temperature of TD. ϕ_s varies from $\approx$ 0.5 at the TD theta-temperature to $\sim$ 0.25 at 55 °C, schematically indicated in **Figure 3.8 b**. The rapid decay of relaxation times as the spin-coating temperature approaches T_Θ is evidence for the dominating role of the solvent quality. **Figure 3.8 b** qualitatively elucidates this effect: (i) the larger the swollen coil size, the stronger the deformation of the coils in the film, the higher the in-plane tensile stress in the film; (ii) the more compact the chain in solution, the lower its number of entanglements with other chains, the lower the film modulus. A comparison of rim-height and rim-shape in dewetted films casted from different films suggested that the latter effect is dominant. Films of similar thickness (h_0) and thermal treatment spin-cast from near-theta conditions exhibit a much taller rim height and a much more rapid decay towards the film. As already discussed, an increased rim-height signifies either a higher

stress in the film or a smaller modulus [45, 102]. One thus may conclude that a more highly entangled coil conformation (arising from the deposition from a good solvent) gives rise to a higher modulus (and therefore lower rim-height) as well as to slower ageing.

3.4.3 Comparison of relaxation dynamics of residual stresses with other relaxation processes

To follow the relaxation dynamics at different temperatures, τ_A values were plotted for various ageing temperatures. The result (for PS of M_w = 4060 and 4840 kg/mol) showed a nearly Arrhenius behaviour (**cf. Figure 3.6**).The calculated activation energy was found to have the value of 70 ± 6 kJ/mol (by using **Equation 3.3** and **Figure 3.6**) and within the highlighted area it can be varied from ca. 50 kJ/mol to 107 kJ/mol. Compared to the literature values for β-relaxation, this is a rather low value [166, 169]. So, the process of residual stress relaxation during physical ageing may be considered as a process occurring locally (segmental) in the polymer. Most of the earlier studies concerning sub-T_g Arrhenius type relaxation dynamics (both in thin film and bulk polystyrene) reported the activation energy value about 150 ± 80 kJ/mol [48, 164–166]. Extrapolation of the Arrhenius line intersects the VFT line at about 108 ± 3 °C. This temperature is close to $T_{g,bulk}$ of PS, below which deviation from VFT behavior of relaxation time was observed. Our experimentally found relaxation times for the ageing have been compared with the α-relaxation times found for the bulk-PS samples by Lupascu *et al.* (through capacitive dilatometry and dielectric spectroscopy) [165]. Their reported α-relaxation dynamics was found to follow VFT laws at the above-T_g region. This is markedly different to the much shorter relaxation times found in our experiments indicating a faster relaxation process (cf. **Figure 3.9**).

Considering the possibility of faster relaxation at the film surface, our experimentally found relaxation times were also compared with the literature values of relaxation times found by different surface sensitive techniques, such as relaxation of the depth of surface deformations (which were produced on polystyrene thin films by removal of embedded gold nanoparticles) [46] and the height of bumps (which were produced on polystyrene thin films under the influence of ions dissolved in degassed water) measured through the atomic force microscopy [47]. Interestingly, with scatter the data of our results exhibit the same order magnitude in relaxation time as for the reported surface relaxation processes (cf. **Figure 3.9**). This is surprising, as dewetting cannot be considered as a surface

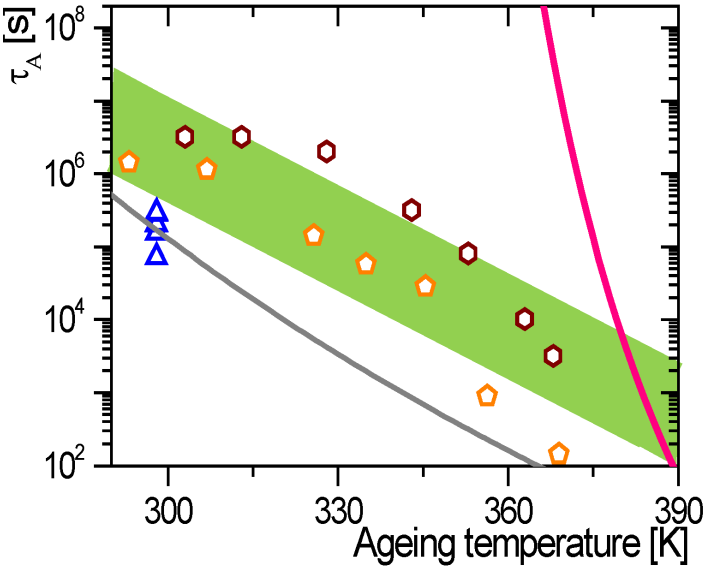

Figure 3.9 – Comparison of relaxation times found from ageing experiments (through dewetting) on PS films with various reported values of relaxation times found from different experimental techniques for PS thin films as well as for bulk. For bulk PS, α-relaxation times (rescaled for $M_w = 4060$ kg/mol from the original data, considering $\tau \sim M_w^{3.4}$ scaling) followed VFT dynamics as measured by dielectric spectroscopy (pink solid line) [165]. Surface relaxation times in thin films measured by AFM for: nano deformations in a 100 nm thick PS films of $M_w = 641$ kg/mol (orange open pentagons) [46] and nano bumps in a 300 nm thick PS films of $M_w = 250$ kg/mol (wine open hexagons) [47]. Fast sub-T_g relaxation as observed by the dye probe reorientation measuremnts in thin free-standing PS films of $M_w = 160$ kg/mol (grey solid line) [49]. The green highlighted area is showing the Arrhenius dependence of relaxation times with ageing temperatures (for all the dewetting data of PS 4060 and 4840 kg/mol spun from toluene). Data of room temperature ageing for PS 4060 kg/mol spun from trans-decalin (blue open triangles) are taken from **Figure 3.8 a**. The calculated enrgy of activation was found to be 70 ± 6 kJ/mol and within the highlighted area it can be varied from ca. 50 kJ/mol to 107 kJ/mol. For all the cases of ageing and dewetting experiments PS film thickness was fixed at 42 ± 2 nm over a 15 nm PDMS layer.

sensitive technique and involves displacement of the whole polymer chains and takes place throughout the whole film thickness. Calculated energy of activation for our residual stress relaxation measurements is closely lies with the same found from relaxation of the highly mobile surface layer in thin free-standing PS films [49] and with the surface sensitive measurements on the relaxation of surface nanobumps [47], and surface nanodeformations [46] on thin PS films. All of these measurements confirmed energy of activation of ca. 100 kJ/mol.

3.5 Conclusions

In summary, our experiments deal with the long standing question of the process of relaxation of glassy polymer films. Relaxation time for residual stresses are found to be much faster than the α-relaxation (and reptation) times of the bulk polymer, suggesting that segmental relaxations are sufficient to relax the residual stresses during physical ageing. All the published works in polymer thin films tried to look at the process in terms of the homogenous relaxation through the global thin film or gradient in relaxation process at different positions inside the thin film, such as surface, interior bulk or interface. The presented experiment probed the relaxation of residual stresses, which were supposed to be generated from the frozen-in out of equilibrium chain conformations. Our results certainly invoke the possibility to explain the unexpectedly fast surface relaxation dynamics in thin films in terms of residual stresses induced from the film preparation. The crucial role of film preparation conditions on the ageing behavior of thin films far below the $T_{g,bulk}$ of the polymer and the observation of significant changes even at room temperature may also be of relevance in the circumstance of the low softening temperature of thin polymer films, typically elucidated as a reduced glass transition temperature [104]. While the deformation of polymer coils as a whole should not modify the solidification (glass transition) temperature of the film, which is mainly governed by the segmental dynamics, our ageing experiments indicate that spin-coating influences the polymer chain conformations in coils even up to the segmental scale. The present study cannot clearly point out whether or how our observations using dewetting can be correlated with a reduced glass transition temperature. Thus, further experiments are needed to verify if non-equilibrium chain conformations inside a spin-coated polymer film can explain puzzling properties of thin polymer films like for example the deviations from the glass transition temperature in the bulk.

3.6 Addendum

Dewetting is associated with formation of holes in the film while heated well above the glass transition temperature of the polymer. All the holes do not form at the same time right after reaching the dewetting temperature, rather several holes form during the course of dewetting. Dewetting dynamics of such later initiated holes will be discussed in **Appendix-I**. Interestingly, the number of later initiated holes (secondary holes) upon dewetting increases when a film is aged at close to

$T_{g,bulk}$ of the polymer (such as 90 °C). So, a decrease in total number of dewetted holes in an aged film is not always the correct argument, as several holes nucleate during the course of dewetting (cf. **Figure 3.10 a**). Though the total sum of the area occupied by all the dewetted holes always decreases with increasing duration of ageing (cf. **Figure 3.10 b**). It is intriguing to observe nucleation of newer holes when the film has been already partially relaxed through ageing and incubation at the dewetting temperature. This fact is somewhat in the same line of thought invoked through the earlier report by Richardson *et al.*, where they commented structural relaxation can generate stress for supported thin films which can cause plastic deformation finally leading to the generation of dewetted holes [179]. To study the dewetted hole growth dynamics in our ageing experiments, always primary holes (formed immediately after reaching the dewetting temperature) were considered, as they do not have any thermal history from incubation during dewetting.

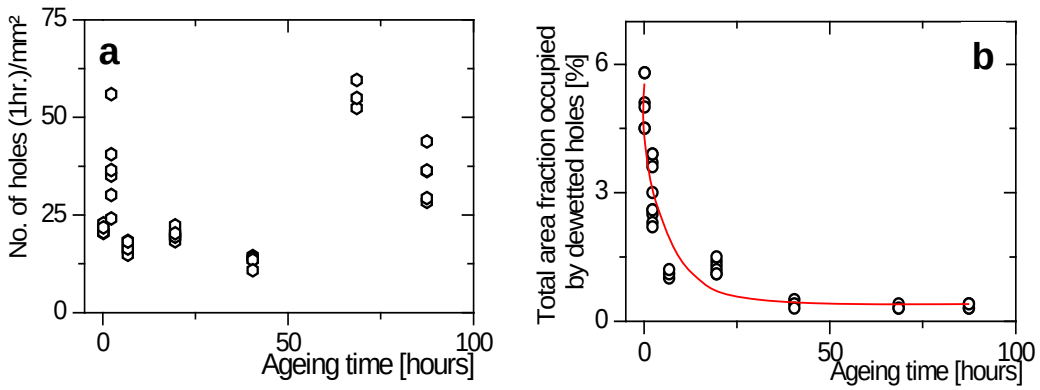

Figure 3.10 – PS films (thickness = ca. 40 nm, M_w = 4060 kg/mol, aged at 90 °C), (a) Variation of total number of dewetted holes per mm^2 (after ca. 1 hr. dewetting at 125 °C) is not showing any particular trend with ageing time. (b) For the same film, variation of dewetted hole area fraction with ageing time, indicates a decrease (in nearly exponential fashion) in dewetted area upon ageing *i.e.* lower rupture probability.

Chapter 4

Influence of Temperature and Substrate on Dewetting and Relaxation of Thin Polymer Films

4.1 Abstract

We studied the dewetting process of thin polystyrene (PS) films on silicon substrates, coated with a thin, irreversibly adsorbed polydimethylsiloxane (PDMS) layer. In the viscoelastic regime close to the glass transition, the temperature and molecular weight dependence of the relaxation time of residual stresses resulting from film preparation by spin-coating can be obtained from the evolution of the shape of the dewetting rim. The presented examples demonstrate that dewetting represents a powerful approach for a sensitive characterization of rheological, frictional and interfacial properties of thin polymer films.

4.2 Introduction

Retraction of a purely Newtonian liquid film from a solid surface and the role of capillary forces are well understood [107]. Nonetheless a similar dewetting phenomenon for highly viscoelastic films where, on the timescale of the experiment, the material cannot flow like a liquid is highly intriguing. Experiments on thin polystyrene (PS) films at temperatures little above the glass transition temperature fall into this category [37, 39, 115, 180]. Under such conditions the polymer can not be treated as a viscous liquid. Thus, interpretation of dewetting results has to account also for the elastic properties of the polymer film. Dewetting

experiments have been proven to be a simple but adequate tool to investigate thin polymer films on various substrates [42,57,81]. Especially the model system of the incompatible polymers polystyrene (PS) on polydimethylsiloxane (PDMS) grafted on a silicon substrate has captivated numerous scientists to explore the dewetting phenomena in polymer thin films. The elasticity of the film is also contributing to the characteristic features of dewetting, like the shape of the rim or the temporal evolution of the hole diameter. In addition, in the course of dewetting, the behaviour of the polystyrene film switch from highly elastic at short times to purely viscous at long times.

In **Section 1.4**, basic concepts of dewetting of thin polymer films were discussed, in terms of mechanisms of formation of holes, dewetting dynamics associated with different dewetting regimes (viscous and viscoelastic) and role of residual stresses. The experimental and theoretical approaches were surveyed in terms of dewetting morphologies (such as hole radius, rim width and rim height). In this chapter, we study the dewetting of polystyrene thin films on a non-wettable substrate to determine the influence of temperature on the relaxation of residual stresses at temperatures above the $T_{g,bulk}$. Further, the possible role of the non-wettable substrate on dewetting dynamics (in terms of interfacial friction) will be discussed. In order to shed some light onto the phenomenon of dewetting of highly elastic films, we followed the process of hole growth in PS films in detail from the very early stages. To emphasize the possible influence of driving forces, and to reduce the resistance from interfacial friction, we have chosen highly non-wettable substrates, as achieved by using PDMS-coated Si-wafers. This PDMS-coating "screened" all heterogeneities of the solid substrates and thus represented an ideally homogeneous non-wettable substrate enabling slippage for the moving PS-film [57].

A characteristic feature of dewetting of high molecular weight viscoelastic fluids (polymers) at temperatures close to T_g is an asymmetric shape of the rim at the early stage of dewetting [39, 42, 57, 102, 109]. The typical shape of an asymmetric rim is shown in **Figure 1.22** (in **Section 1.4**). This asymmetric shape results from the elastic deformation of the film close to the contact line over a characteristic distance controlled by the interfacial friction. For a viscous fluid one would expect equilibration of the Laplace pressure (which is proportional to curvature) within the rim. This would lead to a more symmetric rim shape. The highly asymmetric shape of rim in our high molecular weight viscoelastic films indicates that the polymer is not flowing like a liquid. Initially, for small hole diameters (less than about 1 μm), dissipation of the invested energy originating

e.g. from capillary forces is mainly located within the volume of the film, the removed material (proportional to the dewetted distance (*i.e.*, hole radius, R) will be redistributed within the film over a certain distance Δ_0 which is characterized by film thickness h and frictional properties

$$R << \Delta_0 \sim (h_0\eta/\zeta)^{1/2} \tag{4.1}$$

with ζ being the friction coefficient at the interface and η the viscosity of the film. Under such conditions, no rim is formed next to the circular dewetted zone. However, as the radius of the hole gets larger than Δ_0, this contribution to dissipation becomes smaller compared to friction at the substrate/film interface. As a consequence of such friction, the velocity is damped over the distance Δ_0 within the film. This damping results in the appearance of a highly asymmetric rim, with a steep side reaching a height H next to the three-phase contact line and an approximately exponential decay on the other side, with a decay length Δ_0.

Dewetting experiments were already used to highlight the presence of a characteristic time, τ_W, corresponding to the time during dewetting at which the rim width reaches the maximum value ($W_{\max}$) [42]. This time can be related to the relaxation of residual stresses present in the film and was found to be drastically shorter than the longest relaxation time of the polymer in an equilibrated bulk, the reptation time τ_{REP} [57]. To account for the occurrence of a maximum in the width of the rim in the course of time, and to interpret the effects of sample ageing on this peculiar feature of the viscoelastic thin films, dewetting dynamics, residual stresses in the PS film have been shown to be important [42,81,102,105]. These stresses are supposed to originate from the spin-coating process and can relax (at least partially) during dewetting. For high molecular weight polymers (above ca. 300 kg/mol), residual stresses have been clearly evidenced in various polymer thin film systems [42,56,79,81]. Nonetheless, their relaxation well below the glass temperature is intriguing and its interpretation has been debated for long time [42,181].

While dealing with ageing experiments it was found that $W_{\max}$ is decreasing with ageing time but τ_W remains almost constant [42]. This observation was interpreted as a decrease in residual stresses upon ageing. Ziebert *et al.* reported slow increase in the friction coefficient or, equivalently, a decrease of the slip length can give rise to a maximum in the rim width [105]. Later experiments by Coppee *et al.* partially support this possibility. It is necessary to review all the possibilities which can lead to a maximum in the rim width. Simple scal-

ing arguments have been used by Raphael *et al.* to qualitatively understand the dewetting dynamics [102,182]. The balance of the work done by the driving forces and dissipation via friction can be approximately represented as $|S|\,V \sim \zeta W V^2$ or

$$|S|\,/\zeta \sim WV \tag{4.2}$$

Here V is the velocity of the dewetting front and W is the width of the rim. The driving force acting on the rim is the negative of the spreading parameter S and ζ is the friction coefficient at the polymer-polymer interface. In general, the friction will be non-linear, but for the present simple argument linearity can be considered [182]. Dewetting velocity decreases monotonously during the course of dewetting. So, for W to have a maximum, according to **Equation 4.2**, W has to decrease for some time simultaneously with the monotonously decreasing velocity. This is not possible for **Equation 4.2** if the left-hand side is a constant. An essential condition for a maximum in the rim width is thus that the effective driving force $|S|\,/\zeta$ decreases in the course of time.

There are several possibilities to realize such a decrease: (**a**) Consideration of a residual stress $\sigma(t)$, that is undergoing a relaxation in the course of time, leads to a renormalization of the driving force $|S| \to |S| + h_0\sigma(t)$ (where h_0 is the initial film thickness) [102,105]. As a consequence, upon stress relaxation the driving force decreases. (**b**) Intriguingly, for films of low molecular weight, where relaxation of residual stress could not be evidenced, a maximum in the rim width and its dependence on ageing have also been observed [42,81,182]. Consideration of interface evolution can lead to an increase in the friction coefficient $\zeta \to \zeta(t)$ due to roughening of the film-substrate interface. In addition to the increase in friction, interface roughening can also lead to a decrease of the driving force $|S|$. Very recently, alongwith the dewetting experiments the interface between the two polymer species has been studied by neutron reflectometry. An interdiffusion of the PS-PDMS interface has been found, for samples aged well below the PS bulk glass temperature [181]. (**c**) A third possibility, also associated to minute changes in the interface, is the successive attachment of a few PS chains to the substrate where the PDMS-coverage is low or defective. This process leads to a decrease in the driving force $|S| \to |S| - \nu(t) l f$, where ν is the areal density of such "connector" chains; l is the length they are stretched upon pull-out and f is the pull-out force [183, 184]. Additionally the friction increases due to the connectors, $\zeta \to \zeta + \nu(t)\kappa$ with κ the friction coefficient of connectors [185].

4.3 Experimental

We present experimental results on the dewetting behaviour of thin polymer films on smooth non-wettable silicon substrates. We have used thin polystyrene (PS) films of different molecular weights (M_w = 4060 and 16800 kg/mol, respectively, with a polydispersity index of 1.15 and 1.3 respectively) supported by silicon wafers which were coated with a layer of irreversibly attached PDMS molecules (M_w = 139 kg/mol) [42, 57]. The thickness of the PS films was measured by ellipsometry and was in the range of 40 to 62 nm. All films were obtained by spin-coating dilute polymer solutions (heptane for PDMS and toluene for PS) directly onto the coated substrates. Dewetting of PS films was induced by heating the sample on a hot stage above the glass transition temperature. Isothermal dewetting of the thin polymer films was followed in real time by optical microscopy. The morphology of the rim was also investigated with an Atomic Force Microscope. More details on sample preparation and dewetting experiment can be found in **Chapter 2**. As already shown previously, polystyrene thin films spin-coated onto PDMS-coated silicon wafers are unstable and dewet via the formation of holes. Early stage of dewetting of PS films was followed for times shorter than the reptation time of the polymer. During these stages, viscoelasticity dominated the dewetting behaviour.

4.4 Results and discussions

4.4.1 Influence of temperature on dewetting and relaxation of residual stresses

We follow the growth of dewetted holes at different dewetting temperatures to see the differences in dewetting dynamics and residual stress relaxation. The change in shape of the rim with time can be followed by taking cross-section through holes after different annealing times at different annealing temperatures. As the holes became larger, the building-up of the highly asymmetric rim could be followed. As can be seen in **Figure 4.1 a**, during the early stages of rim build-up, the width of the rim, W, increased in a logarithmic fashion in time, up to a time τ_W when W reached a maximum ($W_{\max}$). At times larger than τ_W, the width of the rim either remained constant or decreased. τ_W can also be related to a transition of the highly asymmetric rims to more symmetric ones. During this early stage of rim build-up and even at times larger than τ_W, the dewetting veloc-

ity V decreased continuously approximately according to a power law, $V \sim t^{-1}$ (cf. **Figure 4.1 b**). At relatively low temperatures of dewetting holes initially

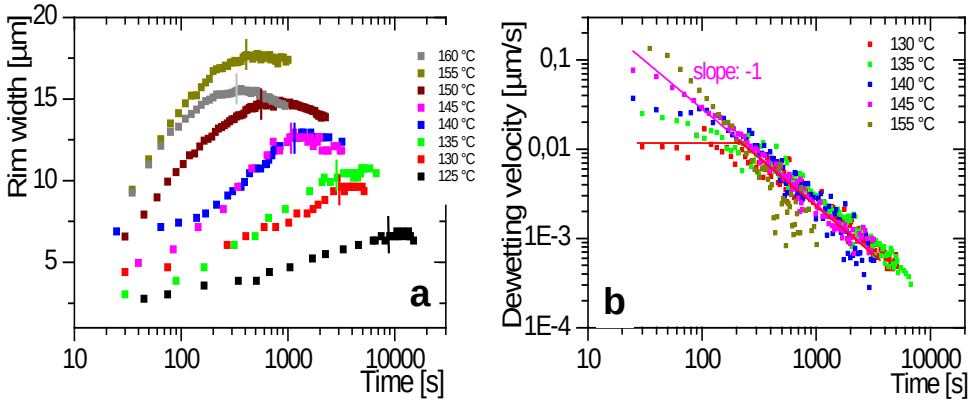

Figure 4.1 – (a) Temporal evolution of the rim width W (b) dewetting velocity V of holes growing in thin polystyrene films ($M_w = 4060$ kg/mol; Film thickness is ca. 40 nm) as a function of dewetting time at various temperatures as indicated in the figure. τ_W is determined by the time when the width of the rim reaches its maximum, as indicated by the vertical lines. Velocity decays like the inverse of time. The pink line corresponds to a $V \sim t^{-1}$ fit at 145 °C. At lower dewetting temperature, hole opening initially takes place at constant velocity and subsequently decays similarly as $V \sim t^{-1}$ (red line is guide to eye).

open up nearly at a constant velocity whereas at higher dewetting temperature the dewetting velocity decayed constantly right from the start. A logarithmic time dependence of R and W, and the corresponding t^{-1} decrease of V, are not expected for a Newtonian liquid. Moreover, our results cover times shorter than the longest relaxation time of equilibrated bulk samples (*i.e.*, the reptation time). Thus, viscoelastic properties of PS certainly influence our dewetting experiments. Effective theoretical models have been developed which take into account residual stresses, interfacial friction (*i.e.*, slippage) and viscoelasticity to explain the dewetting dynamics [102, 105].

In equilibrated bulk samples, the existence of entanglements signifies that the reptation time strongly depends on M_w according to a power law, $\tau_{REP} \sim M_w^{3.4}$. Apart from that, the temperature dependence of the relaxation time follows a non-Arrhenius behaviour when approaching the glass transition temperature. The thermal evolution of relaxation times is usually described by the Vogel–Fulcher–Tamman (VFT) relation, $\tau = \tau_0 \exp(B/(T - T_0)$, with $B = 1170$ K and $T_0 = 343$ K for bulk PS [81]. It also can be explained by the Williams-Landell-Ferry (WLF) equation, which is equivalent to the VFT equation [19]. Interestingly, for the longer polymer, τ_W was remarkably shorter than the τ_{REP} of the bulk polymer [104]. In **Figure 4.2**, we present a comparison

of the values of τ_W for polystyrenes of different chain lengths as a function of temperature. The short polymer (128 kg/mol) approximately followed a VFT behaviour with the values of τ_W and τ_{REP} being almost identical at high temperatures. However, the longer polymers showed significant deviations from such behaviour. At the lowest temperatures, we did not observe any influence of molecular weight. The values of τ_W were almost identical for all polymers studied. At higher temperatures τ_W varied only slightly with temperature, much less than expected from a VFT behaviour [104]. In addition, all values of τ_W were several orders of magnitude lower than τ_{REP} of these long chain polymers in the bulk.

The evolution of τ_W with molecular weight also showed notable deviations from bulk behaviour. For low-M_w, this relaxation was clearly related to the reptation time, τ_{REP}, suggesting that this relaxation process is dominated by the mobility of whole chains [104]. In contrast, for high-$M_w > \sim 300$ kg/mol, very large deviations with respect to bulk reptation times were observed, suggesting that the corresponding relaxation process only requires the motion of a part of such long chains (cf. **Figure 1.25** from ref. [81]). The relaxation time τ_W, as determined from a $W_{\max}$ versus dewetting time plot, became almost independent of the chain length. For the longest chains studied, we found $\tau_W << \tau_{REP}$ by several orders of magnitude. The most notable feature is the almost identical value of τ_W for polymers of very different length. When τ_W values for high molecular weight polymers in our experiments were compared with few earlier reported τ_W values obtained by similar dewetting experiments on nominally similar films, it was found that for our data τ_W was higher by about one decade (cf. **Figure 4.2**) [111, 176]. This change can possibly be interpreted in terms of tiny differences in the PDMS layer. In **Figure 4.2**, we can distinguish two distinct regimes of τ_W depending on the temperature of the dewetting. At low temperatures (T < 110 °C-115 °C), the relaxation time does not depend on the chain length (M_w) and follows qualitatively the VFT dynamics of relaxation. At high temperatures the curves eventually overlap with the VFT behaviour of short chains ($\tau_W \sim \tau_{REP}$ for $M_w < 250$ kg / mol). We interpret τ_W as the time needed to partially relax the non-equilibrated chain conformations, *i.e.*, the time of residual stress relaxation. These conformations have been generated by rapid solvent evaporation in the course of film preparation. In solution the chains were rather diluted and did not have sufficient time to establish the equilibrium state in the film during the process of spin-coating. Most published works found a lower entanglement density in films of thicknesses below ca. 100 nm, by a factor of ~ 2 in comparison to the equilibrated bulk system [53, 55, 84, 85, 112]. Such a departure from equilibrium most likely generates residual stresses.

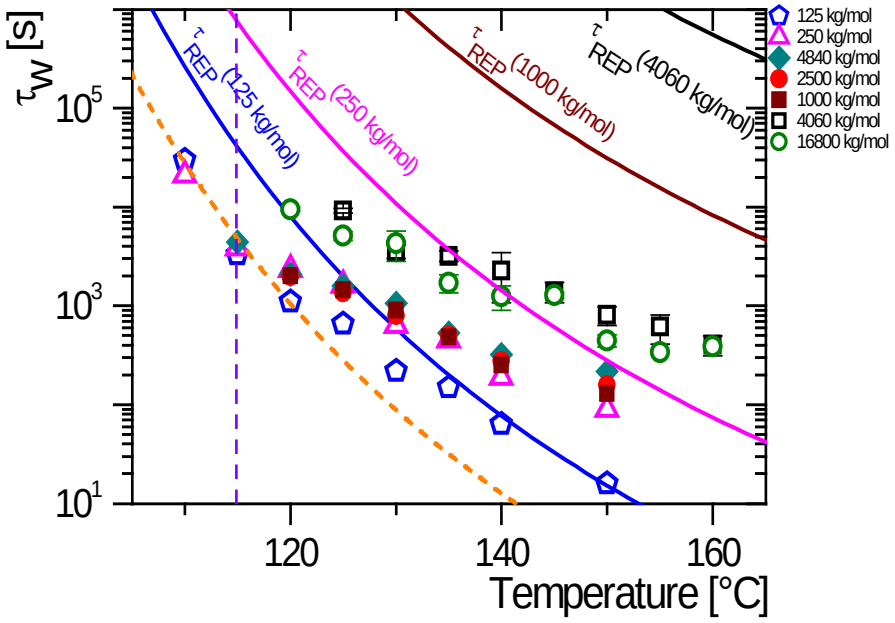

Figure 4.2 – Evolution of the relaxation time τ_W, deduced from the position where the width of the rim reached a maximum value, as a function of dewetting temperature for PS of different molecular weights: 128, 248, 1000, 2500, 4840, 4060 and 16800 kg/mol, together with the evolution of bulk reptation times with temperature according to the VFT law, indicated by solid lines. The dotted orange line represents a qualitative VFT behavior, which is followed by polymer of all lengths at lower temperatures (T < 110 °C -115 °C). The values of τ_W for the M_ws 128, 248, 1000, 2500 and 4840 kg/ mol are taken from the thesis of S. Al Akhrass [111] and M. Hamieh [176]. For all the cases, PS film thickness was set at ca. 40 nm over a ca. 15 nm PDMS layer, except for PS 16800 kg/mol (62 nm PS over 40 nm PDMS).

4.4.2 Influence of PDMS substrate on dewetting and ageing

To know the role of slippage of PS on PDMS, we were interested to see how the PDMS layer thickness affects the process of dewetting. The adsorption of hydroxyl terminated PDMS chains on silicon wafers corresponds to an irreversible adsorption of end-functionalize polymer chains, an intermediate situation with respect to polymer brush and reversibly adsorbed monolayers often termed as 'pseudo-brushes' [138]. Due to a increasing grafting of the chains (a thermally activated process), the thickness of the irreversibly adsorbed PDMS monolayer increases with the adsorption temperature indicating a progressive stretching of the PDMS chains to finally form a dense brush. For irreversibly adsorbed chains the reduced grafting density is given by $\Sigma = \mu\pi R_g^2$, where μ is the grafting density [139, 181], and R_g is the radius of gyration. Radius of gyration for a 139 kg/mol and 77 kg/mol PDMS is $\sim$ 9 nm and $\sim$ 6.5 nm respectively. In our experiment for both the polymers, adsorption for 6 hours at 160 °C led to a dry thickness of PDMS of ca. 15 nm (after washing of excess non-adsorbed PDMS by

heptane). Similarly, adsorption at 200 °C resulted in a PDMS thickness of ca. 40 nm. Increase in PDMS layer thickness with increase in adsorption temperature indicates a stretching in PDMS chains similar to a dense brush morphology. Though, it is surprising to reach a brush thickness which is considerably higher (4-6 times of R_g) than the radius of gyration [181].

In principle, the thickness of the PDMS layer should affect the dewetting dynamics of PS films in two opposite ways: (**i**) Thicker PDMS brushes should dissipate more energy by the deformation of the adsorbed PDMS chains leading thus to slower dewetting velocities and lower size of rim width. (**ii**) If the dewetting dynamics of PS thin films on PDMS coated silicon wafers is dominated by friction of chains at the interface and the viscoelasticity of PS, thicker PDMS layer should yield a higher slippage length. A variation of rim width is a clear indication of a change in the slippage length ($W \sim (h_0 b_s)^{1/2}$), where b_s the slippage length and h_0 the film thickness. Hamieh *et al.* found that the maximum width of the dewetting rim, $W_{\max}$, increased with increasing PDMS layer thickness, which can be interpreted as an increase of the effective, velocity-dependent slippage length [99]. Later, this observation was supported by Coppee *et al.* [181]. We did not find any notably different trend in the size of $W_{\max}$ (and also dewetting velocity) in our nominally identical PS films (M_w = 4060 kg/mol, thickness ca. 40 nm), while dewetted over PDMS layers of either 15 nm or 40 nm thickness (cf. **Figure 4.3**).

Evolution of the maximum rim width ($W_{\max}$) as a function of temperature is shown in **Figure 4.3**. An interesting observation concerns the decrease in the size of rim-width for samples that were nominally identical and differed only in age (at room temperature), in comparison to a relatively fresh film. One can think about some changes in the film which are possible to take place during storing (ageing) at room temperature, leading to a decreased size of rim width. Intriguingly, such observation of decrease in the size of rim width upon dewetting after ageing is pronounced only for PS films over thinner PDMS layer (ca. 15 nm). Storing PS films over thicker PDMS layer (ca. 40 nm) mostly showed an increase in $W_{\max}$ in comparison to a relatively fresh film. These two observations appear puzzling to explain the process of ageing and dewetting for the following reasons. The idea of relaxation of residual stresses in the PS film can explain the decrease in the size of $W_{\max}$ upon storing at room temperature. However, within this interpretation no mechanism exists supporting the increase in $W_{\max}$ upon ageing at room temperature. Based on the consideration of PS-PDMS interface interpenetration, slowing down of the dewetting dynamics during ageing

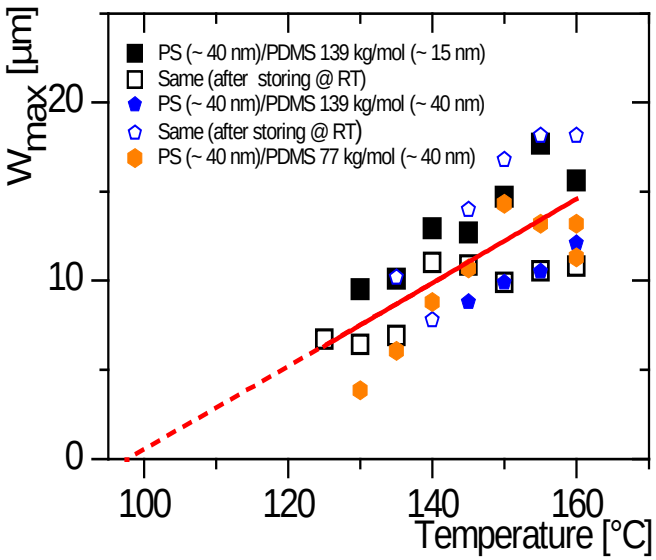

Figure 4.3 – (a) Evolution of rim width maximum, $W_{\max}$, with temperature for PS films on different types of PDMS layer (varied either by thickness or molecular weight mentioned in the plot legend). The linear fit represents variation of $W_{\max}$ with temperature considering data from all of the films. For all, PS of M_w = 4060 kg/mol and film thickness of 42 ± 2 nm were considered.

is directly related to a relaxation of the PS/PDMS interface, *i.e.*, an increase of gradual penetration of PS chains into the PDMS brushes. Though PS is glassy at room temperature, due to the very high mobility of PDMS chains (liquid), this penetration may take place. Apart from that, interdiffusion should be less pronounced for the high-M_w (4060 kg/mol) PS used in this experiment. Eventually, an increase in interfacial interpenetration is similar to a decrease in the inferfacial slip-length [182]. The decrease in slippage length should induces a decrease in maximum rim width ($b_s \sim W^2$).

Coppee *et al.* found ageing is much more pronounced for the thinnest PDMS layers ("loops and tails" morphology), whereas very long ageing times (more than 2 days) are required to observe a significant decrease of the rim width for the thicker PDMS brushes [181]. The thickness of the PDMS monolayers thus affects unexpectedly the dynamics of ageing. Our experiment dealt with ca. 40 nm thick PDMS layers, which are ca. 4 times thicker in comparison to what was used by Coppee *et al.* We may say such thick PDMS layer is not contributing to any ageing effects in the present experiment. Importantly, such thick PDMS layer possibly did not contribute to higher slip length as well, as any notable change in the $W_{\max}$ value was not observed, in comparison to thinner PDMS layers (cf. **Figure 4.3**). Thinner PDMS layers showed ageing effect mostly indicated by a decrease in rim width (cf. **Figure 4.3**).

Interestingly, extrapolation of linear fit for the $W_{\max}$-T plot to $W_{\max} = 0$ for all the PS films ($M_w = 4060$ kg/mol , thickness ca. 40 nm) lead to intersect the temperature axis at about 100 ± 2 °C, which is close to the glass transition temperature of bulk PS (cf. **Figure 4.3**).

It was previously shown that the characteristic stress relaxation time (τ_W) is independent of the level of residual stresses induced by the spin-coating process [42]. One may also ask the question if differences in the frictional properties at the film/substrate interface have an effect on the way the residual stresses relax in the PS film. We can get the answer by determining the characteristic time, τ_W for different pairs of PS-PDMS film. In **Figure 4.4**, taking into account error bars (found from several repeated measurements on nominally similar films), one may conclude that the changes of τ_W are not very large, especially when dewetting was performed at temperature higher than 140 °C.

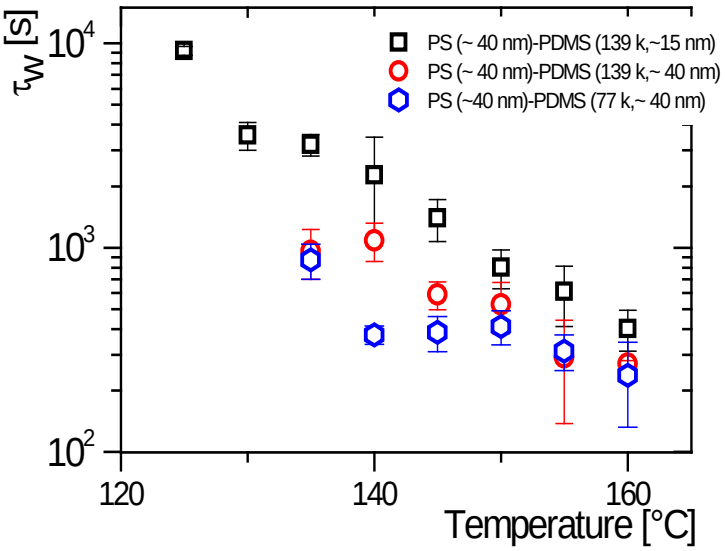

Figure 4.4 – Evolution of the relaxation time τ_W as a function of dewetting temperature for PS films ($M_w = 4060$ kg/mol and thickness is 42 ± 2 nm) on different PDMS layers adsorbed on Si-wafer.

Thickness variations of the PDMS layers did not create any clear trends for τ_W. This approximate constancy of τ_W may reflect the huge difference in the glass-transition temperatures of the PDMS and the PS molecules. Of course, if the PS chains would be adsorbed onto the substrate, their relaxation properties would have changed. However, due to the strong incompatibility between PDMS and PS (this is a major reason why this pair of polymers was chosen in first place) and the corresponding interfacial tension between them, the PDMS substrate can be considered as a highly non-wettable and non-penetrable substrate for PS [99]. Consequently, this consideration is also outpacing the possibility of any kind of

PS-PDMS interpenetration at the interface. Therefore, the substrate should not significantly affect the relaxation processes (relaxation of residual stresses) of PS chains.

4.5 Conclusions

We have shown that, independent of molecular weight relaxation times of residual stresses (τ_W) are comparable for high molar mass polystyrene thin films, measured through dewetting at different temperatures. They are all smaller than the estimated reptation times for bulk polymer at that temperature. For low-M_w, this relaxation was rather close to the reptation time (τ_{REP}), suggesting that this relaxation process is dominated by the mobility of whole chains. In contrast, for high-$M_w > \sim 300$ kg/mol, very large deviations with respect to bulk reptation times were observed, suggesting that the corresponding relaxation process only requires segmental motion of such long chains. Above results clearly demonstrate that dewetting can be considered as a "nano-rheology" experiment which allows to look into the structure and properties of out-of-equilibrium PS thin films. We may thus consider dewetting as a rheological "probe" to study viscoelastic properties of nanoscopic polymer films [57,104]. In combination with few earlier reports, we were abled to enlighten the influence of the PDMS substrate (in terms of dissipation, slipping and possibility of polymer-polymer chain interpenetration between the PDMS coated silicon wafer and the PS film) on the dewetting process. Using thick (ca. 40 nm) PDMS layers we did not find any notable difference either in dewetting dynamics (dewetting velocity or size of rim width) or in relaxation time (τ_W), in comparison to a less thick PDMS layer (ca. 15 nm). Keeping constant the parameters that characterize the dewetting film (*i.e.*, its thickness and mechanical properties), systematic studies on variously coated substrates will acutely allow one to accomplish the full potential of dewetting for studies of interfacial properties such as friction and adhesion at polymer–polymer interfaces [99].

Chapter 5

Cracking and Crazing in Thin Glassy Polymer Films by Physical Ageing

5.1 Abstract

In this chapter we show that physical ageing at elevated temperatures but below $T_{g,bulk}$ is capable to induce stresses resulting in cracking in ultrathin glassy polymer films. Relaxation of residual stresses resulting from the preparation of these films is also taking place. Systematic studies of crack growth as a function of physical ageing were performed. We observed cracking after ageing (at a temperature close to the $T_{g,bulk}$) and cooling the films down to room temperature. AFM inspection for long chain polymers showed nano/microstructures within the cracks consisting of voids and fibrils, indicating craze. Short chain polymers (comparable to the entanglement length) do not show such craze nano/ microstructures, rather formed simple cracks. Cracks or crazes appear throughout the whole film finally leading to an interconnected network, similar to crack patterns in dried mud. For high molecular weight polystyrene, a systematic study of craze propagation velocity showed a progressive increase with increasing ageing time whereas for the same films the dewetting velocity decreased with ageing. While increase in craze propagation velocity indicates an increase in total stress inside the film the decrease of dewetting velocity is a signature of relaxation of residual stress.

5.2 Introductory discussions

A considerable amount of stresses can be generated inside nanometer thick polymer films during preparation, known as residual stresses [78–80]. The origin of these stresses can be quickly recalled: film formation by solvent evaporation steadily increases the polymer concentration, thereby raising the glass transition temperature (T_g) of the solution. As soon as T_g reaches the ambient temperature (at solvent volume fractions of ca. 0.14–0.2) the polymer vitrifies, suppressing further equilibration of the chains by diffusion. This leads to frozen-in polymer chain conformations. Further evaporation of the remaining solvent induces residual stresses in the film.

In-plane stresses can have a substantial impact on the stability of thin polymer films. Such as, the possibility of deformation-induced crazing/cracking in polymer thin films during the process of spin-coating (discussed in **Appendix-II**), commencement of rupturing due to the plastic yield. Reiter and de Gennes suggested that such plastic yield is more probable to occur close but below the $T_{g,bulk}$, such as 90 °C. Moreover, the larger the stored stress inside a film, the more easily plastic yield can take place [76]. Highly squeezed polymer chains confined in the thin film dimensions may yield high stress values. Rowland *et al.* through their flat-punch induced deformation experiment on confined/squeezed thin molten films showed that when the film thickness was smaller than the radius of gyration, both the resistance to small scale elastic deformation (contact modulus) and the stress required to induce large-scale plastic deformation (forming stress) are strongly reduced [77]. In other words, residual stresses inside the thin polymer film should have a certain impact on its deformation. However, though several studies on the amount of residual stresses were reported with the anticipated possibilities for deformation or failure, there was not any clear interpretation on the amount of critical stress which can cause failure (cracks or crazes) in such nanometer thick polymer films.

To anticipate the possibilities of deformations and its failures one should know the amount of residual stresses present inside a thin polymer film. Despite their importance, stresses in thin films are not easy to measure and can often only be deduced indirectly. Yang *et al.* determined the molecular recoiling stress in polymer thin films from the surface contour around the incipient dewetted holes by AFM [78]. The recoiling stress was found to be within 10 MPa, increasing rapidly with molecular weight while decreasing with increasing film thickness. This is indicative of large amounts of residual stresses due to squeezing long poly-

mer chains inside the confined thin film. Thomas *et al.* did direct measurement of residual stresses inside a thin spin-coated film utilizing a modified version of the conventional beam or cantilever curvature measurement technique [80]. Spun-cast film of high molecular weight PS showed surprisingly high residual stress of ca. 135 MPa. Chung *et al.* used a strain induced surface wrinkling method to determine the residual stress inside a spin-coated PS thin film [79]. Residual stresses of ca. 30 MPa were found, deduced from the measured wavelength of the wrinkle patterns. Recently they combined the wrinkling experiment with cracking [186]. For PS film over elastomeric PDMS substrate, at relatively low strains, a threshold stress is reached where a periodic wrinkling pattern appears with the ridges of the wrinkles oriented parallel to the applied strain direction, but the oscillation runs perpendicular to the strain having a well-defined wavelength. This wavelength is related to the elastic modulus or stiffness of the film. At higher strains, the film starts to crack with their long axis perpendicular to the applied strain. For glassy PS films they found that applied critical tensile strength for cracking is ca. 20 MPa [186].

Thermal history certainly has some impacts on the content of residual stresses in thin films. Both of Thomas *et al.* and Chung *et al.* have shown that the residual stress decreases upon thermal annealing above the $T_{g,bulk}$ of the polymer [79, 80]. Reiter *et al.* showed physical ageing even far below the $T_{g,bulk}$ of the polymer can lead to a decrease in the amount of residual stress [42]. Considering a similar experimental protocol of ageing at elevated temperatures close to the $T_{g,bulk}$ of the polymer (but essentially below it) we found the formation of cracks/crazes in our thin polystyrene films. Though the same film showed a decrease in residual stresses indicated through dewetting studies, formation of cracks invokes the possibility of stress accumulation either by substrate-film thermal mismatch or by more complex way during stress relaxation. The present chapter tries to answer the possible role of ageing history on the process of cracking and crazing. Apart from that, the morphological features of cracking and crazing patterns were also explored to find a possible explanation for the failure process.

5.3 Experimental

For the corresponding experimental studies we used thin polystyrene (PS) films with varying thicknesses ranging from 40 nm-300 nm on smooth Si (100) substrates coated with thin (ca. 15 nm thickness) non-wettable polydimethylsiloxane

(PDMS layers) [42]. Here the PDMS layer is acting as an apolar liquid layer enabling slippage and facilitating the crack propagation and dewetting of PS under well-defined experimental conditions. Thermal treatments were done according to the scheme of **Figure 2.6**. Cracking and crazing were found when a film has been aged at a temperature which is close but below the $T_{g,bulk}$ of the polymer and subsequently cooled down to room temperature. Finally, to judge the extent of residual stresses present inside those already aged and cracked films, dewetting studies were performed at 125 °C and the temporal evolution of hole growth was followed. For the present series of experiments ageing was always performed at 90 °C. We used polystyrene of various molecular weights: 52 kg/mol, 120 kg/mol, 532 kg/mol, 4060 kg/mol and 16800 kg/mol. Polydispersity index is less than 1.3 for all. Ageing was always performed either inside a vacuum oven (equipped with an oil-free pump) or inside a closed Linkam hot stage (N_2 gas purged).

5.4 Results and discussions

Crazes/Cracks were only forming in a film which was aged below but close to $T_{g,bulk}$. We found that the lower limit of ageing temperature for crazing (in long chain PS) is $T_a = T_{g,bulk} - (20 \pm 5)$ °C and for cracking (in short chain PS) $T_a = T_{g,bulk} - (30 \pm 5)$ °C. Annealing little above the glass transition temperature (*e.g.* at 110 °C and 115 °C for 3 hours followed by storing the sample at room temperature for 3 hours) never resulted in crazing (in long chain PS). We note that for short chain PS dewetting may start in this temperature region (110 °C-115 °C). Once dewetting started crack formation was no more observed. For long chain PS there might be some role of residual stresses on crazing. Such residual stresses should decrease more during annealing in comparison to ageing.

5.4.1 Cracking in low molecular weight (short chain) PS films

In a first attempt, we used PS films ranging from ca. 40-150 nm thickness and of molecular weight 52 kg/mol. For all the samples we used an ageing temperature of 90 °C for 24 hours. The process of crack formation and propagation was monitored under an optical microscope. For all films, crack growth started close to 55 °C, during cooling the film down from the ageing temperature 90 °C towards the room temperature. We do rapid cooling of the sample, just by taking out the sample from the oven or switching off the hot stage (here, within the first

minute, the temperature decreased by 32-33 °C). Inspection by AFM clearly indicated cracks across the whole film thickness.

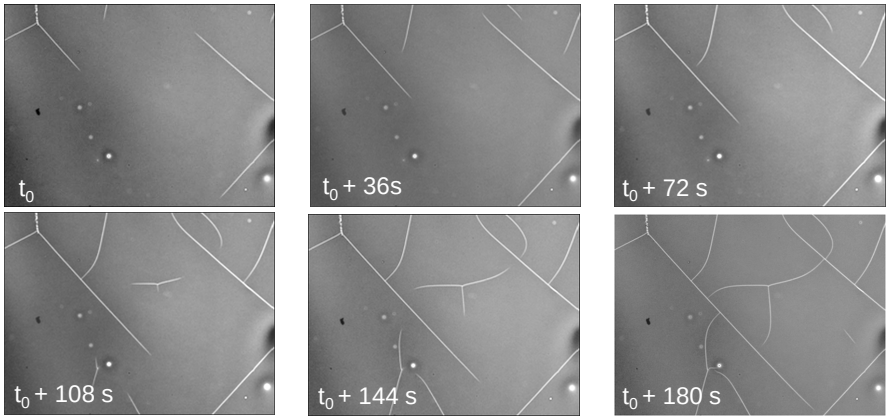

Figure 5.1 – Optical micrographs (size of each 1430 x 1063 µm^2) showing typical way of hierarchical crack growth in a film during/after cooling it down to room temperature from the ageing temperature (PS, M_w = 52 kg/mol, thickness = 55 nm, aged at 90 °C for 24 hours).

The fragmentation process was hierarchical: after a pattern was formed by primary cracks, secondary cracks break the domains into smaller ones, and so on. Growing cracks in a ca. 55 nm thick film was followed under an optical microscope (cf. **Figure 5.1**). The crack propagation velocity was fast (ca. 7-8 µm/s) and occurs at constant velocity until two cracks came close to each other and connected almost at right angle. A crack relieves the stress in the perpendicular direction but not in the parallel one, so that a new crack can release more energy by running into an existing crack at right angles [187]. Different cracks in the same film propagate with nearly same speed, which decreases only when two cracks come close enough before connecting (cf. **Figure 5.2 a-b**). Possibly, as the crack tips approach each other, the cracks must begin to deviate from their former course due to mode mixing [188]. The way cracks were generated throughout the whole film leading to a hierarchically grown network indicated that there was not any single origin (nucleation point). Besides, uniaxial stress is not responsible for such cracking; rather it is biaxial or of more complex origin.

Following the same experimental protocol with various film thicknesses revealed that, in general, an increase in film thickness led to a higher width of the cracks with larger area of fragmented domains (cf. **Figure 5.3 a-b**). Though the size of the areas enclosed by cracks in a film are highly polydisperse, in general an increase in their average size was observed with increasing thickness. A clear increase in crack width was found with increasing film thicknesses up to

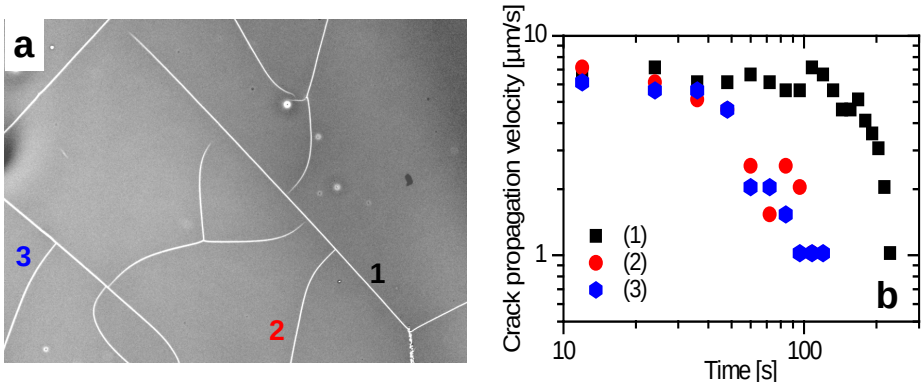

Figure 5.2 – Optical micrograph (size: 1430 x 1063 µm^2) showing crack propagation for different cracks in the same film (PS, M_w = 52 kg/mol, thickness = 55 nm, aged at 90 °C for 24 hours). (b) Start up propagation velocities for different cracks are comparable and decrease when two cracks come close to each other until they connect.

ca.100 nm of film thickness (cf. **Figure 5.4**). This is a common observation for cracking, occurring in several common desiccation and thermal mismatch cracking systems, such as cracking in thin slurry of corn-starch, polymer microspheres and even mud [189–192]. We always considered the width of only those cracks which were not generated at late stages of cracking. Crack widths were considered in the mid-region of a long crack far enough from the crack-tip. Care was taken to exclude cracks in areas perturbed by flaws, like scratches or dirt particles.

The dependence of crack width with film thickness might be simply explained by the model of Hillerborg *et al.* where a crack was assumed to propagate when the stress (σ) at the crack tip reaches the tensile strength in the consideration of Linear elastic fracture mechanics after Griffith, cf. **Section 1.5** [193]. When the crack opens, the stress decreases with increasing crack width (w). As there is a stress to overcome in opening a crack, energy is dissipated by opening a unit area of crack surface and widening it. So, the amount of energy absorbed in widening a crack per unit area can be written as $G_c = \int \sigma dw$. Again, from the elastic fracture mechanics, the fracture toughness or fracture energy (work per fractured surface area) can be represented as: $G_c = Z\frac{\sigma^2 h}{\bar{E_f}}$ where, $\bar{E_f} = \frac{E_f}{1-\nu_f^2}$, h is the film thickness and Z is a constant whose value is in between 1 to 2. E_f and ν_f are representing the elastic modulus and Poisson ratio of the film respectively [194]. So, one can expect a higher crack width and a higher fracture toughness for thicker films. While many of these concepts of linear elastic fracture mechanics have been applied to the study of bulk polymers and polymer films of the order of micron (or higher) thicknesses, there are very few reports on successful applications of these concepts to nanometer thick films [195]. Interestingly, an extrapolation of the linear fit of crack width as a function of film thickness in

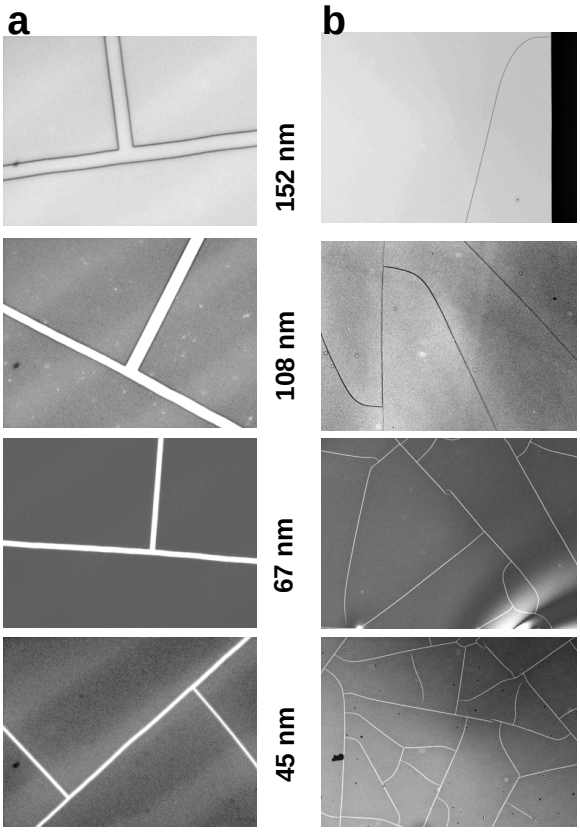

Figure 5.3 – Optical micrographs showing cracking patterns formed in films (PS, M_w = 52 kg/mol, aged at 90 °C for 24 hours) of different thicknesses. (a) The left column is showing the increase in crack width upon increase in film thickness. Size of each image: 65 x 50 µm^2. (b) The right column is showing the increase in the size of the domains enclosed by cracks upon increase in film thickness. Size of each image: 1430 x 1063 µm^2.

our experiment intersects the film thickness axis around 30 nm, coinciding with the threshold thickness below which our experiments never resulted in any crack formation, irrespective of molecular weights (cf. **Figure 5.4**). No obvious thickness dependence on crack propagation velocities was found in the film thickness range investigated in these studies.

In typical crack formations of a layer/film on a solid substrate, the layer hardens and/or weakens in time; it tends to contract but is resisted by the friction from ssubstrate. To explain our experimental findings, a condition might be necessary where biaxial stress is combined with a slipping at the interface. This situation might be described through a proper consideration of the spring-block model [189] or the shear-lag model [196]. Our experimental observations are in good agreement with the theoretical analysis and simulations of a discrete spring-block model (each pair of neighbouring blocks are connected by a bundle of springs, instead of a single spring) as described by Leung and Neda [190]. This

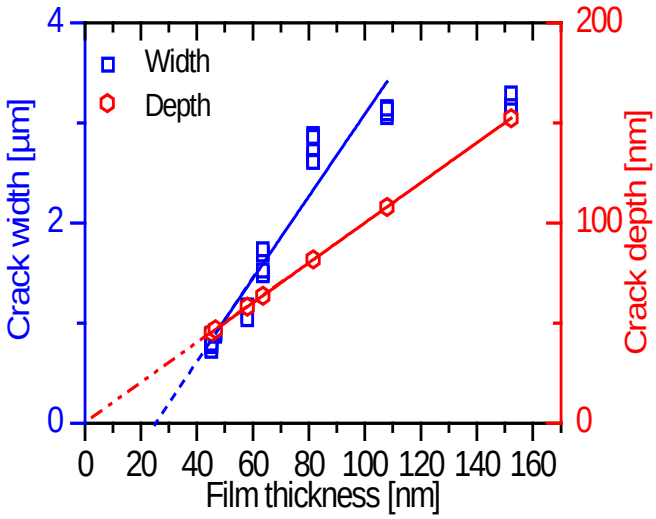

Figure 5.4 – Variation of crack width and depth with film thickness in PS films (M_w = 52 kg/mol, aged at 90 °C for 24 hours). Crack depth varies with the film thickness with a slope of 1, indicating crack goes throughout the whole film thickness.

model describes the nucleation and propagation of cracks in a layer in contact with a substrate involving following events: (i) the system contracts by slipping; the total number of slipping events grows in time. (ii) There are slippings and bond breakings; the system is progressively damaged, then fragmented, while contraction continues. (iii) Bond breaking saturates, fragmentation stops. In particular, consistent with our experimental observations and common observations on drying layers (mud, corn-starch slurry, and colloidal solution), the simulated fragmented areas were found to increase with the increase of layer thickness scaled as: fragmented area $\sim$ square of film thickness. This model also points out an increasing crack width with increasing film thickness. Moreover, this model indicates the existence of a threshold film thickness below which it will certainly not crack. We also found similar observation in our experiments.

Well before this report on spring-block model [190], Hornig *et al.* explained a scalar model consist of array of springs making the coating and its fragmentation covering a bulk material elastically [197]. The coating was considered to break under a quasistatical, slowly increasing strain, induced, *e.g.*, by temperature changes, by desiccation, or by mechanical deformations. They found that the mean fragment size decays through a power-law dependence on the strain; the exponent of the power law is related to the amount of strain and strength of disorder of the coating. Their finite-element anlaysis indicated a correlation length below which the local strain is almost uniform inside a fragmented domain [197]. Eventually, at a distance comparable to correlation length two separately originated cracks can feel each other and follow a different course

of propagation, possibly due to mode-mixing of cracking. A shear-lag consideration in the above model accounts for the non-linear coupling between film and substrate, depending upon film-substrate relative shear displacement and interfacial shear modulus. Recently, the classical shear-lag model was extended to derive an analytical solution of the biaxial coating stress during uniaxial tensile testing condition [196]. The model was in agreement with experimental results concerning 50-200 nm thick metal films over polyimide substrates, showing an increase of the mean crack fragment size with increasing film thickness. This was explained in terms of correlation length or stress transfer length [196]. This length increases with increasing film thickness and/or elastic modulus of the film whereas decreases upon increasing interfacial shear moddulus. Though this result is partially in agreement with our experimental observations, differences in the cracking patterns and straining condition cannot be fully exist for our experiment.

Cracking during cooling down the film towards room temperature essentially invokes the possibility of failure due to the thermal mismatch between the expansion coefficients of the substrate ($\alpha_s \sim 10$ x 10^{-6}/ °C) and the PS film ($\alpha_f \sim 60$ x 10^{-6}/ °C). During cooling from ageing temperature ($T_a = 90$ °C) to room temperature ($T_{RT} = 25$ °C), thermal stress (σ_{th}) is approximately

$$\sigma_{th} = \frac{E_f}{1-\nu_f^2}(\alpha_f - \alpha_s)(T_{RT} - T_a) \tag{5.1}$$

This value corresponds to $\sim$ 14 MPa (considering $E_f = 3.7$ GPa and $\nu_f = 0.33$) [79]. To verify the role of thermal stress, we did a test experiment on a ca. 64 nm thick film of 52 kg/mol PS with different cooling rate from the ageing temperature 90 °C, while the duration of ageing was kept same. We found that the crack width in the rapidly cooled film was higher than the slowly cooled film (Cooling rate: 10 °C/min up to 80 °C, followed by 5 °C/min up to 75 °C, followed by 0.01 °C/min to room temperature. Between each temperature cycle, the sample was held for 30 minutes at that temperature). A histogram of crack width indicates the higher width of the cracks for the rapidly cooled film (cf. **Figure 5.5**). Total length of cracks formed per unit area also decreased for a film which is slowly cooled. No notable difference in crack growth velocity was found for films cooled at different cooling.

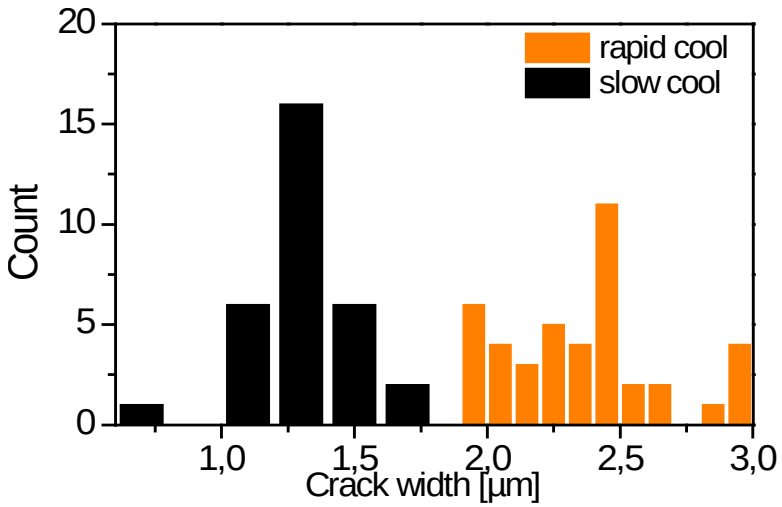

Figure 5.5 – Histogram shows higher crack width for a rapidly cooled film (PS, M_w = 52 kg/mol, thickness = 64 nm, aged at 90 °C for 24 hours) in comparison to a nominally similar film which was cooled slowly in a controlled way.

5.4.2 Crazing in high molecular weight (long chain) PS films

Morphology:

Further experiments were performed on high molecular weight PS (120 kg/mol to 16800 kg/mol) thin films, for thicknesses ranging from ca. 40 nm to 350 nm. Thermal treatments were done in a similar fashion as used for the low molecular weight (52 kg/mol) PS films, *i.e.*, ageing at 90 °C for 24 hours inside a vacuum oven, followed by rapid cooling towards room temperature. One can see growth of crack-like failures under the optical microscope; starting from ca. 37 ± 2 °C. These cracks finally led to an interconnected pattern when cooling to room temperature (cf. **Figure 5.6 a-b**). Detailed AFM inspections inside such crack-like

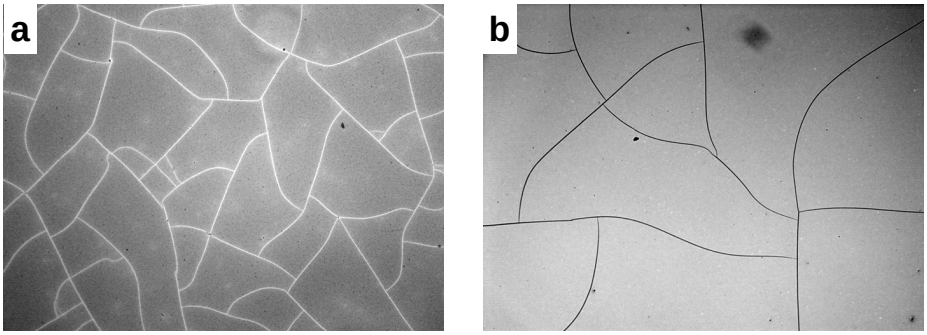

Figure 5.6 – Optical micrographs showing typical craze patterns observed. Size of each image: 1430 x 1063 µm^2. PS films (M_w = 4060 kg/mol) were aged at 90°C for 24 hours (a) thickness = 42 ± 2 nm (b) thickness = 300 nm. The micrographs were taken several days after quenching the sample to room temperature, to let the crazes have sufficient time to develop.

structures showed nano/micro structures consisting of voids and fibrils indicative of crazing. Crazes which were generated later during the course of craze formation had a smaller width as shown in the AFM image of a craze junction (cf. **Figure 5.7**). **Figure 5.8 a** shows the microstructures inside a craze in a ca. 40

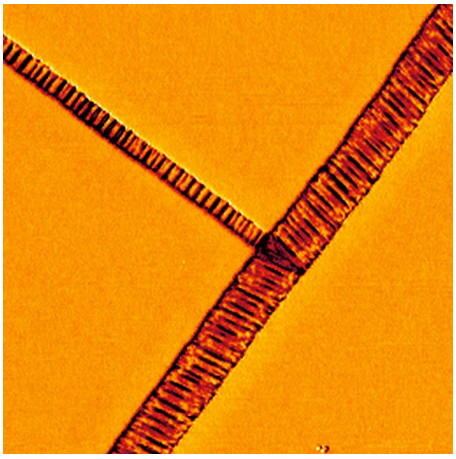

Figure 5.7 – Typical AFM micrograph (phase image, size: 2.5 x 2.5 µm^2) of a craze junction in a PS film (M_w = 4060 kg/mol, thickness = 42 ± 2 nm, aged at 90 °C for 40 days).

nm thin film of PS 4060 k, which was aged at 90 °C for 24 hours and kept several hours at room temperature after quenching. Craze tips can also be isolated (cf. **Figure 5.8 b**). A closer look on the AFM phase images indicates clearly visible stripes/wrinkles parallel to the direction of fibrils (cf. **Figure 5.8 a-b**). This is also the direction of the possibly occurring tensile/compressive type of stresses indicating the formation of cracks or crazes perpendicular to it. These stripes in the AFM phase images seem to indicate a localized deformation (stiffening) which might be occuring due to strain-hardening [34]. One may assume that striped deformations might be signifying a possible shrinking (and wrinkling) of the polymer layer. But we never found any clear wrinkles/stripes in the corresponding height images.

The role of entanglements for the stability (integrity) of craze fibrils is clear in our experiments. We never found stable crazes in PS film of molecular weight 52 kg/mol and below it. This is in agreement with several experimental and theoretical findings. First Kramer *et al.* showed that long craze fibrils (and therefore crazes themselves) are not stable below a critical molecular weight $M_c \sim 2M_e$, where M_e is the entanglement molecular weight [198]. Later they compiled values of G_c for PS and PMMA as a function of polymer molecular weight [128]. None of the polymers showed large fracture energy when molecular weight was less than $2M_e$. Further attempts to correlate fracture toughness, crazing stress and chain entanglement were reported in terms of theoretical arguments [125] and

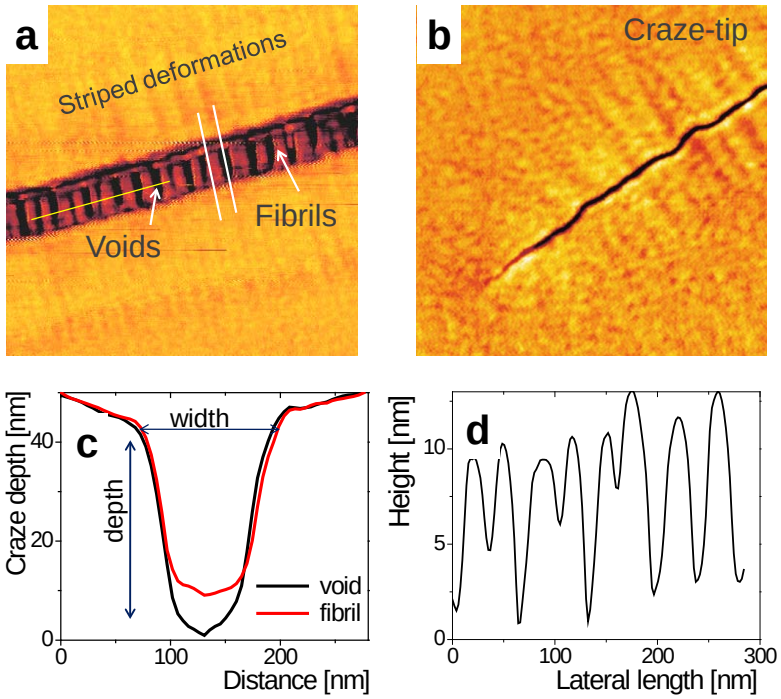

Figure 5.8 – AFM micrographs (phase image, size: 700 x 700 nm^2 each) showing (a) typical craze microstructures consisting of voids and fibrils in a PS film (M_w = 4060 kg/mol, thickness = 42 ± 2 nm, aged at 90 °C for 24 hours). (b) Craze tip in the same film. Striped localized deformation perpendicular to the direction of craze fibril is visible. The micrographs were taken several hours after quenching the sample to room temperature. (c) Height profiles across a craze corresponding to a void and a fibril as indicated by white lines in (a). (d) Height profile corresponding to the yellow line in (a).

molecular dynamics simulations [126, 127]. Interestingly, the simulation results by Rottler and Robbins agreed with several experimental observations in greater detail. In their simulations the fracture energy rises rapidly as M_w rises above $2M_e$ and then saturates around $|8-10|\,M_e$ [126]. If we consider the case of PS, the fracture energy should rise when changing molecular weight from ca. 35 kg/mol and should reach a maximum for ca. 140-175 kg/mol. In our experiments we found lower fracture toughness in terms of unstable craze up to $\sim 3M_e$ (52 kg/mol), whereas starting from $\sim 7M_e$ (120 kg/mol) stable craze fibrils were found. Our experimental results are in good agreement with all of these literature reports.

An intriguing issue concerning craze depth is to know whether the craze fibrils can fill the entire film thickness. In our present experiments, there is a limitation for the AFM tip (tip radius = 8 nm) which cannot fully penetrate inside the crazed film, especially in between highly superimposed voids and fibrils. Multiple layers of closely spaced fibrils are mostly occurring in thick films due to its relatively higher plastic constraint along the film thickness direction, in com-

parison to thin films [199]. Craze depth and width both increase with increasing distance from the craze-tip [199, 200]. In our experiments mature crazes far from the craze tip (at the mid-section of the crazed line) were considered. As the duration of ageing at elevated temperatures has a role on the craze morphology (elaborated in the next section), we always keep the same ageing duration (24 hours) for all the experiments presented in this subsection.

Craze depths in our experiment were compared through varying tapping force (set-point ratio) during AFM measurement in tapping mode. Increase in craze depth was found with increasing tapping force. AFM-tip was able to penetrate through the whole film thickness; unless the distance between fibrils did not allow AFM tip to reach the substrate (AFM tip radius is 8 nm). This observation seems to be in disagreement with earlier observation by Donald *et al.* Through quantitative stereoanalysis of TEM images (by tilting the sample, two micrographs of the same area of the craze were taken), they found that fibrils did not fill the entire film thickness [199]. Prior AFM studies on thin film crazing indicated that the craze depth linearly increased with film thickness until the craze width reached a critical value, dependent upon film thickness [121, 200]. Both of the reports showed that for a mature craze in a thin film the ratio of craze depth to film thickness saturates at a value of approximately 0.35. One of the major differences for all those reported craze microstructures in comparison to our present study is that all of them are formed in free standing films held on a TEM-grid in presence of external mechanical straining.

For thick films (above ca. 150 nm), crazes appeared not to cut through the whole film. We relate this to the limitations of the AFM-tip to penetrate through a dense stack of highly superposed fibrils. Interestingly, a huge increase in craze depth and craze width was found upon storing the crazed films for extremely long time (months) at ambient conditions. It might be due to two possibilities: (i) The crazing process keeps on going for a long duration by growing in width and depth. (ii) Already formed crazes can preferentially absorb moisture from the ambient air, though water is not a good plasticizing agent for PS, it may nonetheless lead to a decrease in fracture toughness of the polymer [201].

Possibly, in our experiments the craze formation started to occur from the film surface, in agreement with recent ideas of craze growth [121,200]. According to these studies, crazing in polymer thin films takes place in three directions; apart from growing in length and width it also propagates in the thickness direction up to a certain depth. This is described by Yang *et al.* as micronecking,

operative during crazing [121]. Formation of crazes at the film surface is favoured in two ways: (i) the fracture of the polymer rich surface 'crust' layer which has solidified during the spin-coating of the film. Such 'crust' can be considered as a highly non-equilibrated, stressed, and poorly entangled surface layer [173]. Crazing/cracking is more probable in such a stressed layer. (ii) There should be a higher probability of disentanglement-dependent crazing for ultrathin films. The idea of enhanced mobility at the thin polymer film free surface is supposed to give an additional mobility of the chains at the active zone during crazing [123]. Though disentanglement-dependent crazing of long chain bulk polymers in the glassy state has not yet been clearly supported experimentally, the case of ultrathin films when aged close to the $T_{g,bulk}$ may give rise to that possibility. Finally, one can anticipate a general process of cracking and crazing in such ultrathin films starting from the film surface and propagation towards the interior (micronecking) [121].

For the moment we assume that craze microstructures in thin films are essentially different than those in bulk. It has been postulated that for films below a critical thickness, plastic constraints along the film direction is eliminated or at least largely reduced. Krupenkin *et al.* predicted that crazing in film thicknesses above ca. 100 nm leads to a network of fine fibrils on the order of 10 nm, whereas for film thicknesses below ca. 100 nm fibrils with occasional holes form [202]. Donald *et al.* reported a critical thickness of 150 nm below which larger diameters of fibrils can be noted with higher fibril volume fractions resembling 'perforated sheets' [199]. Above that thickness they mostly found cylindrical fibrils with ca. 6 nm diameter. Besides these experimental findings, the fibril size was also theoretically explained [199, 202]. In accordance with earlier reports, the present experiments also indicated larger sizes of fibrils and voids with smaller craze width for thinner films (cf. **Figure 5.9 a-b**). In general, larger craze widths and smaller sizes of craze fibrils/voids are indicative of higher amounts of crazing stress, *i.e.*, the stress needed and responsible to draw fibrils out of the dense regions adjacent to the craze to initiate crazing. Eventually, the fracture toughness of an amorphous solid polymer, G_c is primarily limited by the craze width, w, which depends on the maximum crazing stress, $S_c(\max)$, that the craze fibril can withstand; $S_c(max)/S_c \sim (w/D_0)^{1/2}$, where S_c is the crazing stress, and w, D_0 represent the craze width and the fibril/void diameter respectively [126].

Craze growth dynamics:

Further on, the process of crack/craze propagation was monitored under an optical microscope. Hierarchical growth of cracks/crazes was found until they were all

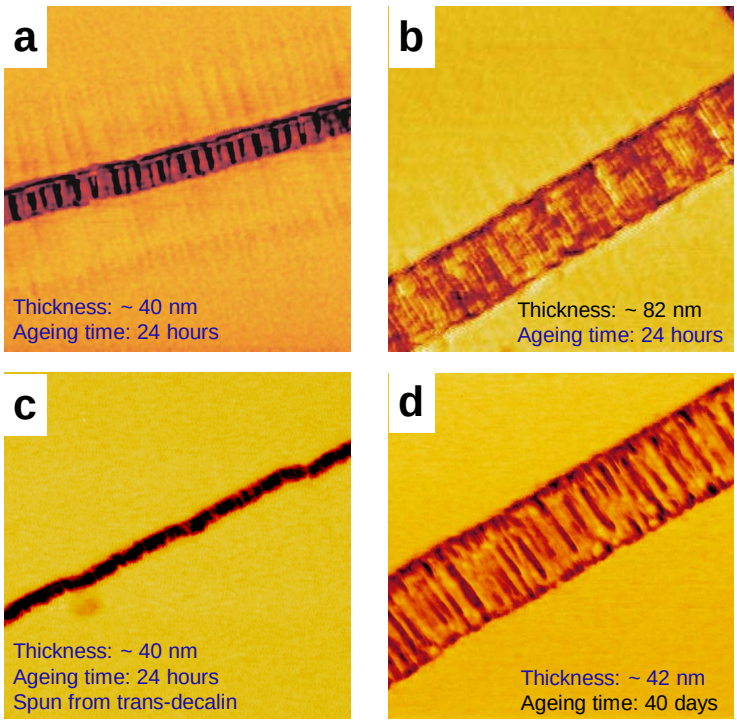

Figure 5.9 – AFM micrographs (phase images, size: 1 x 1 µm^2 each) showing a comparison of typical craze microstructures among several PS films (M_w = 4060 kg/mol) by varying film thicknesses or duration of ageing or the spin-casting solvent.

interconnected. Temporal propagation of a particular crack/craze was followed in real time. It was found that the craze propagation is decelerated with time. In a film of long chain polymer (PS 4060 kg/mol, thickness ca. 40 nm, aged at 90 °C for 24 hours), we found that the craze propagation velocity decreases as $V \sim t^{-(0.65 \pm 0.05)}$ (cf. **Figure 5.10**). A similar film of a short chain polymer (PS 52 kg/mol, which was also treated in the same way as the film of long chain polymers) did not show such a slowing down. Extremely fast (ca. 7-9 µm/s) crack propagation velocity was found in PS 52 kg/mol film in comparison to craze propagation in film of long chain PS 4060 kg/mol polymers (ca. 100-200 nm/s). It was found that ageing in long chain PS, for duration of several weeks to months can lead to comparably fast craze propagation velocity (like cracks in PS 52 kg/mol films) with stable crazes (cf. **Figure 5.10**). However, such increased velocity upon long duration of ageing was not observed for PS 52 kg/mol films. These observations are indicating a clear influence of elevated temperature ageing on the entangled chains. The possible role of ageing on such entangled chains will be discussed in detail later. No obvious thickness dependence of craze propagation velocities was found in the film thickness range investigated in these studies for all the polymers having a molecular weight higher than ca. 120 kg/mol.

In general, both for crazes and cracks a decrease in propagation velocity was observed when two crazes/cracks come closer to each other before connecting at almost in right angle. Zhang *et al.* studied the propagation of craze both theoretically and experimentally (on bulk PS sheet of mm thickness) leading to the conclusion of craze growth deceleration with time [203]. They considered each craze as an energy sink, which absorbs and dissipates energy from its own neighbourhood. A decrease in craze propagation rate can occur when the energy absorbed by crazing is used up for drawing new fibrils or when molecular entanglements enhance the stiffness of the fibril domain such that further opening becomes difficult. Considering the effect of the surrounding population of crazes, they concluded that the craze growth rate is affected by the local effective stress acting in the vicinity of the craze.

Ultrathin films of long chain polymers are supposed to have some stresses due to the out-of-equilibrium chain conformations frozen-in inside the reduced film dimensions. To find the exact role of residual stresses on the process of craze formation and its propagation, we varied the spin-casting solvent to change the initial state of chain conformation. All the experimental conditions (PS 4060 kg/mol, film thickness of ca. 40 nm, spun at room temperature, aged at 90 °C for 24 hours) were kept constant except for the solvent for PS. Trans-decalin (a theta-solvent of PS at 21 °C) was used instead of toluene (athermal solvent for PS). We found that the craze propagation velocity of the film made from trans-decalin solvent is lower than that of the film made from toluene (cf. **Figure 5.10**). Apart from that, AFM studies indicate that the craze width in films spun from trans-decalin is narrower than for similar films prepared from toluene (cf. **Figure 5.9 c**). Lower craze width and lower craze propagation velocity essentially indicate lower crazing stress (stress responsible for crazing) for films prepared from the near-theta solvent. This is indeed supporting our earlier report, where a film prepared from toluene was supposed to have a higher amount of residual stress due to its larger polymer coil deformation and larger inter-chain entanglements [45, 76]. So, one cannot deny the role of residual stresses on the process of crazing and craze propagation. Larger intrachain entanglements for a film prepared from toluene also signifies higher modulus.

5.4.3 Role of ageing on crazing and cracking

To understand the role of residual stresses and physical ageing, a systematic study of craze and crack propagation (followed under an optical microscope) was

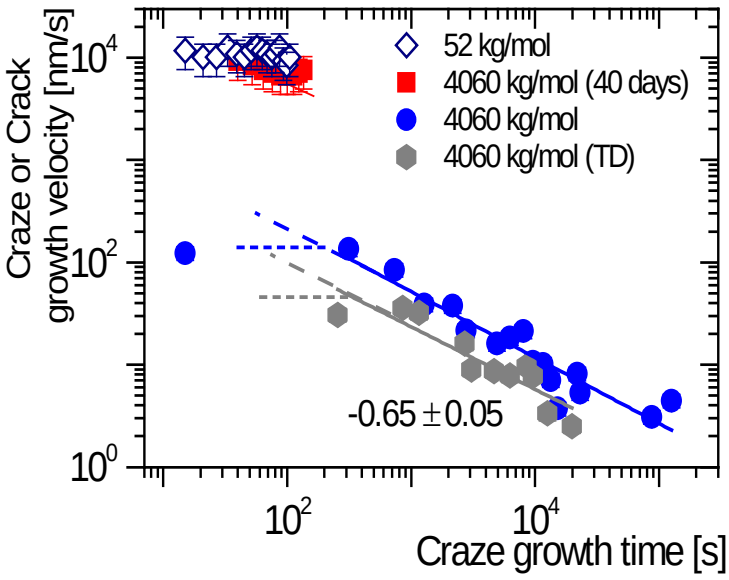

Figure 5.10 – Typical craze/ crack propagation velocities for different PS films of 42 ± 2 nm thicknesses, aged at 90 °C. The M_w of PS is 4060 kg/mol for all except blue open lozenges (52 kg/mol). Duration of ageing is 24 hours for all, except for the red full squares (40 days). Spin-casting solvent is toluene for all film except for the grey full diamonds where trans-decalin was used.

performed with varying duration of ageing at 90 °C. For the short chain polymer (PS 52 kg/mol) no notable change in the crack propagation velocity was observed upon varying ageing time (cf. **Figure 5.11 a**). For the very high molecular weight polymers (PS 4060 kg/mol and PS 16800 kg/mol), an increase in craze propagation velocity was found with increasing duration of ageing (cf. **Figure 5.11 a**). The increase of the craze propagation velocity with increasing ageing time might appear surprising as residual stress should decrease upon ageing. Possibly an elevated ageing temperature can impart some thermal stresses which should increase with duration of ageing. Increase in thermal stress is possibly associated with an increase in elastic modulus by re-entanglement of poorly entangled chains upon ageing, while decreasing residual stresses. However, the possibility of re-entanglement in the glassy state is very low.

To check the extent of residual stresses present inside an already aged and cracked film, dewetting at 125 °C was studied. A decrease (approximately in a single exponential way) in dewetting velocity was observed with increasing duration of ageing (cf. **Figure 5.12**). This is supporting our earlier observations of stress relaxations possibly due to segmental rearrangements [42]. The higher dewetting velocity for the PS 16800 kg/mol in comparison to PS 4060 kg/mol possibly signifies the higher amount of residual stress inside films of PS 16800 kg/mol, due to the higher molecular weight (cf. **Figure 5.12**).

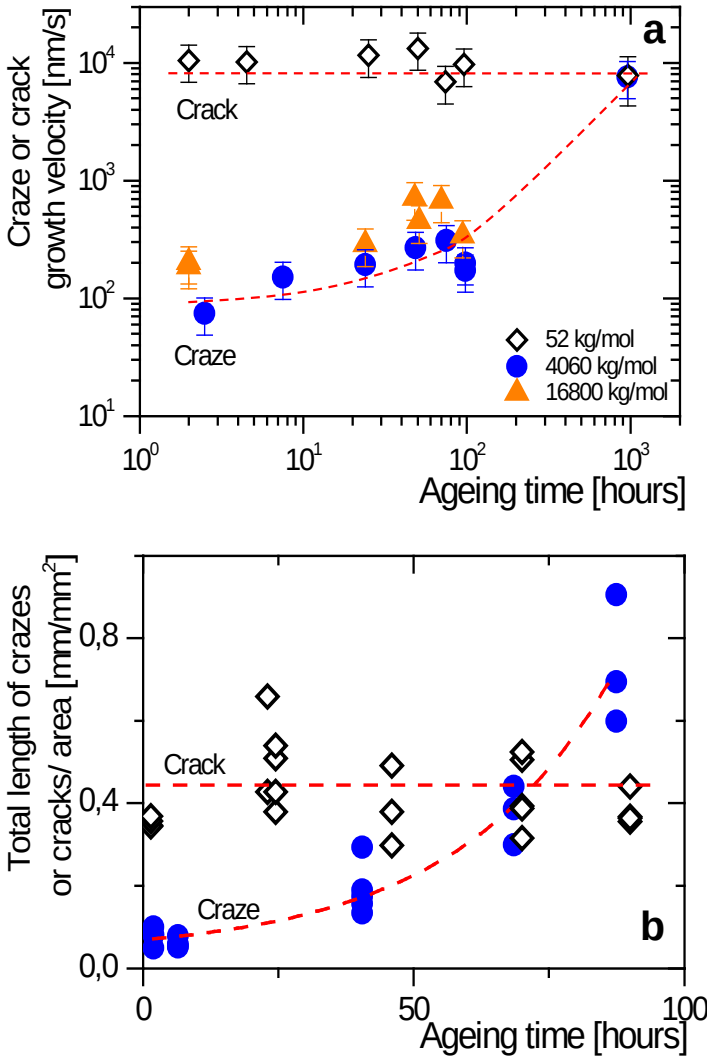

Figure 5.11 – (a) An increase in the craze propagation velocity (considered at ∼ 100 s of craze growth) with increasing ageing time was found for long chain polymers (PS, $M_w = 4060$ and 16800 kg/mol) whereas the crack propagation velocity for short chain PS ($M_w = 52$ kg/mol) remains almost constant upon ageing. (b) An increase in total length of crazes per unit area was found for long chain PS ($M_w = 4060$ kg/mol) whereas the total length of cracks per unit area for short chain PS ($M_w = 52$ kg/mol) remains almost constant upon ageing. The red dotted lines are guide to the eye. ageing time. For all the cases PS film thickness was set at 42 ± 2 nm.

In general, one can conclude that physical ageing causes a decrease in residual stresses (evidenced by the decrease in dewetting velocity) along with an increase in total stress which include thermal stress (cf. **Equation 5.1**) and residual stresses inside the film (evidenced by the increase in craze propagation velocity). Increase in total stress can be explained in terms of increase in thermal stress (cf. **Equation 5.1**) which might be associated with an increase in elastic modulus by re-entanglement of poorly entangled chains, while decreasing residual stresses. In other way, the total stress content inside the film might also be

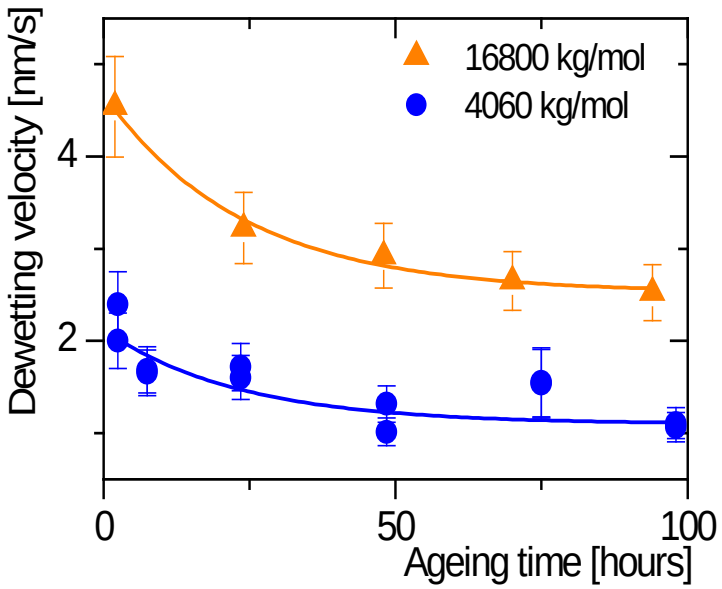

Figure 5.12 – Decrease in hole dewetting velocity (considered at $\sim$ 1000 s of dewetting) with increasing ageing time was found for long chain PS (M_w = 4060 and 16800 kg/mol), in a nearly exponential fashion. For all the cases PS film thickness was set at 42 $\pm$ 2 nm.

associated with stress evolution and inhomogeneous stress-localization while the film is relaxing at the elevated ageing temperature. Varying the duration of ageing in a film of long chain PS is not associated with any notable difference in craze microstructures until it was aged for a duration of several days. Higher craze width and smaller size of craze fibrils were found for a film (PS 4060 kg/mol, thickness ca. 40 nm, aged at 90 °C) which was aged for 40 days in comparison to a film aged for a day (cf. **Figure 5.9 d**). Increasing the duration of ageing led to an increase in crazing tendency. The total length of crazes formed in a particular area (after keeping the sample at room temperature for some fixed time after quenching from elevated ageing temperature) increases in a highly nonlinear fashion (cf. **Figure 5.11 b**).

Several models exist that try to explain the role of ageing on crazing. According to the model by Argon *et al.*, with increasing duration of ageing, there should be an increase in crazing stress (stress needed to initiate a craze) because yield stress and elastic modulus both increase upon ageing [204]. This also implies that the time for craze initiation at constant stress should increase. The model by Kambour predicts a decrease in crazing strain upon ageing because of the same reason of increasing yield stress and elastic modulus upon ageing [205]. This model could not clearly comment on the time to initiate crazing upon ageing. Till now there are no clear explanations on the role of ageing on craze propagation. Gusler *et al.* systematically studied the influence of physical ageing

on craze initiation [206]. An increase in crazing stress at 22 °C but a decrease in crazing stress at 60 °C was found for bulk PS under externally applied biaxial stress condition. This may indicate two different regimes for crazing behaviour. However no explanations were given for the origin of those two regions.

Particularly, ageing at temperatures close but below $T_{g,bulk}$ of the polymer should facilitate localized plastic deformations such as crazing/cracking. Increasing ageing time is associated with an increase in yield stress which may lead to stress localization. In such a case, deformations are allowed to proceed at a decreasing level of stress. So, a little variation in local strain rate can lead to plastic deformations. Stress localization is heterogeneous in nature. Eventually, an elevated ageing temperature (90 °C) is more prone to lead to heterogeneity in polymers, both for bulk and thin films [27, 28, 207].

5.5 Conclusions

In summary, we have shown that thin polymer films contain a certain amount of stresses resulting from preparation by spin-coating. These can lead to deformation (cracking and crazing) following a temperature change without any external mechanical straining. The role of physical ageing was investigated on the aspect of inherited residual stresses inside the film as well as thermal stresses imposed during elevated temperature ageing. A decrease in the residual stress upon physical ageing was evidenced through a decrease in dewetting velocity. The increase in craze propagation velocity might be signifying either an increase in total stress inside the film or stress localization while relaxing. Increase in total stress can be explained in terms of increase in thermal stress which might be associated with an increase in elastic modulus by re-entanglement of poorly entangled chains, while decreasing residual stresses. Though, the possibility of re-entanglement in the glassy state is very low. The role of entanglements on the fracture toughness of polymer was found to be in agreement with some already reported results in terms of craze-fibril stability. The morphologies of craze microstructures were interpreted in terms of various aspects, such as crazing stress, residual stress etc. inside such thin films.

5.6 Addendum

Several important observations on the process of crazing/ cracking are noted below:

(i) Samples aged only at room temperature never showed crack formation, probably due to the absence of thermal stresses. It has already been reported that the dewetting velocity showed a significant decrease during ageing at room temperature. In this case, there might be some decrease in residual stress or increase in friction between PS and PDMS, which apparently do not play a significant role in craze/crack nucleation.
(ii) Dust particles, scratches (especially at the sample edges) etc. represented flaws which preferentially nucleated cracking/crazing. However, the formation of cracks/crazes without such flaws was also possible. There nucleation probably started due to inhomogeneities in film thickness or of the substrate. For our already described systematic studies we always considered cracks/crazes which were not nucleated from any visible flaw.
(iii) The formation of cracks/crazes was only occurring on non-wettable Si wafers adsorbed with PDMS, whereas on bare Si-wafer no cracks/crazes were found. This might be due to the strong adsorption of PS on Si. This PDMS-coating "screened" all heterogeneities of the solid substrates and thus represented an ideally homogeneous surface of low surface tension and rather low interfacial friction for the moving PS-film, enabling slippage.

Chapter 6

Overall Conclusions

The main advantage of the experiments performed in this thesis is its simplicity, mostly using a simple optical microscope supplemented with atomic force microscopy. Dewetting and crazing (or cracking) represent rather simple experimental approaches which allow obtaining a wealth of information on the relation between the molecular scale interfacial properties and the mechano-rheological properties of polymers in thin films.

The central approach in this thesis was to probe the extent of residual stresses inside spin-coated glassy thin polystyrene films by studying viscoelastic properties and relaxation processes in these films. Residual stresses in such films of high molecular weight polymers are assumed to be the result of fast evaporation of the solvent during spin-coating of polymer solution, leading to frozen-in conformations of polymer chains which fall out-of-equilibrium and possibly have a low number of inter-chain entanglements. Residual stress is known to be a dominant factor at the early stage of dewetting of viscolelastic polymer thin films. So, the extent of residual stresses present inside a film can be estimated by measuring the characteristic features of dewetting holes, such as hole radius, rim width or rim height. Several theoretical treatments support the correlation of such physical parameters of hole growth with residual stresses present in the film. In a simple way, one can assume that large values of these quantities after a certain period of dewetting at a particular temperature are indicative of fast dewetting dynamics and high residual stress.

In **Chapter 3** we studied the physical ageing of thin polymer films below the glass transition temperature, in terms of probing the relaxation of residual

stresses by studying the dewetting dynamics. It was found that dewetting exhibits a close to exponential decay of film properties with ageing time, defining a characteristic relaxation time. We found, at all ageing temperatures, these relaxation times were much faster than the reptation time of the bulk polymer. The variation of relaxation times with temperature seems to follow an Arrhenius dependence. This suggests a process of relaxation which takes place at the segmental level of the polymer and is sufficient to relax part of the residual stresses during physical ageing. Moreover, the relaxation dynamics of residual stresses appears to be in close agreement with some earlier reports, concerning relaxation solely at the surface of polymer thin films. So, our results certainly invoke the possibility to explain the unexpectedly fast surface relaxation dynamics in thin films in terms of residual stresses induced by film preparation. Relaxation times were found to vary strongly with the quality of the solvent from which the film was spun. This signifies that chain conformations in the initial solution have a great impact on the behaviour of resultant dry films due to the out-of-equilibrium conformations that can be frozen in.

The convincing indications for the role of film preparation conditions on the ageing behaviour of thin films far below the $T_{g,bulk}$ of the polymer and the observation of significant changes even at room temperature may also be of relevance in the context of the low softening temperature of thin polymer films, typically elucidated as a reduced glass transition temperature. While the deformation of polymer coils as a whole should not modify the solidification (glass transition) temperature of the film, which is mainly governed by the segmental dynamics, our ageing experiments indicate that spin-coating influences polymer chain conformations even at the segmental scale. The present study cannot clearly point out whether or how our observations using dewetting can be correlated with a reduced glass transition temperature. Thus, further experiments are needed to verify if non-equilibrium chain conformations inside a spin-coated polymer film can explain abnormal puzzling properties of thin polymer films like for example the deviations from the glass transition temperature in the bulk.

In **Chapter 4** we have shown that, independent of molecular weight, relaxation times of residual stresses (indicated by the maximum of the width of the rim around a dewetted hole) are comparable for high molar mass ($M_w \geq 300$ kg/mol) polystyrene thin films, as measured through dewetting at different temperatures. All these times are remarkably smaller than the estimated reptation times for bulk polymer at the corresponding temperatures. For low-M_w , this relaxation was clearly comparable to the reptation time (τ_{REP}), suggesting that

this relaxation process is dominated by the mobility of whole chains (reptation). In contrast, for high-M_w , very large deviations with respect to bulk reptation times were observed, suggesting that motion at the segmental scale is sufficient to partially relax the residual stresses generated during the film preparation. Above results clearly demonstrate that dewetting can be considered as a nano-rheological probe to look into the structure and properties of out-of-equilibrium polymer thin films.

In **Chapter 5,** it was shown that physical ageing at elevated temperatures but below $T_{g,bulk}$ is capable to induce stresses resulting in cracking/crazing in ultrathin glassy polymer films, made visible by cooling the film towards room temperature. For long chain polymers, AFM inspection inside the cracking patterns showed craze nano/microstructures consisting of voids and fibrils. Short chain polymers (of length comparable to the entanglement length) did not show such crazes, rather formed simple cracks. For higher molecular weight polystyrene, a systematic study of craze propagation velocity showed a progressive increase with increasing ageing time whereas for the same films the dewetting velocity decreased with ageing. While increase in craze propagation velocity indicates an increase in total stress inside the film, the decrease of dewetting velocity is a signature of relaxation of residual stresses. Increase in total stress might be associated with an increase in elastic modulus by re-entanglement of poorly entangled chains. Though, the possibility of re-entanglement in the glassy state is considerably less.

In general, using experimental approaches like dewetting and cracking (or crazing) we probed the mechanical properties of polymers caught inside thin films. Our work was able to enlighten the highly debated area of relaxation (mobility) in thin glassy polymer films in terms of tunable non-equilibrated chain conformations, observed in relation to relaxation of residual stresses.

APPENDICES

Chapter 7

Appendix-I: Relaxation of Thin Polymer Films during Nucleation of Dewetted Holes

7.1 Abstract

We have to distinguish holes nucleated in the course of dewetting from holes formed right after reaching the dewetting temperature. Holes that nucleated at increasing times (incubation time) after the film temperature was raised to dewetting temperature exhibit a clear decrease in hole growth velocity with increasing incubation time. A comparison of the hole radius after a certain hole-opening time indicates a nearly exponential relaxation, yielding a decay (relaxation) time for the hole-opening driving force. Such relaxation time is much faster (smaller) than the bulk reptation time of the polymer at the dewetting temperature.

7.2 Experimental

All the experiments were performed on high molecular weight polystyrene films (PS, M_w = 4060 kg/mol and 16800 kg/mol, M_w/M_n = 1.15 and 1.3 respectively, thickness = ca. 40 nm), spun-casted either from solutions of toluene or trans-decalin (a theta-solvent for PS at 21 °C). All the films were spun at 3000 rpm on Si (100) substrates, which was previously coated with an irreversibly adsorbed thin non-wettable PDMS layer of ca. 15 nm thickness [42]. Procedural details involving the preparation of PDMS layer have been discussed in **Section 2.1.3** of this thesis. The PDMS layer acts as a liquid layer enabling slippage, and thus

facilitating dewetting of PS film. For those samples having an ageing history below $T_{g,bulk}$, ageing had been done in an oven equipped with an oil free vacuum pump. Temporal evolution of dewetted hole growth was followed in real time by optical microscopy during the early stage of dewetting at 125 °C.

7.3 Results and discussions

Because holes in the film nucleate at various times, as seen in **Figure 7.1 a**, it is possible to simultaneously follow the temporal evolution of holes/rim profiles of several holes. At a fixed temperature, holes that nucleated at different times grow in parts of the film that have been annealed at $T = 125$ °C for different periods of time. The time for hole nucleation is therefore defined as the incubation time in annealing studies. The growth of the holes marked 1–3 in **Figure 7.1 a** was followed in time for a ca. 40 nm thick film of PS ($M_w = 16800$ kg/mol). **Figure 7.1 b-c** show the results as a function of dewetting time and nucleation (incubation) times respectively. The data show a significant slowing down of the hole-opening rate with time, faster than for purely viscous films, which is indicative of a viscoelastic rheology [105]. Holes that nucleated at increasing times after the film temperature had reached to 125 °C exhibited a clear decrease in growth velocity with increasing incubation time. A comparison of the hole radius of the three holes after a hole-opening time of ca. 2000 s (as indicated in **Figure 7.1 d**) indicates a nearly exponential decay, yielding a decay time of ca. 1000 ± 500 s for parts of the hole-opening driving force.

Similar study on dewetting of thin polymer films has been extended to PS films prepared from trans-decalin (a near theta-solvent at room temperature). Dewetting of a PS film ($M_w = 4060$ kg/mol, thickness is ca. 40 nm) was followed at 125 °C (after 45 hours ageing at room temperature). A clear exponential decrease in dewetted hole radius (after a hole opening time of 500 s and 1000 s) with incubation (nucleation) time was observed, yielding a decay of 2005 ± 225 s (cf. **Figure 7.2 a-c**). This is nearly in agreement with the value of ∼ 30 min found earlier for nominally similar PS film [45].

Further, PS ($M_w = 4060$ kg/mol, thickness is ca. 40 nm) films which are prepared from toluene and aged at an elevated temperature (90 °C for 87.5 hours) were subjected to dewetting at 125 °C . Holes generated during the course of dewetting were followed similarly with respect to the incubation (nucleation) time (cf. **Figure 7.3 b**). A comparison of the hole radius of different holes after

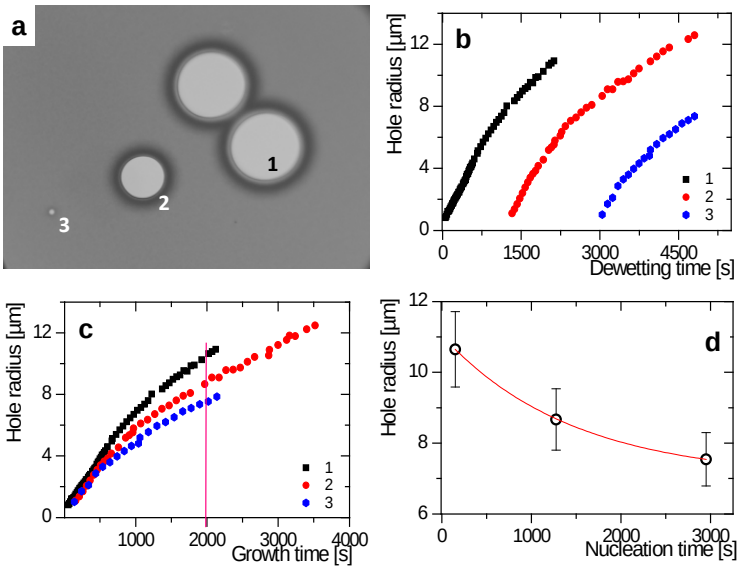

Figure 7.1 – (a) Optical micrograph (size: 143 x 106 µm^2) of a typical PS film (M_w = 16800 kg/mol, thickness is ca. 40 nm) cast from toluene at 23 °C, after heating for ∼ 53 min at 125 °C. Smaller holes were nucleated after longer incubation times compared to bigger holes. (b) Growth of the four holes marked 1–3 in (a), which were nucleated 90, 1275, and 2950 s after the film was brought to 125 °C. (c) Growth of the same holes where the ordinate is the time that each hole has grown since it was nucleated, rather than the time elapsed since the film reached T = 125 °C. (d) Plot of the hole radii of the three holes after a growth time of 2000 s (vertical line in (c)), showing an exponential decay with a time constant of ∼ 1000 ± 500 s.

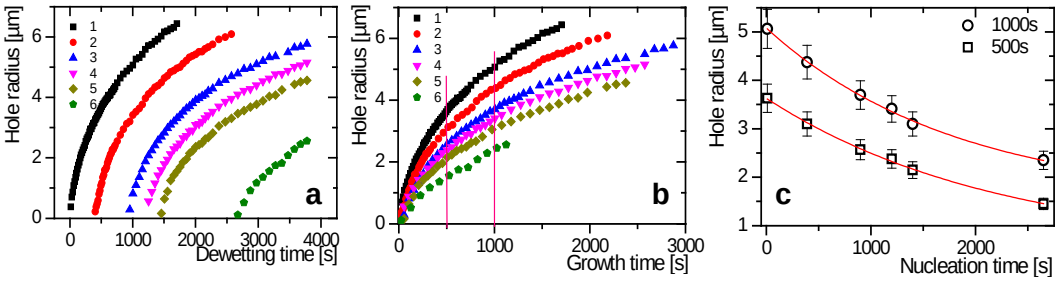

Figure 7.2 – (a) Growth of six holes in a PS film (M_w = 4060 kg/mol, thickness is ca. 40 nm, aged at room temperature for 45 hours) which were nucleated 10, 390, 900, 1200, 1400, and 2650 s after the film was brought to 125 °C. (b) Growth of the same holes where the ordinate is the time that each hole has grown since it was nucleated, rather than the time elapsed since the film reached T = 125 °C. (c) Plot of the hole radii of the six holes after a growth time of 500 s and 1000 s (vertical lines in (b)), showing an exponential decay with a time constant of ∼ 2005 ± 225 s.

a hole-opening time of ca. 1000 s in **Figure 7.3 c** indicates an nearly exponential relaxation, yielding a decay time of ca. 1910 ± 1180 s for the hole-opening driving force.

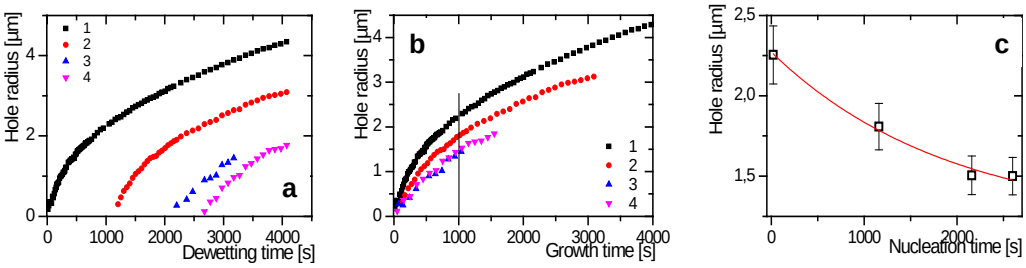

Figure 7.3 – (a) Growth of four holes in PS film (M_w = 4060 kg/mol, thickness is ca. 40 nm, aged at 90 °C for 87.5 hours) which were nucleated 20, 1160, 2160, and 2600 s after the film was brought to 125 °C. (b) Growth of the same holes where the ordinate is the time that each hole has grown since it was nucleated, rather than the time elapsed since the film reached T = 125 °C. (c) Plot of the hole radii of the four holes after a growth time of 1000 s (vertical line in (b)), showing an exponential decay with a time constant of $\sim$ 1910 $\pm$ 1180 s.

Comparison of relaxation times (at 125 °C) found for these high molecular weight PS films indicate values which are in close agreement to each other, lying within ca. 30 $\pm$ 15 min. This is much smaller than the bulk reptation time for the high molecular weight PS used here at 125 °C (ca. 65 years) [81]. Interestingly, number of later grown holes (secondary holes) upon dewetting increases for those films, which were aged, in comparison to a fresh film. While ageing at room-temperature for films prepared from a theta-solvent is sufficient to see that effect, ageing at 90 °C is necessary for films prepared from toluene. It is surprising to observe nucleation of additional holes when the film has been already partially relaxed through ageing. A similar observation was made by Richardson *et al.*, where they observed that structural relaxation in supported thin polymer films can generate stress which can cause plastic deformation finally leading to the generation of dewetted holes [179].

Earlier experimental studies and numerical calculations clearly showed that the residual stress (σ_0) constitutes an additional driving force for the dewetting. In the presence of residual stress, assuming linear friction, the initial velocity of the dewetting process is increased by a factor of $\left(1 + \frac{h_0\sigma_0}{|S|}\right)$ [42, 57, 102, 105]. Thus, a decrease in the initial dewetting velocity supports the hypothesis that the chains in the films, which were initially out of equilibrium, starts to equilibrate during annealing during the course of dewetting.

7.4 Conclusions

In summary, our experiments show that chains in the polymer films, which were initially out of equilibrium, proceed to equilibrate during annealing. Relaxation time at the dewetting temperature was found to be much smaller than the reptation time of the bulk polymer. This fact indicates a motion in the segmental scale of the polymer chain, at a temperature, which is above but close to the glass transition temperature of the bulk polymer. Our study shows that it is important to determine the exact time of nucleation of dewetted holes in a film. One has to take in account thermal history during incubation before dewetting starts.

Chapter 8

Appendix-II: A Comparative Study of Different Cracking and Crazing Protocols in Thin Polymer Films

8.1 Abstract

Polymer films and coatings deposited on solid substrates often develop stresses large enough for cracking. This chapter summarizes several possibilities and observations leading to stress evolution inside such films mainly during preparation or shortly after it. Spin-coated polymer thin films are supposed to contain a substantial amount of residual stresses, which are supposed to originate from fast evaporation of solvent leading to non-equilibrium polymer chain conformations. While several works in the literature are available to quantify and characterize the residual stresses inside a spin-coated film, very few have discussed the possibility of intrinsic deformation and failure inside the film. This chapter initiates that discussion with a special emphasis on the possible appearance of polymer rich 'crust' layer at the film surface, which is supposed to form during the early stage of spin-coating. The 'crust' is supposed to be under mechanical tension and thus prone to rupture, hence possibly leading to cracking or crazing patterns. Such patterns are frequently observed in the here presented experiments, when spin-coating thick films (ca. 90 nm and above) of polystyrene on a non-wettable substrate. Detailed investigations through atomic force microscopy for long chain polymers revealed the existence of craze microstructures, similar to few early reported craze morphologies in thin polymer films. For short chain polymers (comparable to the entanglement length) simple cracks were found instead

of crazes containing fibrils.

8.2 Introduction

8.2.1 Shrinkage cracking in polymeric films and coatings

Cracking induces fascinating patterns that often occur in nature such as fracture in solids, rocks, woods, paints, mud and polymer layers. Technologically speaking however, cracking of polymer thin films poses a big threat concerning the stability of surface coatings in advanced technologies to valuable arts. Cracking of a thin layer of material coated to another surface or interface is quite common. Most polymeric coatings shrink after solidification due to solvent evaporation. Drying mediated cracking pattern is of that kind which causes mainly due to non-uniform shrinkage (or expansion) if attached to a surface. Polymer films on a substrate often generate lateral shrinkage, which is prevented by pinning of the film onto the substrate. This frustration of in-plane shrinkage leads to a tensile stress in the plane of the coating. In the simplest case, stress in a polymer coating starts to develop when the coating has dried or cured enough so that it has developed elasticity and can support a stress. Croll defined this initial "solidified" state in drying polymer solution coatings as the point at which the glass transition temperature of the coating (which is a function of solvent content) is equal to the drying temperature [141]. Further shrinkage from this initial state may occur freely in the thickness direction, but is constrained in the plane of the coating. In the linear regime, in-plane stress in the coating at a time t, $\sigma(t)$ is proportional to the strain at that time, $\epsilon(t)$, and the elastic property of the coating is

$$\sigma(t) = \frac{1}{3}\frac{E_f}{1-\nu_f}\epsilon(t) \tag{8.1}$$

Away from the edge of the coating, the stress due to constrained shrinkage is tensile and in the plane of the coating. Hence, the biaxial modulus $(E_f/(1-\nu_f))$ in **Equation 8.1** is appropriate. E_f and ν_f are the Young modulus and Poisson ratio of the film. Near of the edge, shear and out-of-plane stresses appear, but these decay to zero at a distances of a few coating thicknesses from the edge [208].

The situation of stress evolution in spin-coated thin polymer films on a solid substrate is markedly different from the slow drying mediated cracking in polymer coatings in several aspects. Slow drying mediated stress generation in

polymer layers can take place even long after (from minutes to months, depending on the materials) the formation of the film, whereas stress generation in spin-coating takes place during the process of coating. Different stages of spin-coating involving rapid solvent evaporation in the film were conjectured by Reiter and de Gennes [76]. At the early stage, a metastable physical polymer network was formed, as the film has just been solidified (concentration vitrification) by solvent evaporation. This takes place as the solvent content reached a characteristic value, $\phi_g \sim$ 14-20 %, and vitrification can lead to a glass transition of the polymer at room temperature. Fast vitrification makes the process of spin-coating different from slow drying. Stress generation due to slow evaporation supports the idea of volume change even after the glass transition, whereas for spin-coated films, Reiter and de Gennes recognized that the original chain network structure, once formed (at stage α, cf. **Figure 1.14**), establishes a rigidity that would resist the film from further volumetric changes during the process of spin-coating [76]. At the late stages of spin-coating, the remaining solvent evaporates which can take place at room temperature. This is most likely the stage when the residual stresses are generated.

8.2.2 Idea of 'crust' formation and rupture during spin-coating

Scriven *et al.* modeled the process of formation of a glassy polymer film by fast evaporation [140], the region near the free surface is polymer rich and becomes glassy first, forming a skin-like solid 'crust' layer, long before the freezing of the whole film (cf. **Figure 8.1 b**). To explain the formation of a 'crust', simple arguments based on diffusion and transport of solvent from the film to air were considered by de Gennes, where the nonlinear variation of solvent volume fraction, ϕ lead to the rapid formation of a surface 'crust' layer of width d at $\phi_f \approx \phi_g$, while the composition deeper in the film is $\phi_f > \phi_g$ (cf. **Figure 8.1 a**) [171]. A rough estimation considering reasonable values of quantities like solvent fraction, solvent vapour pressure, and diffusion coefficient of the solvent yields a crust thickness of ca. 70 nm.

Later on, a MD-simulation study showed that the formation of 'crust' is only possible for a high solvent evaporation rate, which can however be achievable during spin-coating [209]. However, the exact nature of the 'crust' is a matter of controversy. Whether it is a region of a viscoelastic fluid, a layer of a soft gel, or a film of glassy polymer has not been answered clearly. Whatever the nature of the 'crust' is, the viscous fluid becomes elastic during evaporation of the solvent [210].

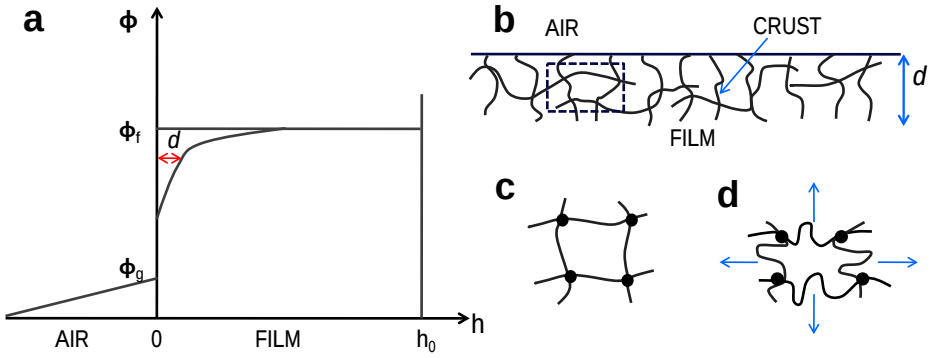

Figure 8.1 – Schematic representation of the solvent volume fraction ϕ in the film and the adjacent air/vapour diffusion layer. The nonlinear variation of ϕ leads to the rapid formation of a surface layer of width d with $\phi_f \approx \phi_g$, while the composition deeper in the film is $\phi_f > \phi_g$. The "crust": b) overall view; c) enlarged view of one mesh unit at the first freezing time; d) the same unit, at later times under horizontal tension. Reproduced from ref. [171].

Till during the process of spin-coating the volume of the 'crust' decreases, but its horizontal dimensions have to remain the same. Thus, there should be a tensile stress in the 'crust' (cf. **Figure 8.1 c-d**). Calculations by de Gennes showed that the ratio of stress to elastic modulus should be sufficient to induce either plastic deformation or fracture in the crust. Fracture is indeed favored because the crust is thin and it is expected to have heteregenous regions which can play the role of nucleation centers. Thus, the outer surface of the film should rupture exhibiting a network of fracture lines similar to mud-crack patterns [171]. De Gennes also pointed out the possibility of rupture, creating a rough surface. Although several theoretical descriptions for a'crust' are available for thin polymer films, to date no direct experimental observation of the'crust' has been made in thin polymer films during spin-coating. Observations by Strawhecker *et al.* indicated anomalously high surface roughness of the final films when the pure solvent has a high vapor pressure [211]. De Gennes discussed this event in terms of the possibility of a ruptured 'crust'. High vapour pressure should lead to a thinner 'crust' which is probably prone to rupture leading to an increased roughness in the film [171]. The observation of cracking patterns in spin-coated polymer films in the present experiments invokes the possibility of the existence of a 'crust' which might rupture.

8.3 Experiments, results and discussions

For all the cracking experiments, PS films were coated over a non-wettable Si-wafer, having a thin (ca. 15 nm) PDMS layer adsorbed on it. Here the PDMS layer acts as an apolar liquid layer allowing for slippage. The preparation procedure involving the preparation of PDMS layer have been discussed in **Section 2.1.3** of this thesis in detail. All the films were spun at 3000 rpm.

8.3.1 Occasional cracking during spin-coating

Crack patterns were found right after the completion of spin-coating of PS solution (in toluene). So, it was clear that those cracking patterns were generated during the process of spin-coating. Notably, cracking was found for thicker films (thickness ca. 90 nm and above) only. Most cracks were isolated, single and wide. Occasionally such cracks were found for films of high molecular weight PS films (thickness ca. 100-105 nm, molecular weight = 4060 kg/mol) (cf. **Figure 8.2 a**). AFM investigations inside the crazes indicated nano/microstructures of closely spaced fibrils separated by voids (cf. **Figure 8.2 c**). A non-fibrillated portion through the center of the crazed line was also found, from which fibril drawing was supposed to take place during crazing. The observed craze microstructures resemble a porous sheet of voids and closely packed fibrils (cf. **Figure 8.2 c and 8.3 b**), similar to those found by Kramer group for PS films under external mechanical straining [199]. Similar to the present observation, a non-fibrillated zone in the middle of the craze was also observed, termed as 'midrib' (cf. **Figure 8.2 c**).

We found isolated cracks for low molecular weight PS (9 kg/mol, 17 kg/mol) films of higher thicknesses (ca. 100-250 nm). AFM inspection indicated no stable craze fibrils inside the crack signifying the role of entanglement (chain length) on the fracture toughness (craze fibril stability) of the polymer, in accordance with earlier experimental and theoretical observations: no stable crazes are possible below a critical molecular weight M_c ($M_c \sim (3\pm1)M_e$, entanglement molecular weight) [126, 198]. Gabriele and Coppee also reported the formation of isolated as well as interconnected cracks, for a similar system involving spin-coating of ca. 100 nm thick polymer films on a PDMS coated non-wettable Si-wafer [137, 212]. They concluded that, cracking is more probable to occur in films of low molecular weight (below M_c) PS. During the evaporation of residual solvent during spin-coating, the film possibly undergoes a contraction in the

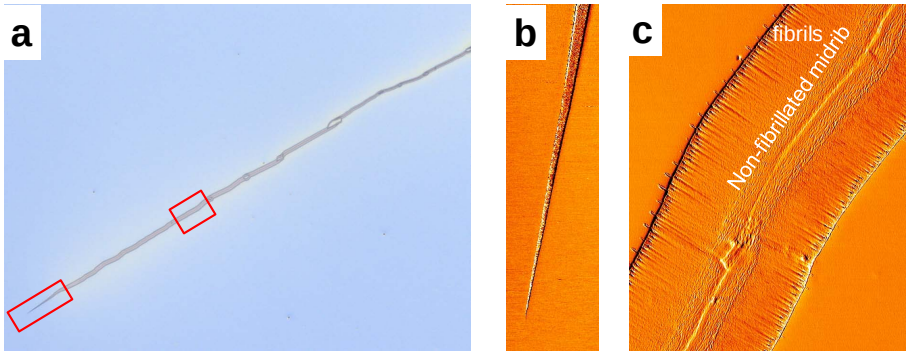

Figure 8.2 – (a) Optical micrograph (715 x 530 μm^2) showing a typical isolated crazing line found in a ca. 127 nm film of PS 4060 kg/mol, right after spin-coating. (b) AFM micrograph (phase image, 8 x 30 μm^2) of the craze tip. (c) AFM micrograph (phase image, 8 x 10 μm^2) inside such crazes indicates highly fibrillated craze microstructure with occasional holes. The AFM micrographs (b, c) approximately represent the marked regions in (a).

'crust' layer, which cannot be opposed or sustained by the polymer chains due to the lack of entanglements. Thus, the only possibility for releasing this tension, is by fractures. We found interconnected network of crazes (similar to mud-crack patterns) for PS (molecular weight = 1070 kg/mol) films of thickness ca. 95 nm, (cf. **Figure 8.3 a**). Detailed study through atomic force microscopy showed the existence of some polymeric structures within the fracture line. Clearly, separated voids and fibrillar structure representative of craze were not observed, rather structures that consisted of densely packed fibrils were found (cf. **Figure 8.3 b**).

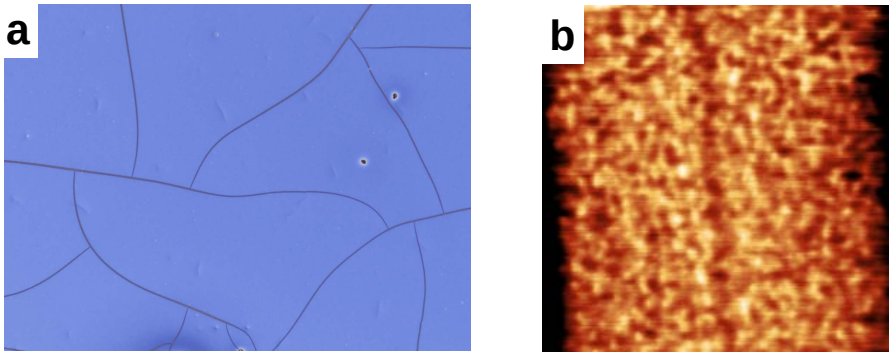

Figure 8.3 – (a) Optical micrograph (715 x 530 μm^2) showing typical interconnected crazing patterns found in a ca. 95 nm film of PS 1070 kg/mol, right after spin-coating. (b) AFM micrograph (phase image, 2 x 2 μm^2) inside such crazes indicates highly fibrillated craze microstructure with occasional holes.

We never found interconnected crazing patterns during spin-coating of similar thickness films for several other polystyrenes of higher or lower molecular weights. We do not have any definite explanation to justify the occurrence of

generated patterns (either interconnected or isolated). In general, interconnected patterns indicate that several nucleation points existed. Besides, uniaxial stress is probably not responsible for such cracking.

The possibility of cracking or crazing in a spin-coated polymer film is the focus of the present experimental investigations. Earlier discussions indicated the role of spin-coating on stress evolution inside a polymer thin film. Most of the views support the accumulation of stress during late stages of spin-coating, after vitrification [76, 213]. The amount of stress is sufficient to induce crazing or yielding in polymer thin films under proper conditions. About a decade ago, McKenna proposed that the corresponding biaxial strains due to the biaxial constraints of the film to the substrate are on the order of 0.045, which is sufficient for yielding of the polymer film [213]. He commented: the spin coating process could be a deformation induced polymorphism, given that the yielded material could be different from the undeformed material with respect to its thermodynamic state. Use of **Equation 8.1** and considering $E_f \sim 3$ GPa and a strain of 0.045 generates a plane stress of the order of 100 MPa, which is sufficient to induce yielding or crazing in the polymer film.

Formation of crazing/cracking patterns during spin-coating may be in line with the theoretical interpretation by de Gennes, concerning a polymer rich 'crust' at the thin film surface, which is supposed to rupture leading to crack patterns. We never found any kind of crack/craze formation for films thinner than ca. 90 nm. Intriguingly, the estimated thickness of a 'crust' by de Gennes was ca. 70 nm, which corresponds with our observation of occasional cracking in thick films (ca. 90 nm and above) of polystyrene during spin-coating onto a non-wettable substrate. Cracking/crazing patterns formed during spin-coating did not possess high regularity and reproducibility in occurrence. Though the detailed understanding of the cracking/crazing process during spin-coating is yet missing, it is clear that the occurrence of such cracks/crazes is limited to non-wettable (adsorbed PDMS layer over Si-wafer) substrates. This may indicate the role of the substrate on 'crust' shape and possible buckling, which guides further processes of rupturing [214].

8.3.2 Cracking or crazing of a spin-coated film by physical ageing

Ageing at elevated temperature (such as at 90 °C) followed by cooling to room temperature also generates interconnected crazing or cracking patterns, possibly

due to the film-substrate thermal expansion mismatch (see the scheme of thermal treatment, cf. **Figure 2.6**). In our films cracking process occurs in a regular and reproducible manner for a wide range of thicknesses (ca. 35 nm to ca. 250 nm). For the purpose of a comparison of ageing mediated crazes, a PS film (1070 kg/mol, thickness ca. 90-95 nm) which was already crazed during the spin-coating process was subjected to elevated temperature ageing and cooling. The morphology of such crazes was distinctly different from those formed during the spin-coating (cf. **Figure 8.4 a-b**). Crazes formed by ageing have lower width in comparison to those formed during spin-coating. Formations of crazes caused by ageing took place slowly (several hours), which finally led to an interconnected pattern. Details on the process of crazing/cracking due to elevated temperature ageing have been discussed in **Chapter 5**.

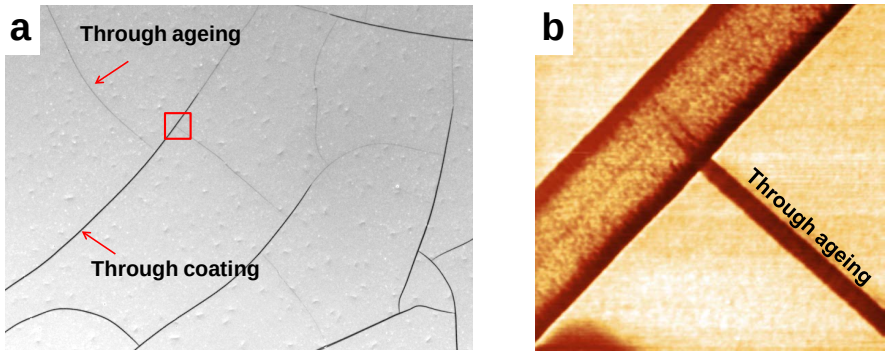

Figure 8.4 – (a) Optical micrograph (950 x 700 μm^2) showing formation of new crazes through ageing (at 90 °C for 24 hours and kept 2 hours at room temperature after quenching) in a film of ca. 95 nm of PS 1070 kg/mol, which was already partially crazed during spin-coating. (b) AFM micrograph (phase image, 5 x 5 μm^2), corresponding to the marked region in (a), indicates a junction between two types of crazes highlighting the difference in craze microstructure.

8.3.3 Cracking or crazing of a spin-coated film by immersion in a non-solvent

In addition, cracking experiments in thin PS films (film thickness = 40 nm, molecular weight = 4060 kg/mol) were performed by dipping the film in a non-solvent. Heptane is a non-solvent for PS whereas it is a good solvent for PDMS. Spontaneous crazing took place when PS films (either fresh or aged) were dipped into a non-solvent, such as heptane. Such crazing is more violent and also generated partial delamination (cf. **Figure 8.5 a-b**). Here heptane is acting as an environmental stress cracking agent (ESC), as it generally swells and plasticizes polymer

chains or reduces the surface energy of the polymer surface or both, and there by generates cracking [215]. Crazing/cracking by dipping films inside heptane is also possible for an already aged film (aged at a temperature close to $T_{g,bulk}$ of PS, such as at 90 °C, followed by immediate immersion inside heptane), but to significantly lesser extent than a relatively fresh PS film. With increasing duration of elevated temperature ageing, immersion-mediated crazing/cracking got slowed down and eventually stopped.

This is opposite of that was found for crazing after cooling down the film from elevated temperature to room temperature. It showed a higher tendency of crazing upon increasing the duration of ageing. We do not have any clear explanation for this observation. It might be speculated that heptane is modifying the PDMS layer in some important way, which results in crazing/cracking to a different extent for differently aged films. The role of the PDMS layer appears essential as we never found any immersion induced crazing/cracking in PS films coated directly on Si-wafer (film thickness investigated: 40-100 nm).

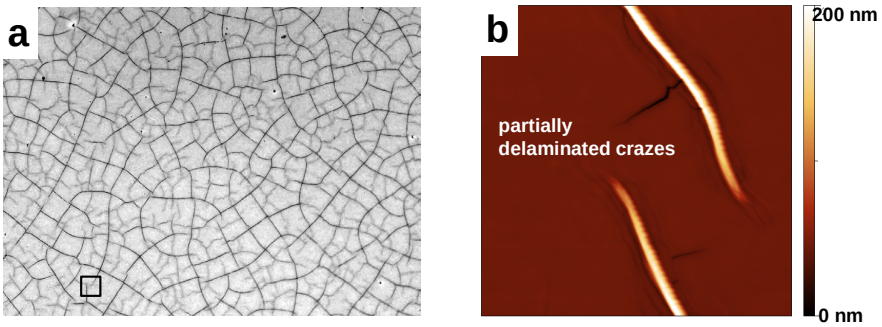

Figure 8.5 – (a) Optical micrograph (950 x 700 µm^2) showing crack and craze formation in an as-cast fresh film of PS 4060 kg/mol of thickness ca. 40 nm after immersion in heptane for 5 minutes. (b) AFM micrograph (phase image, 5.5 x 5.5 µm^2) corresponding to the marked region in (a) is showing both cracks and crazes with partial delamination.

8.4 Conclusions

In summary, our experiments showed that spin-coating can generate stress and deformation in thin polymer films with characteristic craze/crack morphologies. Moreover, our experiments support the long standing and well explored theoretical view on the formation of a polymer rich 'crust' layer during the spin-coating process. Such 'crust' was supposed to be under mechanical tension and can rupture leading to cracks/crazes. The role of the PDMS layer is demonstrated by

observation that we never found any kind of crazing/cracking for PS thin films coated directly onto Si-wafer. The role of the non-wettable PDMS layer is important for the propagation of cracks/crazes. Cracking/crazing by non-solvent immersion indicates some possible heptane-PDMS layer interaction contributing to the process of cracking/crazing. The occurrence of stable crazes for long chain polymers (above a certain chain length comparable to entanglement length) further supports the influence of entanglement and chain length on fracture toughness of polymer.

Bibliography

[1] Mülhaupt, R. *Angew. Chem. Int. Ed.* **43**, 1054–1063 (2004).

[2] Fakhraai, Z. *Dynamics of polymer thin films and surfaces.* PhD thesis, University of Waterloo, (2007).

[3] de Gennes, P.-G. *Angew. Chem. int. Ed. EngI.* **31**, 842–845 (1992).

[4] Witten, T. A. *Rev. Mod. Phys.* **71**, S367–S373 Mar (1999).

[5] de Gennes, P.-G. *Scaling concepts in polymer physics.* Cornell University Press (Ithaca, N.Y.), (1979).

[6] Kléman, M. and Lavrentovich, O. *Soft matter physics: an introduction.* Springer-Verlag, New York, (2003).

[7] Rubinstein, M. and Colby, R. *Polymer Physics.* Oxford University Press, (2003).

[8] Jones, R. *Soft condensed matter.* Oxford Univ. Press, (2004).

[9] Berry, G. and Fox, T. G. *Adv. Polym. Sci.* **5**, 261 (1968).

[10] Perkins, T., Smith, D., and Chu, S. *Science* **264**, 819–822 (1994).

[11] Ghosh, P. *Polymer science and technology.* Tata McGraw-Hill, (2002).

[12] Anderson, P. *Science* **267**, 1615 (1995).

[13] Keddie, J., Jones, R. A. L., and Cory, R. *Europhys. Lett.* **27**, 59–64 (1994).

[14] Debenedetti, P. and Stillinger, F. *Nature* **410**, 259–267 (2001).

[15] Haward, R. and Young, R. *The Physics of Glassy Polymers.* Chapman and Hall, London, UK, (1997).

[16] Jones, R., Kumar, S., Ho, D., Briber, R., and Russell, T. P. *Nature* **400**, 146–149 (1999).

[17] McKenna, G. *Nature Physics* **4**, 673–674 (2008).

[18] Williams, M. L., Landel, R. F., and Ferry, J. D. *J. Am.Chem. Soc.* **77**, 3701 (1955).

[19] Liu, C.-Y., He, J., Keunings, R., and Bailly, C. *Macromolecules* **39**(25), 8867–8869 (2006).

[20] Bower, D. I. *An Introduction to Polymer Physics*. Cambridge University Press, (2002).

[21] Kremer, F. and Schönhals, A. In *Broadband dielectric spectroscopy*. Springer-V (2003).

[22] Johari, G. and Goldstein, M. *Journal of Chemical Physics* **53**, 2372–2388 (1970).

[23] Simon, S. L., Plazek, D. J., Sobieski, J. W., and McGregor, E. T. *Journal of Polymer Science Part B: Polymer Physics* **35**(6), 929–936 (1997).

[24] Struik, L. *Polymer Engeering and Science* **17**, 165–173 (1977).

[25] Russell, E. V. and Israeloff, N. E. *Nature* **408**, 695 (2000).

[26] Tracht, U., Wilhelm, M., Heuer, A., Feng, H., Schmidt-Rohr, K., and Spiess, H. W. *Phys. Rev. Lett.* **81**, 2727–2730 Sep (1998).

[27] Ediger, M. D. *Annual review of physical chemistry* **51**, 99–128 (2000).

[28] Flier, B. M., Baier, M., Huber, J., Müllen, K., Mecking, S., Zumbusch, A., and Wöll, D. *Physical Chemistry Chemical Physics* **13**, 1770 (2011).

[29] Hutchinson, J. M. *The Physics of Glassy Polymers*. Chapman and Hall, London, UK, (1997).

[30] Lee, H., Paeng, K., Swallen, S., and Ediger, M. *Science* **323**, 231–234 (2009).

[31] Weitz, D. A. *Science* **323**(5911), 214–215 (2008).

[32] Meijer, H. E. and Govaert, L. E. *Progress in Polymer Science* **30**(8-9), 915 – 938 (2005).

[33] Roth, C. B. *Journal of Polymer Science Part B: Polymer Physics* **48**(24), 2558–2560 (2010).

[34] Reiter, G. *The European Physical Journal E: Soft Matter and Biological Physics* **8**, 251–255 (2002).

[35] McKenna, G. *J. Phys.Condens. Matter* **15**, 737 (2003).

[36] Lee, H., Paeng, K., Swallen, S., and Ediger, M. *The Journal of Chemical Physics* **128**, 134902 (2008).

[37] Reiter, G. *Europhys. Lett* **23**, 579 (1993).

[38] Orts, W. J., van Zanten, J. H., Wu, W.-l., and Satija, S. K. *Phys. Rev. Lett.* **71**, 867–870 Aug (1993).

[39] Reiter, G. *Phys. Rev. Lett.* **87**, 186101 Oct (2001).

[40] Mukherjee, M., Bhattacharya, M., Sanyal, M. K., Geue, T., Grenzer, J., and Pietsch, U. *Phys. Rev. E* **66**, 061801 Dec (2002).

[41] Miyazaki, T., Nishida, K., and Kanaya, T. *Phys. Rev. E* **69**, 022801 Feb (2004).

[42] Reiter, G., Hamieh, M., Damman, P., Sclavons, S., Gabriele, S., Vilmin, T., and Raphael, E. *Nature Materials* **4**, 754–758 (2005).

[43] Priestley, R. D. *Soft Matter* **5**, 919–926 (2009).

[44] Kawana, S. and Jones, R. A. L. *Eur. Phys. J. E* **10**, 223–230 (2003).

[45] Raegen, A., Chowdhury, M., Calers, C., Schmatulla, A., Steiner, U., and Reiter, G. *Phys. Rev. Lett.* **105**, 227801 Nov (2010).

[46] Fakhraai, Z. and Forrest, J. *Science* **319**, 600–604 (2008).

[47] Siretanu, I., Chapel, J. P., and Drummond, C. *Macromolecules* **45**(2), 1001–1005 (2012).

[48] Akabori, K.-i., Tanaka, K., Kajiyama, T., and Takahara, A. *Macromolecules* **36**(13), 4937–4943 (2003).

[49] Paeng, K., Swallen, S. F., and Ediger, M. D. *Journal of the American Chemical Society* **133**(22), 8444–8447 (2011).

[50] Forrest, J. A., Dalnoki-Veress, K., Stevens, J. R., and Dutcher, J. R. *Phys. Rev. Lett.* **77**, 2002–2005 Sep (1996).

[51] Forrest, J. A., Dalnoki-Veress, K., and Dutcher, J. R. *Phys. Rev. E* **56**, 5705–5716 Nov (1997).

[52] Forrest, J. A. and Dalnoki-Veress, K. *Advances in Colloid and Interface Science* **94**(1-3), 167 – 195 (2001).

[53] Si, L., Massa, M. V., Dalnoki-Veress, K., Brown, H. R., and Jones, R. A. L. *Phys. Rev. Lett.* **94**, 127801 Apr (2005).

[54] Brown, H. R. and Russell, T. P. *Macromolecules* **29**(2), 798–800 (1996).

[55] Rathfon, J. M., Cohn, R. W., Crosby, A. J., and Tew, G. N. *Macromolecules* **44**(1), 134–139 (2011).

[56] Bodiguel, H. and Fretigny, C. *The European Physical Journal E: Soft Matter and Biological Physics* **19**, 185–193 (2006).

[57] Reiter, G., Al Akhrass, S., Hamieh, M., Damman, P., Gabriele, S., Vilmin, T., and Raphael, E. *The European Physical Journal - Special Topics* **166**, 165–172 (2009).

[58] Dalnoki-Veress, K., Nickel, B., Roth, C., and Dutcher, J. *Phys. Rev. E* **59**, 2153–2156 Feb (1999).

[59] Roth, C. B. and Dutcher, J. R. *Soft materials: structure and dynamics.* New York, Dekker, (2005).

[60] Tsui, O. K. *Polymer Thin Films.* World Scientific, (2008).

[61] Alcoutlabi, M. and McKenna, G. *J. Phys.: Condens. Matter* **17**, R461 (2005).

[62] Reiter, G. and Napolitano, S. *Journal of Polymer Science Part B: Polymer Physics* **48**(24), 2544–2547 (2010).

[63] Forrest, J. A. and Mattsson, J. *Phys. Rev. E* **61**, R53–R56 Jan (2000).

[64] van Zanten, J. H., Wallace, W. E., and Wu, W.-l. *Phys. Rev. E* **53**, R2053–R2056 Mar (1996).

[65] Peter, S., Meyer, H., and Baschnagel, J. *Journal of Polymer Science Part B: Polymer Physics* **44**(20), 2951–2967 (2006).

[66] Paeng, K., Richert, R., and Ediger, M. D. *Soft matter* **8**(17), 819 (2012).

[67] de Gennes, P. *The European Physical Journal E: Soft Matter and Biological Physics* **2**, 201–205 (2000).

[68] Ngai, K. *The European Physical Journal E: Soft Matter and Biological Physics* **8**, 225–235 (2002).

[69] Varnik, F., Baschnagel, J., and Binder, K. *Phys. Rev. E* **65**, 021507 Jan (2002).

[70] Herminghaus, S., Jacobs, K., and Seemann, R. *The European Physical Journal E: Soft Matter and Biological Physics* **5**, 531–538 (2001).

[71] Efremov, M. Y., Olson, E. A., Zhang, M., Zhang, Z., and Allen, L. H. *Phys. Rev. Lett.* **91**, 085703 Aug (2003).

[72] Tress, M., Erber, M., Mapesa, E. U., Huth, H., Müller, J., Serghei, A., Schick, C., Eichhorn, K.-J., Voit, B., and Kremer, F. *Macromolecules* **43**(23), 9937–9944 (2010).

[73] Napolitano, S. and Wubbenhorst, M. *Nature Communications* **2**, 260 March (2011).

[74] Jiang, Z., Kim, H., Jiao, X., Lee, H., Lee, Y.-J., Byun, Y., Song, S., Eom, D., Li, C., Rafailovich, M. H., Lurio, L. B., and Sinha, S. K. *Phys. Rev. Lett.* **98**, 227801 May (2007).

[75] Tsui, O. K. C., Wang, Y. J., Lee, F. K., Lam, C.-H., and Yang, Z. *Macromolecules* **41**(4), 1465–1468 (2008).

[76] Reiter, G. and de Gennes, P. *The European Physical Journal E: Soft Matter and Biological Physics* **6**, 25–28 (2001).

[77] Rowland, H., King, W., Pethica, J., and Cross, G. *Science* **322**, 720–724 (2008).

[78] Yang, M. H., Hou, S. Y., Chang, Y. L., and Yang, A. C.-M. *Phys. Rev. Lett.* **96**, 066105 Feb (2006).

[79] Chung, J. Y., Chastek, T. Q., Fasolka, M. J., Ro, H. W., and Stafford, C. M. *ACS Nano* **3**(4), 844–852 (2009).

[80] Thomas, K. and Steiner, U. *Soft Matter* **7**, 7839 (2011).

[81] Damman, P., Gabriele, S., Coppée, S., Desprez, S., Villers, D., Vilmin, T., Raphaël, E., Hamieh, M., Akhrass, S. A., and Reiter, G. *Phys. Rev. Lett.* **99**, 036101 Jul (2007).

[82] Kavassalis, T. A. and Noolandi, J. *Macromolecules* **21**(9), 2869–2879 (1988).

[83] Fetters, L. J., Lohse, D. J., Richter, D., Witten, T. A., and Zirkel, A. *Macromolecules* **27**(17), 4639–4647 (1994).

[84] Tretinnikov, O. N. and Zbankov, R. G. *Macromolecules* **37**(10), 3543–3545 (2004).

[85] Mukhopadhyay, M., Jiao, X., Lurio, L., Jiang, Z., Stark, J., Sprung, M., Narayanan, S., Sandy, A., and Sinha, S. *Phys.Rev.Lett* **101**, 115501 (2008).

[86] Itagaki, H., Nishimura, Y., Sagisaka, E., and Grohens, Y. *Langmuir* **22**(2), 742–748 (2006).

[87] O'Connell, P. A. and McKenna, G. B. *Science* **307**(5716), 1760–1763 (2005).

[88] Silberberg, A. *Journal of Colloid and Interface Science* **90**(1), 86 – 91 (1982).

[89] Brulet, A., Boue, F., Menelle, A., and Cotton, J. P. *Macromolecules* **33**(3), 997–1001 (2000).

[90] Kraus, J., Müller-Buschbaum, P., Kuhlmann, T., Schubert, D., and Stamm, M. *Europhys. Lett.* **49(2)**, 210–216 (2000).

[91] Barbero, D. R. and Steiner, U. *Phys. Rev. Lett.* **102**, 248303 Jun (2009).

[92] McGraw, J., Jago, N., and Dalnoki-Veress, K. *Soft Matter* **7**, 7832 (2011).

[93] De Gennes, P. G. *Rev. Mod. Phys.* **57**, 827 (1985).

[94] Blake, T. *Journal of Colloid and Interface Science* **299**(1), 1 – 13 (2006).

[95] De Gennes, P.-G., Brochard-Wyart, F., and Quere, D. *Capillarity and wetting phenomena: drops, bubbles, pearls, waves*. Springer (Heidelberg), (2003).

[96] Reiter, G. In *Handbook of adhesion technology*. Springer-Verlag, Berlin/ Heidelberg (2011).

[97] Israelachvili, J. N. *Intermolecular and Surface Forces, Second Edition: With Applications to Colloidal and Biological Systems (Colloid Science)*. Academic Press, (1992).

[98] Müller-Buschbaum, P. *The European Physical Journal E: Soft Matter and Biological Physics* **12**, 443–448 (2003).

[99] Hamieh, M., Al Akhrass, S., Hamieh, T., Damman, P., Gabriele, S., Vilmin, T., Raphael, E., and Reiter, G. *The Journal of Adhesion* **83**(4), 367–381 (2007).

[100] Brochard-Wyart, F. and de Gennes, P. *Advances in Colloid and Interface Science* **39**(0), 1 – 11 (1992).

[101] Bäumchen, O. and Jacobs, K. *J.Phys. Condens. Matter* **22**, 033102 (2010).

[102] Vilmin, T. and Raphael, E. *The European Physical Journal E: Soft Matter*

and Biological Physics **21**, 161–174 (2006).

[103] Bonn, D., Egges, J., Indekeu, J., Meunier, J., and Rolley, E. *Rev. Mod. Phys* **81**, 739 (2009).

[104] Reiter, G. In *Glass Transition, Dynamics and Heterogeneity of Polymer Thin Films,* Kanaya, T., editor, Advances in Polymer Science. Springer (2012). (in press).

[105] Ziebert, F. and Raphael, E. *Phys. Rev. E* **79**, 031605 Mar (2009).

[106] Brochard-Wyart, F., Debregeas, G., Fondecave, R., and Martin, P. *Macromolecules* **30**(4), 1211–1213 (1997).

[107] Redon, C., Brochard-Wyart, F., and Rondelez, F. *Phys. Rev. Lett.* **66**, 715–718 Feb (1991).

[108] Debregeas, G., de Gennes, P.-G., and Brochard-Wyart, F. *Science* **279**(5357), 1704–1707 (1998).

[109] Damman, P., Baudelet, N., and Reiter, G. *Phys. Rev. Lett.* **91**, 216101 Nov (2003).

[110] Gabriele, S., Sclavons, S., Reiter, G., and Damman, P. *Phys. Rev. Lett.* **96**, 156105 Apr (2006).

[111] Al Akhrass, S. A. *Démouillage des films minces viscoélastique sur substrats glissants et déformables.* PhD thesis, Universite de Haute Alsace, (2007).

[112] Sauer, B. B. and Walsh, D. J. *Macromolecules* **27**(2), 432–440 (1994).

[113] Saulnier, F., Raphaël, E., and de Gennes, P.-G. *Phys. Rev. Lett.* **88**, 196101 Apr (2002).

[114] Shenoy, V. and Sharma, A. *Phys. Rev. Lett.* **88**, 236101 May (2002).

[115] Herminghaus, S., Seemann, R., and Jacobs, K. *Phys. Rev. Lett.* **89**, 056101 Jul (2002).

[116] Vilmin, T., Raphaël, E., Damman, P., Sclavons, S., Gabriele, S., M., H., and Reiter, G. *Europhys. Lett* **73(6)**, 906–912 (2006).

[117] Strobl, G. *The Physics Of Polymer.* Springer, Berlin, (1997).

[118] Kramer, E. and Berger, L. In *Crazing in Polymers Vol. 2,* Kausch, H., editor, volume 91 of *Advances in Polymer Science*, 1–68. Springer Berlin / Heidelberg (1990).

[119] Lee, J.-Y. *Deformation and failures in nanostructured polymer thin films.* PhD thesis, University of Massachusetts, (2007).

[120] Kramer, E. In *Crazing in Polymers,* Kausch, H., editor, volume 52-53 of *Advances in Polymer Science*, 1–56. Springer Berlin / Heidelberg (1983).

[121] Yang, A. C. M., Kunz, M. S., and Logan, J. A. *Macromolecules* **26**(7), 1767–1773 (1993).

[122] McLeish, T., Plummer, C., and Donald, A. *Polymer* **30**(9), 1651 – 1655 (1989).

[123] Donald, A. *The physics of glassy polymers.* Chapman and Hall, London, UK, (1997).

[124] Yang, A. C. M., Kramer, E. J., Kuo, C. C., and Phoenix, S. L. *Macromolecules* **19**(7), 2010–2019 (1986).

[125] Brown, H. R. *Macromolecules* **24**(10), 2752–2756 (1991).

[126] Rottler, J., Barsky, S., and Robbins, M. O. *Phys. Rev. Lett.* **89**, 148304 Sep (2002).

[127] Rottler, J. and Robbins, M. O. *Phys. Rev. E* **68**, 011801 Jul (2003).

[128] Sha, Y., Hui, C. Y., Ruina, A., and Kramer, E. J. *Macromolecules* **28**(7), 2450–2459 (1995).

[129] Brandrup, J., Immergut, E., and Grulke, E. *Polymer handbook.* John Wiley & Sons, Inc., (2003).

[130] Neergaard Waltenburg, H. and Yates, J. T. *Chemical Reviews* **95**(5), 1589–1673 (1995).

[131] Frantz, P. and Granick, S. *Langmuir* **8**(4), 1176–1182 (1992).

[132] Fink, C. K., Nakamura, K., Ichimura, S., and Jenkins, S. J. *Journal of Physics: Condensed Matter* **21**(18), 183001 (2009).

[133] Iler, R. K. *The Chemistry of Silica.* John Wiley and Sons: New York, (1979).

[134] Tong, Q.-Y. and Gösele, U. *Semiconductor Wafer Bonding Science and Technology.* John Wiley & Sons, (1998). chapter 5.

[135] Patel, A., Cosgrove, T., Semlyen, J., Webster, J., and Scheutjens, J. *Colloids and Surfaces A: Physicochemical and Engineering Aspects* **87**(1), 15 –

24 (1994).

[136] Tsige, M., Soddemann, T., Rempe, S. B., Grest, G. S., Kress, J. D., Robbins, M. O., Sides, S. W., Stevens, M. J., and Webb III, E. *Journal of Chemical Physics* **118**, 5132 (2003).

[137] Gabriele, S. *Rupture de Films Minces de Polymére Dynamique, Fracture, Digitation.* PhD thesis, Laboratoire de Physico-Chimie des Polyméres, Département de Chimie, Université de Mons-Hainaut, (2006).

[138] Guiselin, O. *Europhysics Letters* **17**(3), 225 (1992).

[139] Léger, L., Raphaël, E., and Hervet, H. In *Polymers in Confined Environments,* Granick, S., Binder, K., de Gennes, P.-G., Giannelis, E., Grest, G., Hervet, H., Krishnamoorti, R., Léger, L., Manias, E., Raphaël, E., and Wang, S.-Q., editors, volume 138 of *Advances in Polymer Science*, 185–225. Springer Berlin / Heidelberg (1999).

[140] Bornside, D., Macosko, C., and Scriven, L. *Journal of Imaging Technology* **13**, 122–128 (1987).

[141] Croll, S. G. *Journal of Applied Polymer Science* **23**(3), 847–858 (1979).

[142] Chakraborty, M., Chowdhury, D., and Chattopadhyay, A. *Journal of Chemical Education* **80**(7), 806 (2003).

[143] Sengbusch, P. V. Internet (Botany online, University of Hamburg), July (2003).

[144] Coulon, G., Ausserre, D., and Russell, T. *J. Phys. France* **51**(8), 777–786 (1990).

[145] Botiz, I., Schlaad, H., and Reiter, G. In *Self Organized Nanostructures of Amphiphilic Block Copolymers II,* Müller, A. H. and Borisov, O., editors, volume 242 of *Advances in Polymer Science*, 117–149. Springer Berlin / Heidelberg (2011).

[146] Schäffer, E. *Instabilities in Thin Polymer Films: Structure Formation and Pattern Transfer.* PhD thesis, Fachbereich für Physik, Universität Konstanz, (2001).

[147] Binnig, G., Quate, C. F., and Gerber, C. *Phys. Rev. Lett.* **56**(9), 930–933 Mar (1986).

[148] Magonov, S. N.; Reneker, D. H. *Annu. Rev. Mater. Sci.* **27**, 175 (1997).

[149] Sommer, J. U. and Reiter, G. In *Ordered Polymeric Nanostructures at Surfaces*. Springer Berlin / Heidelberg (2006).

[150] Basu, N., Osichow, A., Mecking, S., and Reiter, G. *The European Physical Journal E: Soft Matter and Biological Physics* **35**, 1–12 (2012).

[151] Goldbeck-Wood, G., Bliznyuk, V. N., Burlakov, V., Assender, H. E., Briggs, G. A. D., Tsukahara, Y., Anderson, K. L., and Windle, A. H. *Macromolecules* **35**(13), 5283–5289 (2002).

[152] Tweedie, C. A., Constantinides, G., Lehman, K. E., Brill, D. J., Blackman, G. S., and Van Vliet, K. J. *Advanced Materials* **19**(18), 2540 (2007).

[153] Magonov, S., Elings, V., and Whangbo, M.-H. *Surface Science* **375**(2-3), L385 – L391 (1997).

[154] Rothen, A. *Review of Scientific Instruments* **16**(2), 26 –30 feb (1945).

[155] Ellison, C. and Torkelson, J. *Nature Materials* **2**, 695–700 (2003).

[156] Priestley, R., Ellison, C., Broadbelt, L., and Torkelson, J. *Science* **309**, 456–459 (2005).

[157] Kim, S. and Torkelson, J. M. *Macromolecules* **44**(11), 4546–4553 (2011).

[158] Pye, J. E., Rohald, K. A., Baker, E. A., and Roth, C. B. *Macromolecules* **43**(19), 8296–8303 (2010).

[159] Frieberg, B., Glynos, E., and Green, P. F. *Phys. Rev. Lett.* **108**, 268304 Jun (2012).

[160] Pfromm, P. and Koros, W. *Polymer* **36**(12), 2379 – 2387 (1995).

[161] Huang, Y. and Paul, D. *Polymer* **45**(25), 8377 – 8393 (2004).

[162] Rowe, B. W., Freeman, B. D., and Paul, D. R. *Polymer* **50**(23), 5565 – 5575 (2009).

[163] Teichroeb, J. H. and Forrest, J. A. *Phys. Rev. Lett.* **91**, 016104 Jul (2003).

[164] Yang, Z., Fujii, Y., Lee, F. K., Lam, C.-H., and Tsui, O. K. C. *Science* **328**(5986), 1676–1679 (2010).

[165] Lupascu, V., Picken, S. J., and Wübbenhorst, M. *Journal of Non-Crystalline Solids* **352**(52-54), 5594 – 5600 (2006).

[166] Dhinojwala, A., Wong, G., and Torkelson, J. *J. Chem. Phys.* **100(8)**, 6046–6054 (1994).

[167] Fukao, K. and Koizumi, H. *Phys. Rev. E* **77**, 021503 Feb (2008).

[168] Rotella, C., Napolitano, S., De Cremer, L., Koeckelberghs, G., and Wübbenhorst, M. *Macromolecules* **43**(20), 8686–8691 (2010).

[169] Yano, O. and Wada, Y. *Journal of Polymer Science Part A-2: Polymer Physics* **9**(4), 669–686 (1971).

[170] Lupascu, V., Picken, S. J., and Wübbenhorst, M. *Macromolecules* **39**(15), 5152–5158 (2006).

[171] de Gennes, P. *The European Physical Journal E: Soft Matter and Biological Physics* **7**, 31–34 (2002).

[172] Grohens, Y., Hamon, L., Spevacek, J., and Holl, Y. *Macromolecular Symposia* **203**(1), 155–164 (2003).

[173] Thomas, K. R., Chenneviere, A., Reiter, G., and Steiner, U. *Phys. Rev. E* **83**, 021804 Feb (2011).

[174] Tsui, O. K. C. and Zhang, H. F. *Macromolecules* **34**(26), 9139–9142 (2001).

[175] Raegen, A., Chowdhury, M., Schmatulla, A., and Reiter, G. In *Makromolekulares Kolloquium Freiburg Conference Proceedings published in Macromol. Rapid Comm.*, volume 31, F62, (2010).

[176] Hamieh, M. *Stabilité et Démouillage des Couches Minces de Polystyrène Proche de la Transition Vitreuse*. PhD thesis, Institut de Chimie des Surfaces et Interfaces (ICSI), (2006).

[177] Sun, S.-T., Nishio, I., Swislow, G., and Tanaka, T. *Journal of Chemical Physics* **73**, 5971 (1980).

[178] Schneider, H. A. *Die Makromolekulare Chemie* **189**(8), 1941–1955 (1988).

[179] Richardson, H., Carelli, C., Keddie, J., and Sferrazza, M. *The European Physical Journal E: Soft Matter and Biological Physics* **12**, 437–441 (2003).

[180] Reiter, G. *Phys. Rev. Lett.* **68**, 75–78 Jan (1992).

[181] Coppée, S., Gabriele, S., Jonas, A., Jestin, J., and Damman, P. *Soft Matter* **7**, 9951 (2011).

[182] Ziebert, F. and Raphael, E. *Europhys. Lett* **86**, 46001 (2009).

[183] Raphael, E. and De Gennes, P. G. *The Journal of Physical Chemistry* **96**(10), 4002–4007 (1992).

[184] Reiter, G., Schultz., J., Auroy, P., and Auvray, L. *Europhys. Lett* **33 (1)**, 29 (1996).

[185] Ajdari, A., Brochard-Wyart, F., Gay, C., de Gennes, P., and Viovy, J. *J. Phys. II France* **5**(4), 491–495 (1995).

[186] Chung, J. Y., Lee, J.-H., Beers, K. L., and Stafford, C. M. *Nano Letters* **11**(8), 3361–3365 (2011).

[187] Mulheran, P. A. *Philosophical Magazine Letters* **68**(2), 63–68 (1993).

[188] Liang, J., Huang, R., Prevost, J., and Suo, Z. *International Journal of Solids and Structures* **40**(10), 2343 – 2354 (2003).

[189] Leung, K.-t. and Neda, Z. *Phys. Rev. Lett.* **85**, 662–665 Jul (2000).

[190] Leung, K.-t. and Neda, Z. *Phys. Rev. E* **82**, 046118 Oct (2010).

[191] Singh, K. B. and Tirumkudulu, M. S. *Phys. Rev. Lett.* **98**, 218302 May (2007).

[192] Goehring, L. *Phys. Rev. E* **80**, 036116 Sep (2009).

[193] Hillerborg, A., Modéer, M., and Petersson, P.-E. *Cement and Concrete Research* **6**(6), 773 – 781 (1976).

[194] Cook, R. F. and Suo, Z. *MRS Bulletin* **27**, 45–51 (2002).

[195] Kearney, A. *Fracture and fatigue of nanoporous ultrathin polymer films.* PhD thesis, Stanford University, (2008).

[196] Frank, S., Handge, U. A., Olliges, S., and Spolenak, R. *Acta Materialia* **57**(5), 1442 – 1453 (2009).

[197] Hornig, T., Sokolov, I. M., and Blumen, A. *Phys. Rev. E* **54**, 4293–4298 Oct (1996).

[198] Kramer, E. J. *Journal of Materials Science* **14**, 1381–1388 (1979).

[199] Donald, A. M., Chan, T., and Kramer, E. J. *Journal of Materials Science* **16**, 669–675 (1981).

[200] Crosby, A. J., Fasolka, M. J., and Beers, K. L. *Macromolecules* **37**(26), 9968–9974 (2004).

[201] Cheng, L. and Guo, T. *Interface Science* **11**, 277–290 (2003).

[202] Krupenkin, T. N. and Fredrickson, G. H. *Macromolecules* **32**(15), 5029–

5035 (1999).

[203] Zhang, Z. D., Chern, S. S., and Hsiao, C. C. *Journal of Applied Physics* **54**, 5568 – 5576 (1983).

[204] Argon, A. S. and Hannoosh, J. G. *Philosophical Magazine* **36**(5), 1195–1216 (1977).

[205] Kambour, R. P. *Polymer Communications* **24**, 292–296 (1983).

[206] Gusler, G. M. and McKenna, G. B. *Polymer Engineering & Science* **37**(9), 1442–1448 (1997).

[207] van Melick, H., Govaert, L., and Meijer, H. *Polymer* **44**(8), 2493 – 2502 (2003).

[208] Francis, L. F., Mccormick, A. V., Vaessen, D. M., and Payne, J. A. *Journal of Materials Science* **37**, 4717–4731 (2002).

[209] Tsige, M. and Grest, G. S. *Macromolecules* **37**(12), 4333–4335 (2004).

[210] Okuzono, T., Ozawa, K., and Doi, M. *Phys. Rev. Lett.* **97**(13), 136103 Sep (2006).

[211] Strawhecker, K. E., Kumar, S. K., Douglas, J. F., and Karim, A. *Macromolecules* **34**(14), 4669–4672 (2001).

[212] Coppée, S. *Structuration et relaxation de chaines dans les films minces de polymeres*. PhD thesis, Universite de Mons-Hainaut, (2007).

[213] McKenna, G. B. *J. Physique IV* **10**, 53–57 (2000).

[214] Head, D. A. *Phys. Rev. E* **74**, 021601 Aug (2006).

[215] Brown, H. R. and Yang, A. C. M. *Journal of Materials Science* **25**, 2866–2868 (1990).

List of Figures

List of Tables

Acknowledgments

This thesis is the end of my long journey in obtaining my doctoral degree. There are many people I met during this time who had extended their support either by words of encouragement or valuable advice. It is a pleasant aspect that I have now the opportunity to express my heartfelt gratitude to all of you.

First of all, I would like the thank you Prof. Günter Reiter for giving me the opportunity to join your group, for supervising this PhD thesis. I appreciate your ideas, support, and also the valuable guidance throughout my doctoral life. Being the first student of the newly moved group, my start-up was not so easy. Thanks for being on my side for all those hard times. I would like to thank you also for introducing me to the soft matter community by giving me the opportunity to participate in many national and international conferences, schools and visits.

I would like to thank all of my collaborators for the valuable inputs in my research. Thank you Prof. Ullrich Steiner (Cambridge, UK) for those nice discussions (during your frequent visits in Freiburg) and for your always quick responses while you are in Cambridge. Thank you Prof. Arnold C.-M. Yang (Hsinchu, Taiwan), it was always nice to get your comments before I was starting my work in the morning. That is somehow the long geographical distance between us worked in the positive sense. Thank you Prof. Ophelia Tsui (Boston, USA) for the most recent collaboration and discussion during your visit in Freiburg. Dr. Adam Raegen, many thanks to you, being a postdoc in our group you made my research life easier and more systematic, especially when I was in my early days here. Dr. Falko Ziebert, Thank you very much for all those discussions and helps to understand the theoretical and conceptual background in my work. Thanks also for being given so much effort to correct the first version of this thesis. Paul Freyberg, Chris Calers and Abhishek Modi, you guys assisted me a lot. I want to thank all of you, my junior collaborators, for being so collaborative and sometime made me feel, I am the boss!

Besides my supervisor I would like to thank the rest of my thesis committee: Prof. Dr. Alexander Blumen and Prof. Dr. Elizabeth von Hauff (as my

examiners) for their encouragement, insightful comments and the time they are going to spend for the evaluation.

I must thank Dr. Moustafa Hamieh and Dr. Samer Al Akhrass for some preliminary experimental studies which were the starting point for few portions of my present work.

I would like to acknowledge the funding source from Deutsche Forschungsgemeinschaft (DFG), especially through the Materials World Network (MWN) in collaboration with National Science Foundation (NSF).

I enjoyed discussions through insightful comments from several scientists (either during conferences or their visit to Freiburg). Especially, I would like to name Prof. Jörg Baschnagel (Strasbourg, France), Prof. Kari Dalnoki-Veress (Hamilton, Canada), Prof. Greg McKenna (Texas, USA), Prof. Michael Wübbenhorst (Leuven, Belgium), Prof. Mark Geoghegan (Sheffield, UK), Prof. Ullrich Handge (Bayreuth, Germany) and Prof. Jun Xu (Beijing, China). It was nice for me to be in touch to get scientifically enriched with those groups, working closely to my research topics, in India. I wish to thank Prof. Milan K. Sanyal (SINP, Kolkata), Prof. Ashutosh Sharma (IIT-Kanpur) and Dr. Rabibrata Mukherjee (IIT-Kharagpur) for encouraging all those visits to their lab.

It was always nice to share the office, lab and moreover the life after science with all the present and past members of the group during my entire stays here in Germany. I am lucky to be in such an International group and getting the chances to meet you all from around the globe. Prof. Gert Strobl, thanks for all of those discussions. It feels me great to be in one of the traditional German polymer place. Thanks Prof. Achim Kittel, Dr. Werner Stille and Dr. Ioan Botiz, I learned from all of you, about your way to look into the science and life. Thank you Frau Heck, my life in Germany could not start so smoothly without your active help in all those bureaucratic matters in Freiburg. My best smile to all members of the experimental polymer physics group at the University of Freiburg.

I would like specially to thank Prof. Milan K. Sanyal (SINP, Kolkata), Dr. Nikhil Guchhait (Univ. of Calcutta) and Prof. T. P. Radhakrishnan (Univ. of Hyderabad), among my teachers/supervisors during my M.Sc. in India to encourage me before I started my PhD to travel abroad and to delete frontiers in the world of science.

Thanks to my mom and my wife who have always been there for me. Thank you for your constant support and encouragement in everything.